Background Determination in the Salt Phase of the Sudbury Neutrino Observatory Experiment

Charlotte Sims
Worcester College, Oxford

Thesis submitted in partial fulfilment of the requirements
for the degree of Doctor of Philosophy
at the University of Oxford
Hilary Term 2005

Background Determination in the Salt Phase of the Sudbury Neutrino Observatory Experiment

Charlotte Sims
Worcester College, Oxford

Thesis submitted in partial fulfilment of the requirements
for the degree of Doctor of Philosophy
at the University of Oxford
Hilary Term 2005

Abstract

The Sudbury Neutrino Observatory experiment is a heavy water Čerenkov imaging detector that has the unique ability of measuring both the total active flux, and the electron-type only flux, of solar neutrinos from the ^{8}B spectrum. The total active flux is measured by detecting neutrons that result from the interaction of neutrinos with a deuteron, splitting it into a neutron and a proton. The electron-type neutrinos produce detectable electrons through W exchange with quarks within the deuterons. Any measured deficit in the electron-type neutrino flux with respect to the total flux strongly supports the theory of flavour oscillations in the neutrino sector, as in the quark sector.

This thesis identifies the low energy radioactive backgrounds of ^{238}U, ^{232}Th and ^{24}Na that also produce neutrons by photodisintegrating the deuteron, indistinguishable from those produced by neutrinos. It assesses the latest theoretical predictions for the cross sections for such reactions. Each radioactive element has a different cross section for this reaction and so the levels must be determined separately.

The daughters of the ^{238}U and ^{232}Th chains, ^{214}Bi and ^{208}Tl respectively, produce statistically separable patterns of Čerenkov light within the D_2O. Since that of ^{24}Na closely resembles that of ^{208}Tl it was determined by independent modelling of its production. A separate method removed time periods when the ^{24}Na was most likely to be present within the data set. Agreement between the two analyses confirmed that the modelling was reasonable. The extracted number of events in the salt data set contributing to the total active flux was corrected to allow for the $102.2^{+29.6}_{-33.1}$ photodisintegration neutrons from these sources of radioactivity.

Better understanding of these backgrounds and the application of an energy dependent fiducial volume allowed for combined signal and background extraction, down to a kinetic energy of 4 MeV, yielding fluxes of:

$$\phi(\nu_{\text{total}}) = 4.85\ ^{+0.19}_{-0.19}\ (\text{stat})\ ^{+0.24}_{-0.22}\ (\text{syst})\ \times 10^{-6}\text{cm}^{-2}\text{s}^{-1}$$
$$\phi(\nu_e) = 1.73\ ^{+0.05}_{-0.05}\ (\text{stat})\ ^{+0.07}_{-0.09}\ (\text{syst})\ \times 10^{-6}\text{cm}^{-2}\text{s}^{-1}\ .$$

This agrees with Standard Solar Model predictions for the total active ^{8}B solar neutrino flux and supports the hypothesis of neutrino flavour oscillations.

To my parents....

Acknowledgements

Nick Jelley is a fantastic supervisor. I feel very privileged to have been his student and have very much enjoyed working with him. I was also very lucky to share 652 (and 507) with Jessica and Jeanne, who were always happy to pass on the secrets of SNO. On a scale of one to ten, they're great friends.

The rest of the SNO group (Steve, Simon, Kai, James, Wan and more recently Helen and Gabriel) have been a pleasure to work with, and, when in Sudbury, to live with. Thanks for the lunch box!

I have enjoyed working as part of a close collaboration and forming professional and social relationships with my peers and my tribal elders. I would particularly like to thank Josh, Neil, Alan, Jacques and Kevin for their advice, encouragement and friendship. Thanks also to Ryan for taking me skating on thin ice and to Chris for teaching me everything a girl should know about electronics and Canada.

I would also like to thank Fred for encouraging me to follow this path and Tamsin for keeping me on it. All my friends, in particular Roger, Charles and Anna, have been very supportive over the last few years - although I'd like to think I've changed their view of a stereotypical physicist! Toby has been a wonderful distraction from physics, except for his inspired choice of a "Monte Carlo" party just after I submitted!

The two who deserve the most thanks are my parents. This would not have been possible without their love and support. Their continual interest in what I am doing is always greatly appreciated.

Our gaze is submarine, our eyes look upward
And see the light that fractures through unquiet water.
We see the light but see not whence it comes.
Oh, Light Invisible, we glorify Thee!

T. S. Eliot
Choruses from "The Rock"

Contents

List of Figures

List of Tables

Chapter 1

Neutrino Theory

The area of science that studies the fundamental properties of particles and their interactions started with the discovery of the electron by J. J. Thomson in 1897 and the splitting of the atom in 1911 by E. Rutherford. Particle physics has since become one of the most philosophically, theoretically, and, in the regime of experimental determination, technologically challenging areas of modern physics research.

Tremendous progress has been made over the last fifty years[1] by international collaborations of experimentalists and theorists who have attempted to find a unified description of particle physics. Our current understanding, called the Standard Model (SM), predicts

$+2/3$	u	c	t	quarks
$-1/3$	d	s	b	
-1	e	μ	τ	leptons
0	ν_e	ν_μ	ν_τ	

Table 1.1: The three generations of quarks and the three generations of leptons that form all matter and their associated electric charge.

all matter is either of hadronic (quarks) or leptonic form. The quarks and leptons are each grouped together in three generations, of which only the first generation is found in natural matter. All interactions occur through boson exchange.[2] Quarks never exist in isolation. They have fractional charge and group together as the structural basis for larger particles (mesons or hadrons) with integer charge. They are bound together according to

[1] CERN celebrates its golden jubilee in 2004

[2] gravity has not yet been successfully incorporated into the Standard Model but its effect on particle interactions is negligible in comparison to the strong and electroweak interactions.

their colour[3] by gluons which mediate the strong force. The quarks within the mesons or hadrons may then interact with leptons, or other quarks, by exchange of photons, Z^0 or $W^{\pm}$ bosons, which all mediate the electroweak force. This interaction, a combination of the electromagnetic and weak interactions, is a triumph of the SM and a step towards the goal to unify all four interaction types into one Grand Unified Theory.

The model has been extremely successful, for example in its prediction of particle interaction modes, but there still remain a number of unanswered and fundamentally important issues, so-called 'Beyond the Standard Model'. The experiment of this thesis was devised to investigate the anomaly referred to as the Solar Neutrino Problem; why there seems to be a deficit in the neutrino flux from the Sun when compared with solar model estimates. A possible solution could be physics beyond the SM.

1.1 Neutrinos within the Standard Model

The neutrino, ν, which means 'little light one', was first hypothesised in 1930 by W. Pauli [1] to explain the continuous energy spectra seen in the beta (β) decay of *e.g.* ^{210}Bi, and yet still allow the process to conserve energy, spin and angular momentum:

$$^{210}\mathrm{Bi} \rightarrow \ ^{210}\mathrm{Po} + \mathrm{e}^- + \bar{\nu}_\mathrm{e} \ ; \tag{1.1}$$

$$\mathrm{n} \rightarrow \ \mathrm{p} + \mathrm{e}^- + \bar{\nu}_\mathrm{e} \ . \tag{1.2}$$

Further experimental observations of β decay in the 1950's showed that the electron was preferentially emitted in a particular direction with respect to the nuclear spin of the decaying nucleus, *e.g.* a ^{60}Co atom [2]. This indicated violation of parity, a symmetry that transforms $x \rightarrow -x$, which had been assumed to be conserved in all reactions. Since the helicity of a particle is defined as the projection of spin in the direction of momentum:

$$\mathcal{H} = \frac{\vec{\sigma} \cdot \vec{p}}{\mid \vec{p} \mid} \ , \tag{1.3}$$

and both these quantities must be conserved, experiments indicated that the electron is of definite helicity in β decay. The same must be true for the emitted anti-neutrino, experimentally shown to have positive helicity. Neutrinos (and electrons) have opposite helicity to their anti-particles.

[3] they form colour singlets such as rgb or $r\bar{r}$

R. Feynman and M. Gell-Mann constructed a general (for both quarks and leptons) theory of the weak interaction [3], which explicitly included the phenomenon of maximal parity violation, by representing particles as two-component Weyl spinors. On translation to a system requiring 4-component Dirac particles, they showed that the interacting currents of a neutrino and positron were coupled by a $\gamma_\mu(1-\gamma_5)$ operator. The choice of sign was fixed according to the experimentally observed helicity of the neutrino in the Goldhaber experiment [4]. This is a reduced combination of a vector and an axial vector component, as shown in Table 1.2, and hence the theory is referred to as the V-A theory of the weak interaction.

Operator	Transformation Properties	γ Matrix Representation
S	scalar	1
V	vector	γ_μ
T	tensor	$\gamma_\mu\gamma_\nu$
A	axial-vector	$i\gamma_\mu\gamma_5$
P	pseudo-vector	γ_5

Table 1.2: The transformation properties of possible operators, and their representation in γ matrix notation.

Since an axial vector is one which does not reverse its direction under the parity operator, such as spin, and a polar vector is one which does, such as momentum, parity violation is necessarily implied by V-A couplings.

The neutrino is colourless and electrically neutral, and so only interacts weakly. Chirality projects out the *handedness* of a state so that it can not be superimposed onto its mirror image. The left-handed $\nu_{\rm L}$ can be obtained by a projection operator acting on a Dirac spinor:

$$\nu_{\rm L} = \Psi_{\rm L} = P_{\rm L}\Psi = \tfrac{1}{2}(1-\gamma_5)\Psi \ . \tag{1.4}$$

The right hand chiral operator is similarly obtained but involves a $+\gamma_5$. Since ${\gamma_5}^2 = 1$ and there is the anti-commutation relationship $\{\gamma_\mu, \gamma_5\} = 0$, $P_{\rm R}\Psi_{\rm L} = P_{\rm L}\Psi_{\rm R} = 0$ and so there are *no* right chiral terms that can exist for a neutrino. The neutrino thus exists in a state of definite helicity and chirality. In order for parity to be maximally violated in the weak interaction the W boson may only couple to left-handed particles or right-handed

anti-particles. This is forced within the SM by only allowing left-handed doublets and right-handed singlets, so that there are no right-handed neutrinos.

This has implications for the mass state of the neutrino. The Dirac equation requires a right- and left-handed component of a particle to describe the mass term.[4] Thus the absence of a right-handed neutrino within the SM implies that the neutrino is massless. Perhaps a more intuitive explanation is to reason that a particle which only exists in a state of defined helicity can not be Lorentz transformed into a state of opposite helicity. Only massless objects which are travelling at the speed of light can not undergo a Lorentz boost. So the neutrino must be massless (point-like) within the V-A framework.

For symmetry reasons the SM does not allow the possibility of a massless right-handed neutrino, which would allow right-handed particles to exist in doublets in agreement with the left-handed particles. Beyond the SM, of course, it is possible that right-handed neutrinos could exist, but just not interact weakly: so-called sterile neutrinos.

1.2 The Solar Neutrino Problem

W. Pauli and E. Fermi had predicted that the electrically neutral neutrino would have an extremely small cross section for interaction, so small in fact that making a source intense enough to allow detection seemed an insurmountable problem. However, C. Cowan and F. Reines noted in the 1950's [5] that one benefit of nuclear power is the enormous flux of anti-neutrinos produced as a by-product of fission in the reactors. They used a tank of $CdCl_2$ in $\sim 4000\,\mathrm{l}$ of liquid scintillator deployed near the Savannah River reactor to detect γ rays from the annihilation of a positron in delayed coincidence with those from neutron capture on Cd, the signal expected from the anti-neutrino inverse β decay reaction:

$$\bar{\nu_e} + \mathrm{p} \rightarrow \ \mathrm{n} + \mathrm{e}^+ \ . \tag{1.5}$$

They were able to measure an energy averaged cross-section for the reaction [6] of $(11 \pm 2.6) \times 10^{-44}\,\mathrm{cm}^{-2}\,\mathrm{s}^{-1}$, in agreement with V-A theory [7].

Soon after, R. Davis Jr proposed the idea of probing the structure of the Sun, essentially a fusion reactor (albeit 150 million km from Earth), to verify the neutrino fluxes from nuclear reactions that form the Standard Solar Model (SSM) with experimentation [8]. His experiment, using a tank of 615 tonnes of C_2Cl_4 as target in the Homestake

[4] The Higgs mechanism, which generates masses, also couples to both chiral fields

mine, USA, first published data in 1968. The importance of this experiment, which was the first to identify solar neutrinos, was acknowledged by the award of the 2002 Nobel Prize in Physics [9] to R. Davis Jr and M. Koshiba, "for pioneering contributions to astrophysics, in particular for the detection of cosmic neutrinos". The award was also given to R. Giacconi for his discovery of cosmic X-ray sources.

A neutrino can interact with ^{37}Cl to give ^{37}Ar atoms through the inverse β decay reaction

$$^{37}\mathrm{Cl} + \nu_{\mathrm{e}} \rightarrow \ ^{37}\mathrm{Ar} + \mathrm{e}^{-} \ , \tag{1.6}$$

provided its energy exceeds the threshold of 814 keV. In fact, the reaction is well suited to detect electron-type solar neutrinos from the ^{8}B spectrum, as illustrated in Figure 1.4, which can have enough energy to populate the excited isobaric analogue state of ^{37}Ar, 1.4 MeV above the ground state [7]. Every two months or so the radioactive ^{37}Ar atoms were extracted so that their decay could be monitored. A background corrected tally of the number of ^{37}Ar decays thereby inferred the flux of ^{8}B solar neutrinos.

A data sample collected over twenty years provided unexpected results; that the flux was 34% the assumed value from SSM [10]. There was much scepticism in the community until other ν flux experiments also showed a deficit when compared with the SSM. Either there were problems with the SSM or previously accepted theories of neutrino physics were incomplete. On hearing their results, B. Pontecorvo, who was to have a profound impact on the probable solution to the problem, remarked [11],"It starts to be really interesting! It would be nice if all this would end with something unexpected from the point of view of particle physics."

1.3 The Standard Solar Model

Models to explain the stellar evolution of the Sun and predict various solar properties, including the ratios of the neutrino fluxes, have been refined over the last fifty years, in particular by John Bahcall, a pioneer in this field. The main assumption is to treat the Sun as a spherical body in a state of constant hydrostatic equilibrium, that is to say that the gravitational pressure is balanced by the internal pressure of the very hot plasma heated by the nuclear reactions.

During the time when the Sun is fusing hydrogen into helium it is classed as a main

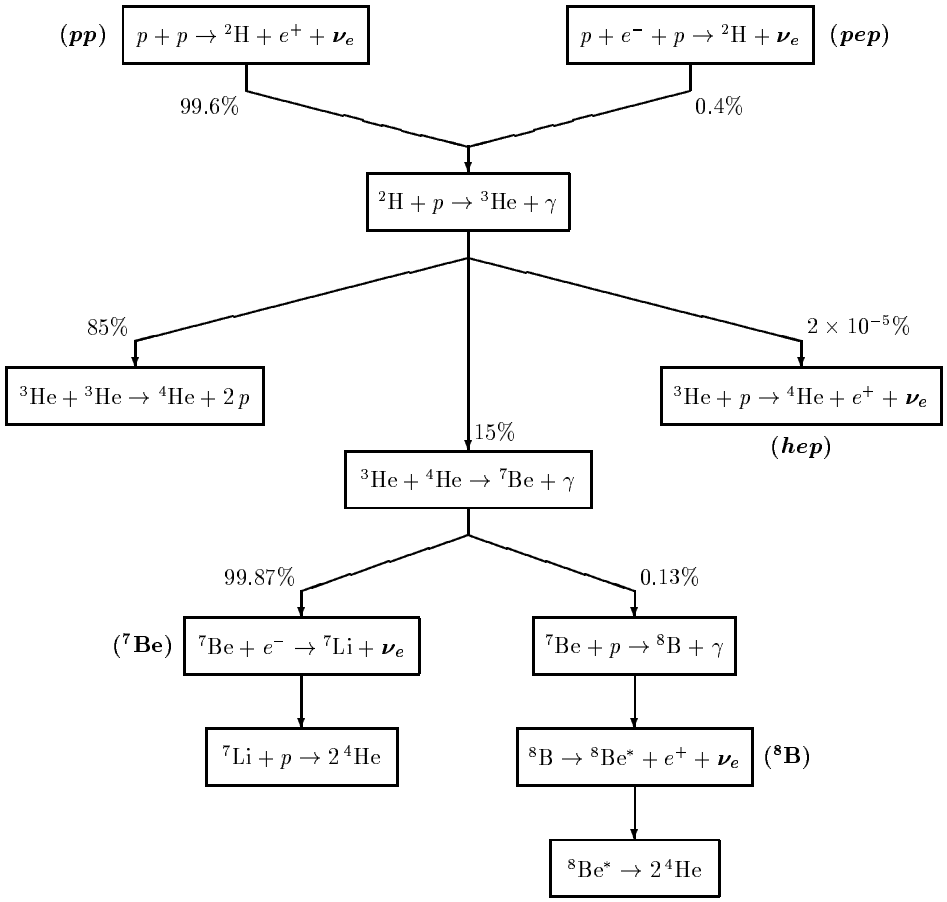

Figure 1.1: The various steps in the pp (p + p ..) chain that allow for the production of ^{8}B neutrinos, as well those from ^{7}Be, pep (p + e$^-$ $\rightarrow$ p ..) and hep (He + p ..) chains. Figure kindly provided by K. Zuber.

sequence star, and the elemental abundances in its photosphere can be used to determine the point in time at which it joined the main sequence to the present day, estimated to be 4.6 billion years. Deductions can then be made on the mass, radius, luminosity and spectrum, which will affect the rate of neutrino emission from the different chains relative to each other, shown schematically in Figure 1.1. An accurate estimate of the relative neutrino flux from each chain is vital for comparison to experiments, which are sensitive to a particular energy region, as shown in Figure 1.4, and so to neutrinos from specific reactions in the Sun. There are good reasons to believe that current SSMs are valid. In particular, one of the predicted quantities that is dependent on temperature and chemical abundance, is the sonar speed in the Sun, from which predictions for the frequency of the surface vibrational modes can be calculated. These are in agreement with helioseismological estimates to better than 0.1% [12], and can be used to yield information from the deeper modes within the solar interior on the electron density profile, which is important for MSW effect predictions (see section 1.4.2).

1.4 Massive Neutrinos

1.4.1 Oscillations

In the fermionic sector, quarks are not pure eigenstates of the weak interaction and there is mixing between the flavours. The probability of obtaining a certain flavour at time t is given by a linear superposition of its mass eigenstates, parameterised by the CKM (Cabibbo Kobayashi Maskawa) [13] matrix. The quark is said to oscillate between states, causing appearance of one flavour and thus disappearance of the orginal, and back again. Since the Davis experiment was capable of measuring only one leptonic flavour, similar oscillations in the neutrino sector could explain the deficit in solar neutrino flux.

Such mixing in the neutrino sector was first proposed by Pontecorvo [14], using a unitary matrix formulated by Maki, Sakata and Nakagawa (MSN matrix) describing transformations between the mass and flavour eigenstates, and can be expressed by

$$|\nu_\alpha > \; = \sum_n \mathrm{U}_{\alpha n} |\nu_n > \;\; , \tag{1.7}$$

or more explicitly:

$$\begin{pmatrix} \nu_{\mathrm{e}} \\ \nu_\mu \\ \nu_\tau \end{pmatrix} = \begin{pmatrix} \mathrm{U}_{e1} & \mathrm{U}_{\mathrm{e}2} & \mathrm{U}_{\mathrm{e}3} \\ \mathrm{U}_{\mu 1} & \mathrm{U}_{\mu 2} & \mathrm{U}_{\mu 3} \\ \mathrm{U}_{\tau 1} & \mathrm{U}_{\tau 2} & \mathrm{U}_{\tau 3} \end{pmatrix} \begin{pmatrix} \nu_1 \\ \nu_2 \\ \nu_3 \ . \end{pmatrix} \tag{1.8}$$

where $n(= 1, 2, 3)$ indicates the mass eigenstates and $\alpha(= e, \mu, \tau)$ indicates the flavour eigenstates. The time evolved wave function for a certain flavour of neutrino can be expressed in terms of the mass states as

$$\Psi(x,t) = \sum_n \mathrm{U}_{\alpha n} \nu_n e^{ip_\nu x} e^{-iE_\nu t} \ . \tag{1.9}$$

The energy of any relativistic particle can be expressed in natural units simply in terms of its mass and momentum, which, assuming that the mass is so small that $v \to c$, can be approximately expanded as

$$E_\nu = \sqrt{p_\nu^2 + m_n^2} \approx p_\nu + \frac{m_n^2}{2p_\nu} \ . \tag{1.10}$$

This approximation, Equation 1.10, allows the wavefunction at a particular time, essentially equivalent to distance under these conditions in natural units, to be expressed as:

$$\Psi(x, t \approx x) = \sum_{\alpha'} U^*_{\alpha' n} \left[\sum_n \exp\left(-ix \left(\frac{m_\alpha^2}{2p_\nu} \right) \right) U_{\alpha n} \right] \nu_{\alpha'} \ , \tag{1.11}$$

since the momentum exponent has cancelled with the first part of the energy expansion. The mass states of Equation 1.11 have been eliminated by expanding in terms of the flavour states and the transposed MNS matrix. So the wavefunction has in fact been transformed into a superposition of all the neutrino flavours, indicating that as it develops there is the possibility of detecting the neutrino in *different* flavour states.

If L is the distance between the release of a neutrino of definite flavour α, and its detection in a final flavour state β, then the amplitude for flavour conversion is

$$\mathrm{A}(\beta|\alpha) = \sum_n U^*_{\beta n} \exp\left(-iL \left(\frac{m_\alpha^2}{2E_\alpha} \right) \right) U_{\alpha n} \tag{1.12}$$

and the probability of detection is naturally $P = |\mathrm{A}(\beta|\alpha)|^2$, which will depend on the difference between the two mass states: $m_\alpha^2 - m_\beta^2$, or Δm^2. The final flavour thus depends on the depth of evolution (the distance L), the mass differences, the mixing matrix containing the angles between all the flavour states and the initial energy of the neutrino.

Experimental evidence [15] has shown that U_{e3} is small enough to be neglected to very good approximation, so the three neutrino flavour mixing may be approximated to

interference between just two neutrino flavour states: the ν_e and a normalised combination of ν_μ and ν_τ. The matrix is thus greatly simplified;

$$\mathrm{U} = \begin{pmatrix} c_{12}c_{13} & s_{12}c_{12} & s_{13}e^{-i\delta} \\ -s_{12}c_{23} - c_{12}s_{23}s_{13}e^{-i\delta} & c_{12}c_{23} - s_{12}s_{23}s_{13}e^{-i\delta} & s_{23}c_{13} \\ s_{12}s_{23} - c_{12}s_{13}e^{-i\delta} & -c_{12}s_{23} - s_{12}c_{23}s_{13}e^{-i\delta} & c_{23}c_{13} \end{pmatrix} \rightarrow \begin{pmatrix} \cos\theta & \sin\theta \\ -\sin\theta & \cos\theta \end{pmatrix} \tag{1.13}$$

in which c and s represent the sine or cosine of the angle between the two states given by the subscripts, and δ is the CP (charge parity) violating phase factor. In its more commonly used form, exact for two neutrino flavours analysis, only the angle between the two mass states 1 and 2 is relevant, and so can be globally replaced by a single mixing angle, θ. Substituting this into Eqn 1.12 and using some trigonometric relations for simplification, the probability for neutrino oscillation to a different flavour is

$$P(\beta|\alpha) = 1 - P(\alpha|\alpha) = \sin^2(2\theta)\sin^2\left(\frac{\Delta m^2 L}{4E}\right), \tag{1.14}$$

parameterised by just a single mixing angle and mass difference, and dependent on the L/E ratio. Even for extremely small differences in mass, the temporal distortion of the wavefunction can result in macroscopically tangible effects over large enough distances. The distance from the Sun, and the low energy of solar neutrinos allows probing into the region of mass differences of the order $10^{-10}\,\mathrm{eV}^2$.[5] The oscillation length in the vacuum between the Sun and Earth is given by the final term in Equation 1.14:

$$L_{vac} = \frac{4E}{\Delta m^2}. \tag{1.15}$$

1.4.2 The Matter Effect

In 1984 S. Mikheyev and A. Smirnov [16] incorporated L. Wolfenstein's hypothesis of the matter enhancement of neutrino oscillations [17] into their theoretical analysis of the passage of atmospheric neutrinos through the Earth. They also realised that the matter effect, later known as the MSW effect, could alter the passage of neutrinos through *any* region of high enough density such as those created in the core and envelopes of collapsing stars, and in particular, the Sun [18], because of the different interaction (amplitude for elastic forward scattering) for electron rather than for other types of neutrinos. The difference arises as the electron-type neutrino has an increased cross section of interaction

[5] for vacuum oscillations

with electrons as it may exchange a W or Z boson. Other types of neutrinos are limited to Z exchange as the only lepton for scattering in the Sun is the electron. Thus the vacuum oscillations are perturbed due to a difference in potential for electron and other flavour (α) neutrinos, which will depend on the electron number density for that particular medium, n_{e}:

$$\Delta V = V_{\mathrm{e}} - V_{\alpha} = \sqrt{2}\mathrm{G_F}n_{\mathrm{e}} \ , \tag{1.16}$$

in which $\mathrm{G_F}$ is the Fermi constant. The result is that there are new mass eigenstates for the propagation through matter; $\nu_1^m, \nu_2^m \neq \nu_1, \nu_2$. Since the mixing angle through matter, θ_{m}, is dependent on the matter eigenstates, it will necessarily differ from the mixing angle θ in the vacuum. The additional phase $\Delta\phi_{\mathrm{m}} = \Delta V t$ can be parameterised [19] in terms of a refraction length, L_{r}, which represents the electron-neutrino scattering length:

$$L_{\mathrm{r}} = \frac{\sqrt{2}\pi}{\mathrm{G_F}n_{\mathrm{e}}} \tag{1.17}$$

and is related to the mixing angle by

$$\sin^2 2\theta_{\mathrm{m}} = \frac{\sin^2 2\theta}{\left(\cos 2\theta - \frac{L_{\mathrm{vac}}}{L_{\mathrm{r}}}\right)^2 + \sin^2 2\theta} \ . \tag{1.18}$$

One can see from Equation 1.18 that the depth of the oscillation, $\sin^2 2\theta_{\mathrm{m}}$, exhibits a resonant character, dependent on the ratio of the oscillation length in vacuum and the matter-resultant refraction length. The resonant point occurs when $L_{\mathrm{r}}\cos(2\theta) = L_{\mathrm{vac}}$, so that even for very small values of θ_{m} maximal mixing can occur. Electron-type neutrinos are produced in the Sun over a range of distances, depending on which reaction they are produced in, and propagate through areas of varying electron density. When the passage out of the Sun goes through a region where the resonant condition can be satisfied, and the width of this region is larger than the oscillation length in matter, the oscillations are amplified.

The physical meaning of the matter effect is shown in Figure 1.2. Having been created as an electron neutrino, on reaching the resonant region the particle can continue its trajectory out of the Sun (and thus to Earth) as a different flavour neutrino. A varying density ρ causes a time dependence of the mixing angle, and in turn non-unique values of the neutrino mass states in matter, which are liable to propagate into each other. The smoothness of the electron density gradient in the Sun allows for an approximation

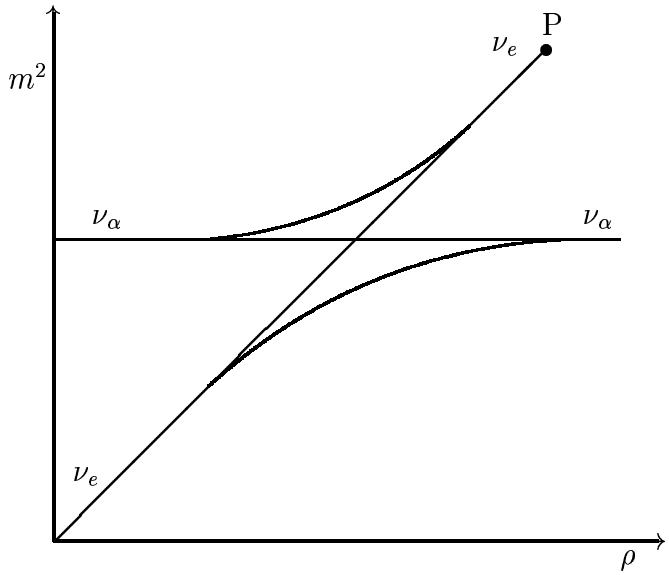

Figure 1.2: As an electron-type neutrino of flavour-dependent mass, created at a point P with a particular density, may change its flavour state to α as it travels through regions of slow varying electron density if it passes through the resonant point for enhanced oscillations [20].

to locally constant density, fulfilling what is known as the adiabaticity condition, and allowing the matter eigenstates to propagate independently.

The overall effect of matter enhancement is dependent on the position and width of the density region that allows resonance, the refraction length (dependent on n_e), and the oscillation length in vacuum, dependent on E_ν and Δm^2. Hence there is the possibility that the difference in neutrino mass states Δm^2 could give rise to distortion of the energy spectrum. Experiments such as Borexino, looking at neutrinos from the ^{7}Be reaction should be able to investigate lower parts of the energy spectrum (the only funded experiment capable of measuring energies below 5 MeV down to < 1 MeV) to further investigate any suppression in the energy spectrum, as well as allowing the probing of a spectrum other than that more commonly investigated, the ^{8}B chain. Whether there is any matter enhancement through the Earth is investigated by comparing the solar flux in the daytime, and in the night time. So far, no discernible asymmetry has been found

but statistics are limited and the effect is expected to be very small.

1.4.3 Dirac or Majorana?

For the neutrino to be massive it must have left and right-handed components. Although it only interacts through left-handed couplings to the weak currents, its chiral state may be expanded in terms of its helicity, which when massive consists of both positive and negative eigenvalues (through Lorentz boost arguments), the proportion of positive helicity states dependent on the actual mass. These positive and negative helicity states can then be expanded as left- and right-handed chiral states, allowing both possibilities from just one chiral interaction.

The neutrino may be a Dirac particle like all the other fermions in the SM, or it may be a Majorana particle. A Majorana particle is defined as being its own anti-particle, so viewing the particle in an accelerated frame of reference has the same effect as a transformation under both the charge and parity operators. The neutrino must be massive to allow for such an helicity flip under CP operations. All other fermions in the SM are Dirac particles since their charge always provides a unique distinction between a boosted particle and anti-particle state.

The character of the neutrino can be experimentally determined by looking at the total number of emitted neutrinos visible in double beta decay: two simultaneous β decays from the same nucleus. A neutron in an unstable nucleus can β decay and emit a right-handed anti-neutrino. If the anti-neutrino is the same as a neutrino, and in addition Lorentz-boosted, then this may be seen as a left-handed neutrino and can instigate the second β decay, producing a separate, second electron. The only visible particles from the decay are the two electrons. Hence indication of the neutrino as a Majorana particle is *neutrinoless* double beta ($0\nu\beta\beta$) decay. Conversely if the neutrino is a Dirac particle the final state anti-neutrino from the first β decay is not equivalent to the initial state neutrino of the second β decay and so both neutrinos and electrons will be emitted; $0\nu\beta\beta$ decay would never be observed. Current limits [21] from $0\nu\beta\beta$ decay experiments limit the mass of the [Majorana] neutrino to $\mathrm{m}_{\nu_e} < 0.35\,\mathrm{eV}$.

1.5 Experimental Evidence

Many experiments have been conducted over the last century to increase the understanding of neutrino properties. Certain experiments, presented below, have made significant contributions to determination of the oscillation parameters. Combined analysis of all these experiments through global fits allows much more stringent limits to be placed on the mixing angles and the mass differences.

1.5.1 Reactor Neutrinos

CHOOZ is a short baseline (one kilometre) reactor experiment [15], in a village of the same name in France. Completion of construction in March 1997 allowed background data to be taken before the two reactors (total thermal power 8.5 GW) it was sensitive to were switched on. The detection medium of five tonnes of Gadolinium-loaded liquid scintillator was surrounded by 192 PMTs with 15% coverage. The aim was to detect anti-neutrinos through the delayed coincidence of a positron (two 511 keV γ rays are released following annihilation), with a neutron (from an 8 MeV signal) to determine whether or not the flux had depleted over the distance. Running for one year collected 2991 candidate events and a background of 287 events from a period when both the reactors were off. No evidence was found of electron-type disappearance within the parameter range approximated by $\delta m^2 > 7 \times 10^{-4}\,\mathrm{eV}^2$ and $\sin^2 2\theta = 0.10$ for large δm^2 [15]. These results were derived from exclusion plots in $(\delta m^2, \sin^2 2\theta)$ with the assumption that the two neutrino model is valid.

KamLAND (**Kam**ioka **L**iquid scintillator **AN**tineutrino **D**etector) detects electron anti-neutrinos from 53 core reactors around Japan, of total thermal power flux over the detector livetime of 701 Jcm^{-2} [22]. A combination of 80% paraffin and 20% dodecane provides one ktonne of active scintillator, separated from a radioactive shield of buffer oil by a 13 m diameter plastic balloon, and surrounded by 1879 PMTs (34% coverage). The experiment is situated in the original Kamiokande cavity, flooded with water for further background suppression.

Each nuclear fission of 200 MeV yields about six $\bar{\nu}_e$, so knowing the total power output integrated over the distance to each reactor can determine whether there is an overall deficit. Anti-neutrinos above an energy threshold of 1.8 MeV interact as

in Equation 1.5. After a time delay of $\sim 200\mu$s the neutron captures on protons in the hydrocarbon scintillator, releasing a γ ray of 2.2 MeV which allows for coincidence tagging in time, space and energy. Data taking started in January 2002 and 515.1 days have now been analysed, equivalent to 766.3 tonne-year exposure. Only 258 events out of an expected 365.2 ± 23.7 (syst) and a background of 17.8 ± 7.3 were observed [22], where systematic errors are now equivalent to statistical ones. Assuming CPT (charge, parity and time) invariance and performing a two flavour global analysis severely limits the width of the Δm^2 region, as shown in Figure 1.3, to $\Delta m^2 = 8.2^{+0.6}_{-0.5} \times 10^{-5}\,\mathrm{eV}^2$. The results do not have much impact on the global best fit value of $\tan^2\theta = 0.40^{+0.09}_{-0.07}$.

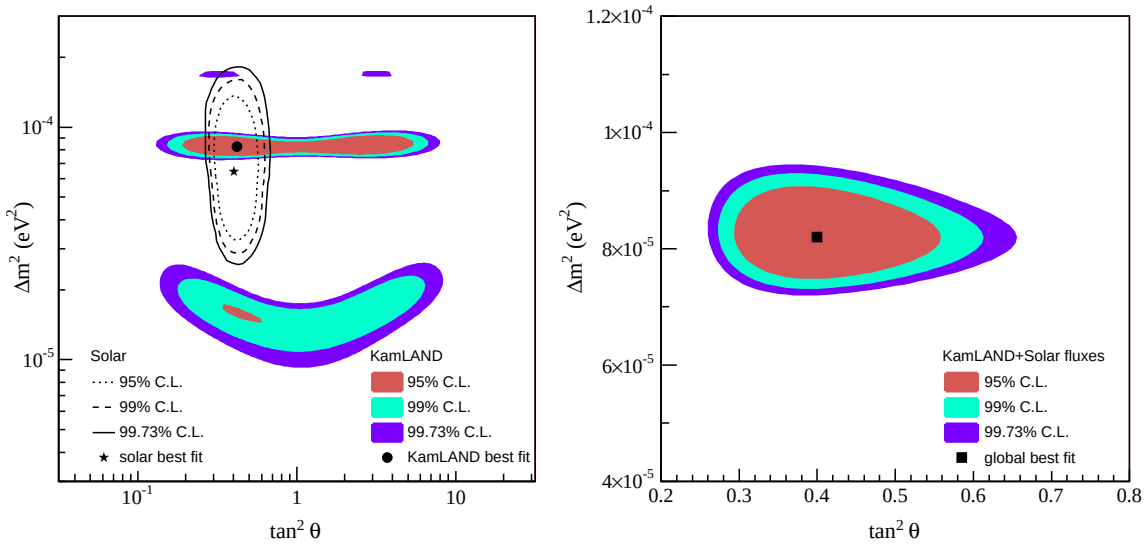

Figure 1.3: The current best fit parameters provided by 515.1 days of KamLAND data are shown in combination with other experiments to yield global values of Δm^2 and $\tan^2\theta$. Figure taken from [22].

1.5.2 Atmospheric Neutrinos

Super-K, the upgrade to Kamiokande (Kamioka **n**ucleon **d**ecay **e**xperiment), which was originally designed to investigate the very different problem of nucleon stability, is a cylindrical ultra-pure light water Čerenkov detector that looks for atmospheric neutrinos from cosmic ray interactions. The neutrino interacts (Equation 1.19) via electron-neutrino scattering, where x represents a neutrino of any flavour, but the

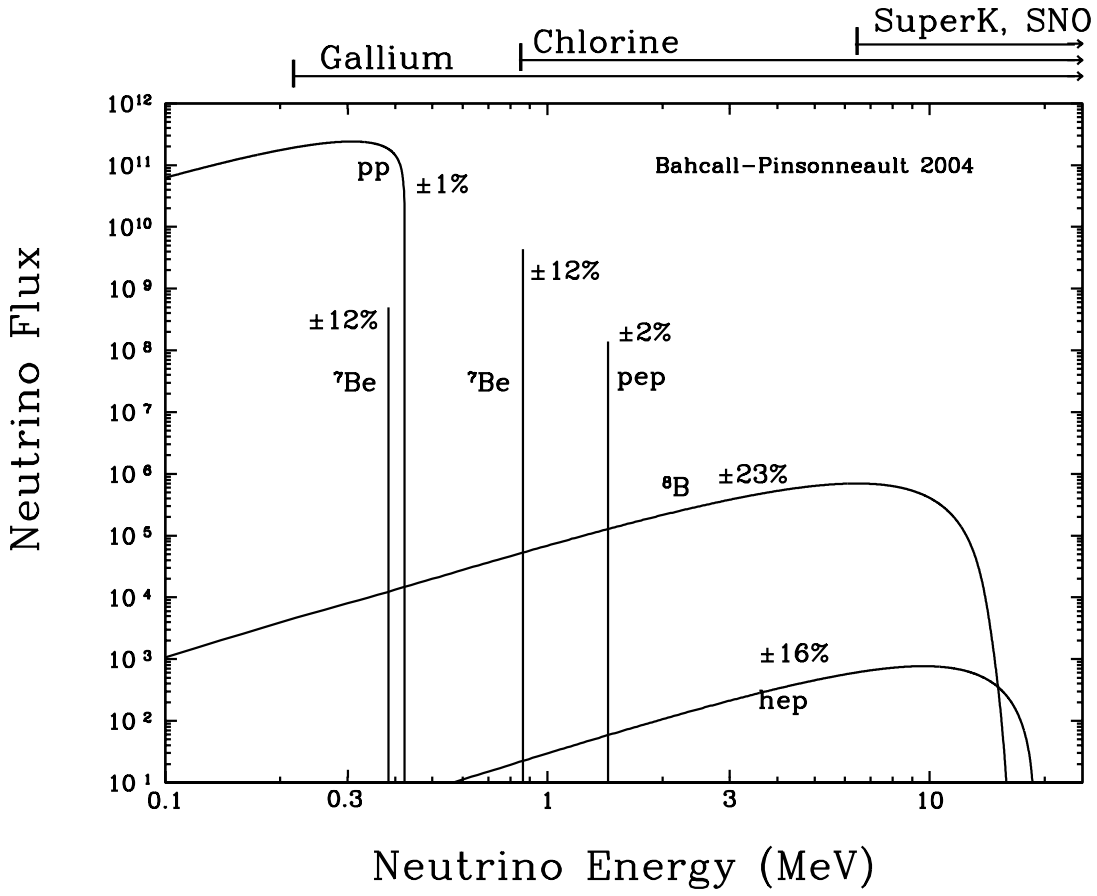

Figure 1.4: The energy range of the different neutrino fluxes that are produced in the Sun as calculated by Bahcall and Pinsonneault in their BP04 model. Figure taken from [23].

reaction has enhanced sensitivity to electron-type neutrinos. It is also sensitive to ^{8}B solar neutrinos.

$$\nu_x + \mathrm{e} \rightarrow \ \nu_x + \mathrm{e} \tag{1.19}$$

The light from the recoil electrons emitted in the scattering of Equation 1.19 is detected by the 11146 50 cm diameter PMTs that focus on the inner fiducial region of 22.5 ktonnes H_2O. An outer region of 18 ktonnes is used to veto out background radiation from the cavity and cosmic muons.

The neutrinos are expected in the ratio ($\nu_\mu/\nu_e \equiv 2$) from the reactions:

$$\begin{aligned} \pi^+ &\rightarrow \ \mu^+ + \nu_\mu \\ \mu^+ &\rightarrow \ \bar{\nu_\mu} + \mathrm{e}^+ + \nu_\mathrm{e} \end{aligned} \tag{1.20}$$

Since the neutrinos are produced in the atmosphere, there is a large difference in the distance travelled between the upward going neutrinos that have passed through the Earth, and the downward going ones, with a continuous distance spectrum over the zenith angle. Those identified as muon neutrinos exhibit a strong zenith

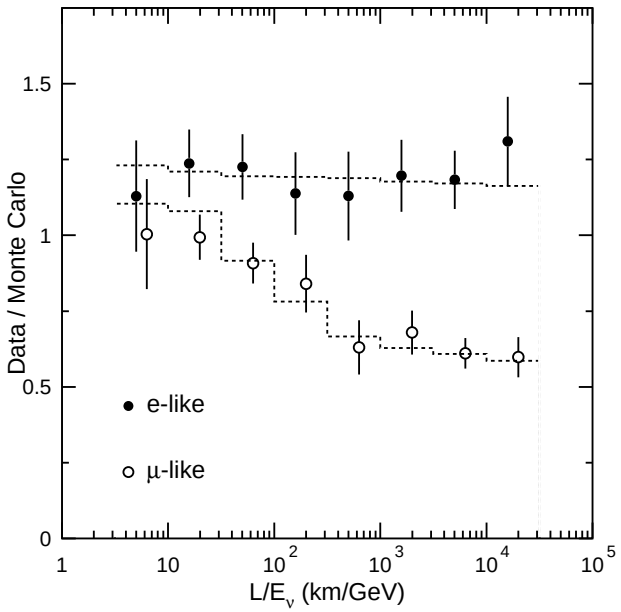

Figure 1.5: Flavour oscillations could explain the deficit of μ neutrinos over larger distances seen at Super-K. Plot taken from [24].

angle asymmetry, indicating that the large distances could have allowed flavour

oscillations, as shown in Figure 1.5. This effect is not seen for the electron-like neutrinos which allows limits to be placed [24] on the oscillation parameters for ν_μ for $\nu_\mu \rightarrow \nu_\tau$. The best fit oscillation parameters from the Super-K results are a squared mass difference $\Delta m^2 = 2.5 \times 10^{-3}\text{eV}^2$ and a value of the mixing angle between ν_2 and ν_3 given by $\sin^2\theta_{23} = 1.0 (\sin^2\theta_{23} > 0.96$ at the 90% confidence level).

1.5.3 Solar Neutrinos

GALLEX (**Gall**ium **Ex**periment), upgraded to **GNO** (**G**allium **N**eutrino **O**bservatory), and **SAGE** (**S**oviet **A**merican **G**allium **E**xperiment) are radiochemical experiments measuring $^{71}\text{Ga} \rightarrow {}^{71}\text{Ge}$ conversion through electron neutrino capture. The extremely low energy threshold of 233 keV allows unique measurement of solar neutrino fluxes from the pp and ^{7}Be reactions (see Figure 1.4), responsible for 91% and 7% of the total solar neutrino flux respectively. They can be deconvoluted from the other solar neutrino fluxes by comparison with results from other experiments.

SAGE uses 50 tonnes of liquified metallic ^{71}Ga housed in seven chemical reactors, and is protected from the cosmic muon flux by the 4700 m water equivalent (mwe) rock overburden of the Caucasus mountains at the Baksan Neutrino Observatory. ^{71}Ge atoms are extracted every month by flushing the reactors. After removal, gaseous Germane is produced which can be used in a proportional counter, and the subsequent ^{71}Ge decays are monitored by fitting out the half life to infer the neutrino flux.

Similar techniques are used to extract the ^{71}Ge atoms from the Gallex and GNO experiments based in Gran Sasso, the main difference from SAGE being that a liquid target of 101.3 tonnes of $GaCl_3$ is employed.

The combined averaged flux from these experiments, over 12 years for SAGE and 14 years for Gallex and GNO, is 68.1 ± 3.75 SNU, where one solar neutrino unit (SNU) is equivalent to one capture per 10^{36} atoms per second. It is in considerable disagreement with the theoretical prediction of 128 ± 8 SNU.

1.6 SNO

All of the above experiments show a deficit in the flux of neutrinos. The results may be explained by neutrino oscillations, but for definite proof it must be shown that the overall neutrino flux exceeds the flux of electron-type neutrinos, from a particular spectrum. The Sudbury Neutrino Observatory was explicitly designed for such a purpose. It was proposed in 1985 [25] as an experiment to detect both the *total* and *electron-type* flux of solar neutrinos from the ^{8}B chain.

It is a heavy water Čerenkov imaging detector. Signals are produced by the emergent particles from neutrino inelastic scattering off, or splitting apart of, the deuteron, or by electrons scattered in elastic interactions with electron-type neutrinos. Different flavours of neutrinos will undergo different physical processes within the detector and produce different Čerenkov light signals:

- all flavours of neutrino may interact via the neutral current (NC) reaction (splitting of the deuteron)
- all flavours of neutrino may scatter off electrons (ES) in the D_2O although the reaction is more sensitive to electron-type neutrinos
- electron-type neutrinos may interact with quarks inside the deuteron through the charged current (CC) reaction

The events can not be deconvolved to indicate the flavour of neutrino on an event-by-event basis and so a maximum likelihood signal extraction technique is used to separate the neutrinos according to which reaction they have undergone.

Results from the first phase (pure D_2O) showed excellent agreement between SSM predictions of the total active flux of solar neutrinos from the ^{8}B spectrum, and the total number of neutrino events. The results also showed that the number of electron-type only neutrinos was far lower than the total flux, implying that there was a $\nu_{\mu,\tau}$ component within the total flux:

$$\phi(\nu_e) = 1.76\ ^{+0.05}_{-0.05}\ (\text{stat})\ ^{+0.09}_{-0.09}\ (\text{syst})\ \times 10^{-6}\text{cm}^{-2}\text{s}^{-1}$$
$$\phi(\nu_{\mu,\tau}) = 3.41\ ^{+0.45}_{-0.45}\ (\text{stat})\ ^{+0.48}_{-0.45}\ (\text{syst})\ \times 10^{-6}\text{cm}^{-2}\text{s}^{-1}\ .$$

The salt phase had enhanced sensitivity to the NC reaction, and also allowed for better statistical separation between the three types of signal. This separation allowed for an

energy unconstrained fit to be performed, in which there were no assumptions about the spectral shape of ^{8}B solar neutrinos. The total flux and electron-type only flux were calculated as:

$$\phi(\nu_e) = 1.68\ ^{+0.06}_{-0.06}\ (\text{stat})\ ^{+0.34}_{-0.38}\ (\text{syst})\ \times 10^{-6}\text{cm}^{-2}\text{s}^{-1}\ .$$
$$\phi(\nu_{\text{total}}) = 4.94\ ^{+0.21}_{-0.21}\ (\text{stat})\ ^{+0.09}_{-0.09}\ (\text{syst})\ \times 10^{-6}\text{cm}^{-2}\text{s}^{-1}$$

If a global analysis is performed (SNO data is combined with measurements from other experiments) then the best fit values for the mixing parameters are $\Delta m^2 = 8.0^{+0.6}_{-0.4} \times 10^{-5}\text{eV}^2$ and $\theta = 33.9^{+2.4}_{-2.2}$ degrees, assuming a two-neutrino analysis. The data strongly prefer the large mixing angle (LMA) solution to the solar neutrino problem.

1.7 Thesis Outline

The SNO results required a detailed understanding of the backgrounds that could mimic the NC reaction. This thesis describes the determination of the deuteron photodisintegration background from naturally occurring radioactive decay chains.

The detector, detection signals and experimental phases are discussed in more detail in Chapter 2. Chapter 3 explains the determination of a good quality data set. It details how the events are reconstructed and how the majority of backgrounds which have unique characteristics can be separated from good neutrino data using their timing information, and spatial and charge distributions. It also outlines the determination of a period of particularly high background within the possible data set and the implementation of a criterion to prevent future occurrences within the data set. Chapter 4 explores the current theories and predictions for the cross section of deuteron photodisintegration and compares the reults to the modelling within the simulations. Chapter 5 identifies the main sources of naturally occurring radioactive backgrounds that caused deuteron photodisintegration within the salt phase and Chapter 6 presents a method of separating the backgrounds such that the number of photodisintegration neutrons from each background may be calculated. The number of expected neutrons from photodisintegration neutrons within the data set, as well as other sources of neutron backgrounds, must be subtracted from any extracted number of NC events, to convert a measure of the number of neutrons within the analysis region to a number of neutrinos. Finally, Chapter 7 uses a maximum likelihood fit to extract the neutrino signals and backgrounds down to a kinetic energy of 4 MeV through implementation of an energy-dependent fiducial volume.

Chapter 2

The SNO Detector

The Sudbury Neutrino Observatory exploits the unique set of neutrino reactions on D_2O to measure both the flux of ν_e and the total active neutrino flux of solar neutrinos from the ^8B spectrum [25]. The primary method of detection is to observe Čerenkov radiation emitted by relativistic electrons associated with the neutrino interactions. The ultra-pure D_2O is contained within an acrylic vessel (AV) of 12 m diameter and surrounded by 1700 tonnes of pure H_2O and the light is detected by 9456 photomultiplier tubes (PMTs) mounted on an exoskeletal support structure 17.8 m in diameter. The light water shields out radioactivity from this structure. SNO is located 2039 m underground in INCO's Creighton Mine, Sudbury, Canada, in a specially excavated cavity 22 m in diameter and 34 m tall, shown in Figure 2.1.

The detector is shielded from cosmic rays and muons by the norite rock overburden of the mine. This provides an equivalent water depth of 6000 m and reduces the muon flux inside the detector to $\sim 70\,\mathrm{day}^{-1}$. The rest of the cavity is flooded with 5300 tonnes of H_2O, which acts as support, and a muon veto, as well as providing additional shielding from radioactivity within the rock.

This chapter details the particle detection principles and describes the PMTs, acrylic vessel, electronics and water systems that each play an integral part in the detector. There is also a section on detector calibrations.

2.1 Neutrino Detection

Čerenkov light is radiated if the velocity of a charged particle is faster than the phase velocity of light in the media in which it is travelling. The shockwave of light forms a

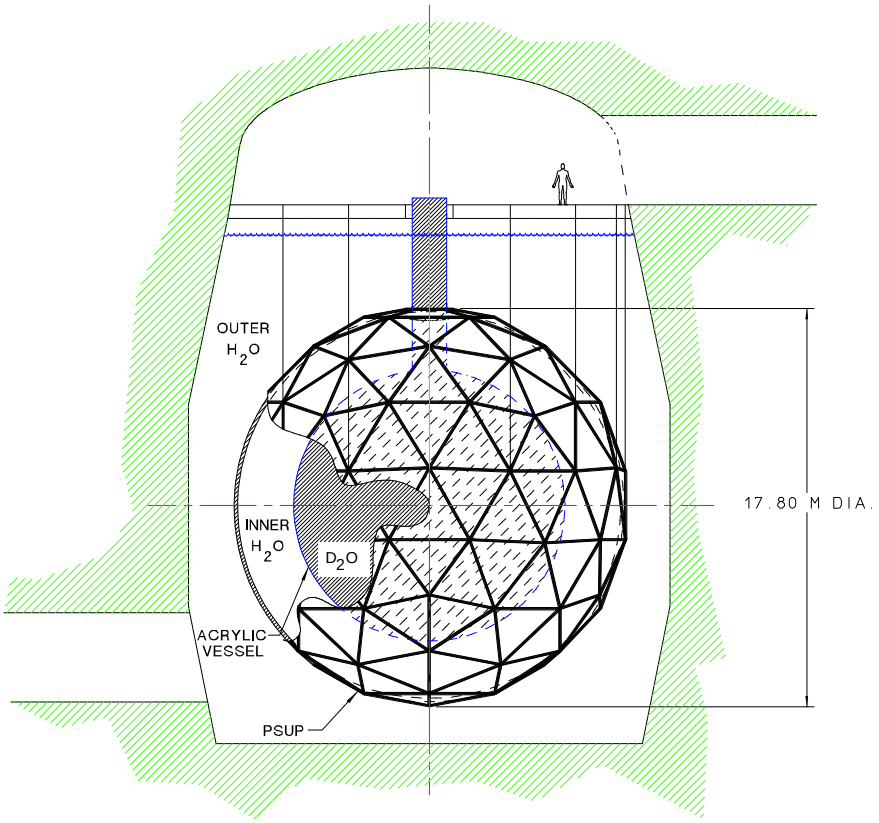

Figure 2.1: The PMT support structure shown inside the cavity, surrounding the acrylic vessel, with light water and heavy water volumes located as indicated. Figure taken from [26].

cone, with half angle θ to the direction of motion of the particle given by

$$\cos(\theta) = \frac{1}{n\beta} , \tag{2.1}$$

where β is the ratio of the velocity to the phase speed of light in vacuum, and n is the refractive index of the medium. The refractive index averaged over the Čerenkov spectra for D_2O is 1.333, so $\theta \simeq 41°$ for a relativistic electron. The number of photons, N, over a wavelength range λ_1 to λ_2 is linearly proportional to the path length x of the moving particle and thus closely related to its energy,

$$N = 2\pi\alpha \int_{x_1}^{x_2} \int_{\lambda_1}^{\lambda_2} \frac{d\lambda}{\lambda^2} \left(1 - \frac{1}{\cos^2(\theta)}\right) dx \tag{2.2}$$

For an electron in the energy range of interest ($5 - 15\,\mathrm{MeV}$) and a wavelength range $\sim 250-550\,\mathrm{nm}$, about 440 photons are emitted per centimetre. Since it typically travels $\sim 0.45\,\mathrm{cm}$ per MeV of energy [27] about 200 photons are produced for every MeV of electron energy, providing the kinetic energy is above the Čerenkov threshold of 0.262 MeV. As the PMTs plus the reflectors provide $\sim 50\%$ coverage and the quantum efficiency for photon detection is $\sim 10\%$, a 5 MeV electron will produce about 50 PMT hits.

2.1.1 Charged-Current

The charged-current (CC) interaction is the primary method in SNO for detecting electron-type neutrinos. Those above an energy threshold of 1.44 MeV [28] can exchange a W^+ boson with a d-quark in a deuteron nucleus D,

$$\nu_e + D \rightarrow p + p + e^- - 1.44\,\mathrm{MeV} , \tag{2.3}$$

where the electron acquires an energy approximately 1.44 MeV less than the neutrino, allowing inference of the neutrino energy spectrum. As the electron is typically emitted heading in the direction of the neutrino there is slight directional sensitivity to the solar flux of approximately $1 - \frac{1}{3}\cos\theta_\odot$, where $\theta_\odot$ indicates the direction of travel with respect to the position of the Sun. The reaction is a pure allowed Gamow-Teller transition as the two protons emerge in the singlet S state. The integrated product of flux and cross-section has been calculated [28] within the scope of the assumptions[1]; that the electron is a free particle, retardation is negligible and the effective range approximation is valid (see chapter 4), as $2.3 \times 10^{-35}\,\mathrm{sec}^{-1}$ per deuteron for solar neutrinos from the ^8B flux.

[1] generally assumed to be a very good approximation

2.1.2 Elastic Scattering

Although neutrinos of all types will elastically scatter off electrons, the cross section is about 6.5 times larger for an electron-type neutrino as it is not limited to Z^0 exchange.

$$\nu_e + e^- \rightarrow \nu_e + e^- \tag{2.4}$$

The elastic scattering interaction (ES) can be distinguished from CC interactions through the strong directional correlation of the cone of Čerenkov light from the outgoing electron with the incoming neutrino. The low cross section for this reaction inhibits its use as the primary detection of electron-type neutrinos. There is less information on the energy of the incident neutrino since the energy is shared between the two outgoing particles. The differential cross section is exactly calculable from electroweak theory as demonstrated by 't Hooft [29]:

$$\frac{d\sigma}{dT_e} = \frac{2G_F^2 m_e}{\pi}\left[g_L^2 + g_R^2\left(1 - \frac{T_e}{E_\nu}\right)^2 - g_L g_R\left(\frac{m_e T_e}{E_\nu^2}\right)\right] \tag{2.5}$$

$$(g_L = (0.5 + \sin^2\theta_W) \text{ for electrons, } g_R = \sin^2\theta_W,\ \sin^2\theta_W = 0.23)\ ,$$

where G_F, m_e, T_e, and E_ν are the Fermi coupling constant, the electron rest mass, the electron recoil kinetic energy, and the incoming neutrino energy respectively.

2.1.3 Neutral-Current

SNO relies on an accurate determination of the total flux of ^8B solar neutrinos via the neutral-current (NC) reaction on the deuteron nuclei;

$$\nu_x + D \rightarrow p + n + \nu_x\ , \tag{2.6}$$

and subsequent neutron detection, where x represents any [active] flavour of neutrino. The threshold for this reaction is the binding energy of the deuteron: 2.225 MeV. Thermalisation of the neutron eliminates any directional sensitivity.

There are three separate detection methods for each of the three phases of SNO to track the neutron from the NC reaction, as described below.

Phase I - Pure D_2O

The neutron may capture on a deuteron nucleus, Eqn 2.7, producing an excited

state in tritium which emits a single monoenergetic γ ray on its decay to the ground state,

$$n + D \rightarrow \ t^* \rightarrow \ t + 6.25\,\mathrm{MeV}\ . \tag{2.7}$$

The subsequent amount of Čerenkov light is equivalent to a $\sim 5\,\mathrm{MeV}$ electron, as it predominantly interacts through the Compton effect and undergoes several scatterings.

Phase II - Addition of Salt

The neutron capture rate was enhanced in Phase II through the addition of two tonnes of salt (NaCl) to the D_2O. There is still the possibility of capture on deuterium but the most likely ($\simeq 90\%$) neutron capture is on ^{35}Cl, Eqn 2.8, releasing a cascade of γ rays of total energy 8.6 MeV.

$$^{35}\mathrm{Cl} \rightarrow \ ^{36}\mathrm{Cl}^* \rightarrow \ ^{36}\mathrm{Cl} + \Sigma[8.6\,\mathrm{MeV}] \tag{2.8}$$

The extremely complicated decay scheme is comprised of 398 [30] routes to the ground state (measured as $\geq 10^{-5}$). There are 23 strong transitions, and those whose intensity exceeds 10% are shown in Table 2.1, along with the direct decay to the ground state of intensity 2.78%, the probability of producing a single γ ray.

E (keV)	I (%)
517.077	23.4
786.303	11.2
788.433	16.9
1164.87	27.7
1951.15	20.2
1959.36	12.9
6110.84	20.2
7413.97	10.4
8578.59	2.78

Table 2.1: Strong ($\geq 10\%$) transitions observed in ^{35}Cl(n,γ) reaction compared to the internal transition directly to the ground state.

Simulations of these cascades show that between two and three γ rays [31] is the most likely number detected. The γ rays primarily Compton scatter off the electrons

in the D_2O, and electrons with kinetic energy greater than 0.262 MeV each produce a cone of Čerenkov light.

Phase III - Neutral-Current Detectors (NCDs)

SNO is currently in its third, and final configuration. An array of 36 ^{3}He proportional counters provides an additional and uncorrelated method for neutron detection:

$$n + {}^3He \rightarrow t + p + 0.764\,MeV\ ; \tag{2.9}$$

subsequent pulse shape analysis is used to isolate the neutrons. The counters, of total length 398 m, shadow the PMTs slightly (collecting data in parallel), reducing the light collected by a maximum of 12%. This can be determined by comparing ^{16}N source deployment in the centre of the detector before and after NCD installation.

2.2 Water Systems

Both the D_2O and H_2O required purification [32] before the levels of intrinsic radioactivity, primarily from Uranium (^{238}U) and Thorium (^{232}Th), were low enough that they would not dominate signals from neutrino interactions. The light water is continually purified through circulations and different types of assays allow monitoring of the main contaminants. The heavy water is circulated every two weeks to monitor the activity. All plastic components in the water systems (the smaller storage tanks and about 140 m of piping) are made from polypropylene, chosen for its low level of leaching.

N_2 cover gas prevents the ingression of ^{222}Rn (a daughter of the ^{238}U chain) from the laboratory air, which at levels of 3 pCi/l would overwhelm any neutrino signal. There are separate cover systems for the light and heavy water. The N_2 barrier must be sufficient and the amount may be altered to reflect any changes in air pressure in the laboratory. It is important that the barrier is continually present and so the gas is constantly replenished to replace boil-off. It should also be relatively free of Rn contamination itself; levels have been measured to $< 10^{-5}$ pCi/l. The only viable way for Rn to then enter the system is when internal components (*e.g* filters or pumps) are replaced or repaired, and even then D_2O is flushed through.

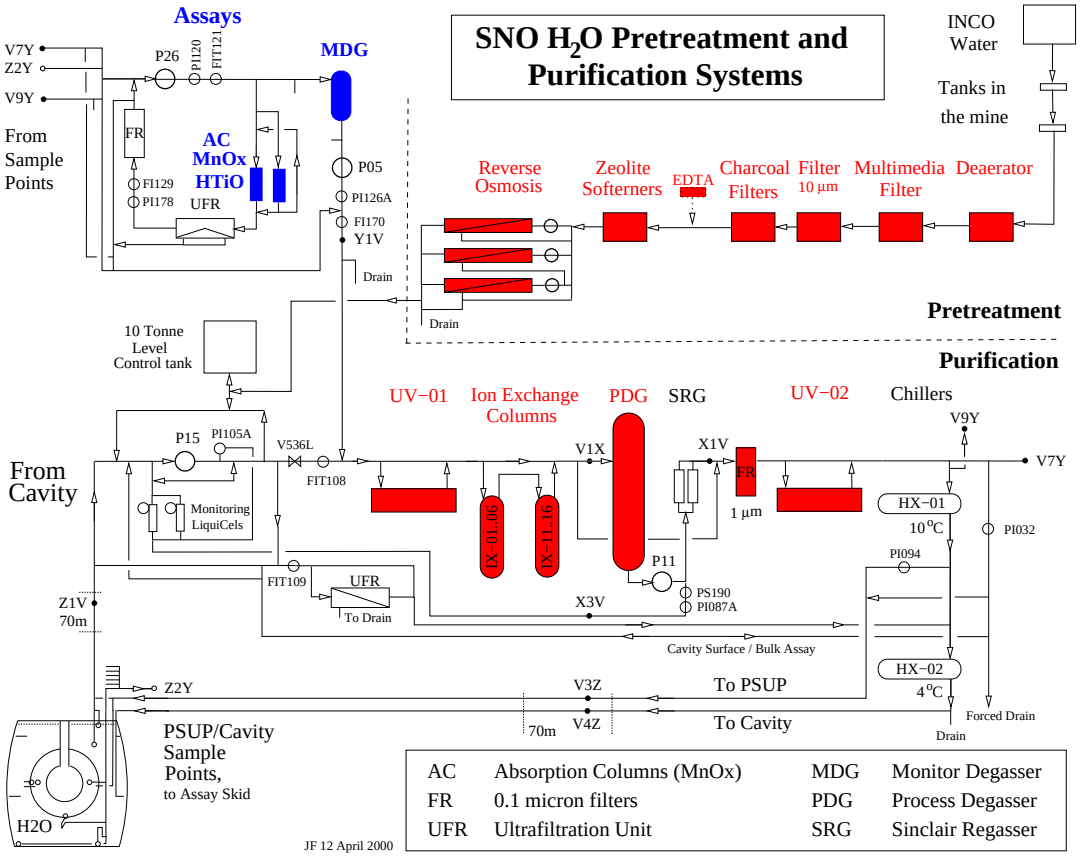

Figure 2.2: Overview of the light water systems. Figure kindly provided by J. Farine.

2.2.1 Light Water

The first step in the ultra purification process after initial degassing was filtration; sandbeds extracted large particles and a charcoal filter removed organic compounds from the H_2O. Softeners removed Ca, Mg and dissolved Fe from the water. A reverse osmosis and ion exchange system reduced levels of inorganic salts and removed soluble ionised impurities. The effectiveness of all these stages can be seen from data in Table 2.2, taken from Ra

Water Sampled Following:	Sample (tonnes)	^{232}Th (g/g)	^{238}U (g/g)
Charcoal Filter	5	$6.3 \pm 1.2 \times 10^{-11}$	$4.2 \pm 1.2 \times 10^{-12}$
	5	$9.3 \pm 1.8 \times 10^{-11}$	$1.2 \pm 1.2 \times 10^{-11}$
Softener	5	$3.7 \pm 1.1 \times 10^{-13}$	-
	5	$7.8 \pm 2.0 \times 10^{-13}$	-
Reverse Osmosis	42	$1.2 \pm 0.5 \times 10^{-14}$	-
	31	$2.8 \pm 0.8 \times 10^{-14}$	$1.1 \pm 0.3 \times 10^{-14}$
Ion Exchanger	29	$3.6 \pm 2.5 \times 10^{-14}$	-

Table 2.2: Verification from Ra assays that the combination of purification procedures does reduce the levels of contaminants in the light water systems.

assays when the water systems were initially tested. The lack of a large number of samples limits the numerical accuracy but indicates the order of magnitudes gained at each stage. A process degasser removes all the gases in the water to reduce the Rn and O_2 levels. Complete gas removal allows diffusion across the PMT connectors, and because low pressure causes tube breakdown, the water is regassed with N_2 before it enters the detector, having been cooled to 10° C. The low temperature reduces the PMT noise. Circulation removes any heat generated in the water by the electronics and from the rock, as well as being an inhibitive environment for the growth of biological organisms. Maintaining constant temperature ensures uniform density of the media. If the H_2O level needs to be adjusted, reserves can be added from (or bled into) the 10 tonne level control tank, before rejoining the main circuit, as shown in Figure 2.2.

2.2.2 Heavy Water

The D_2O is on loan from Atomic Energy of Canada and must, at some stage, be returned. It has never been used in a nuclear reactor (which might render the media useless because

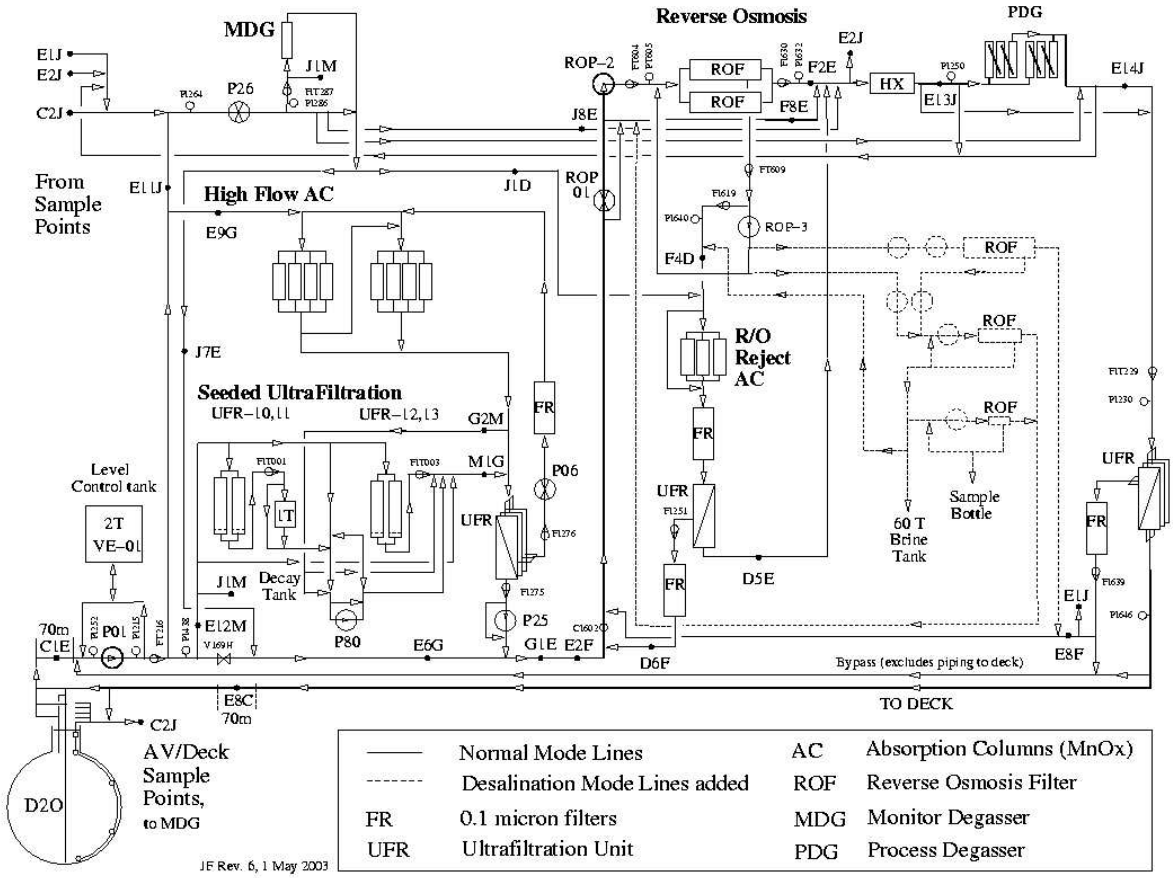

Figure 2.3: Overview of the heavy water systems. Figure kindly provided by J. Farine.

of signals from tritium) and, having isotopic purity of 99.92%, has very low levels of hydrogen which has a relatively large neutron capture cross section. It demands careful handling because of its very high value.[2] Any purification system must ensure that no D_2O is lost and that isotopic purity is maintained to avoid degradation of the NC signal.

Ion exchange columns initially reduced the ionic content of the D_2O before it entered the vessel. Regular circulations pass the D_2O through adsorption columns to assay ^{232}Th, ^{238}U and ions. There is a two tonne level control tank (also referred to as the reserve tank) which contains reserve D_2O for level adjustments. Before returning to the vessel, the D_2O enters an ultrafiltration unit, which extracts trace amounts of the absorbers used in the assays. The design also allows for the addition of salt (NaCl) to the heavy water and its removal (to ~ 1 ppb), through reverse osmosis.

2.2.3 Assays

HTiO

For an HTiO assay either D_2O or H_2O is passed through membrane filters coated with hydrated Titanium Oxide (HTiO) onto which Ra from ^{232}Th and ^{238}U will be adsorbed. The flow rate is 100 l/min and passes through two membranes connected in parallel [33] to allow the passage of $\sim$ 400 tonnes of D_2O in a time period comparable with the half life of ^{224}Ra, 3.66 days. The filters are removed and the Ra can be extracted onto membranes. It is eluted with nitric acid and reduced to a 10 ml volume. It can then be combined with liquid scintillator and $\beta-\alpha$ coincidence counters allow a direct measurement of the Ra levels in the assayed water.

MnO_x

Figure 2.3 shows how D_2O, taken from one of six sample points located at various depths close to the wall of the acrylic vessel may be assayed. There are also six monitoring points for the H_2O, the most frequently sampled being that between the AV and the PMTs where the most important H_2O backgrounds will originate. The water flows at a rate of 20 l/min through one of four columns filled with compound Manganese Oxide (MnO_x) coated beads, onto which Ra dissolved in the water will be adsorbed. After an assay the columns can be removed, dried and placed above an

[2] Note also that D_2O is slightly toxic if ingested.

electrostatic chamber. The ^{226,224}Ra α decays to ^{222,220}Rn which follows a series of decays to give ^{212,214,216,218}Po, from whose decay spectra the levels of ^{238}U and ^{232}Th can be estimated, respectively. The charged Po ions are attracted to solid state α detectors and can be counted to estimate contamination levels for that assay. The detection limit is of the order 10^{-16} g/g ^{232}Th,^{238}U. Before rejoining the system the water must be passed through the ultra-filters which remove any traces of MnO_x from entering the AV [34].

Vacuum Degassing

From the same six sampling points in the systems, water is taken to monitor degassers to measure ^{222}Rn levels. This ensures accurate monitoring in case of substantial disequilibrium in the chain, possible if there is Rn leakage into the system. The degassers can free a few hundred atoms of ^{222}Rn from the water, flowing at a rate of 20 l/min. Cooling with liquid nitrogen freezes the Rn from the other liberated gases, and it can subsequently be released and counted in a Lucas cell scintillator.

2.3 The Acrylic Vessel

A 12 m diameter acrylic ($C_2H_5O_8$) sphere of thickness 5.5 cm (thickened in regions of support) separates the D_2O from the shielding H_2O. A sphere has the largest volume-to-surface ratio and optimum stress distribution. The geometry is also simple to model. The water levels across the vessel are carefully monitored and adjusted to avoid a pressure gradient causing undue stress. At the top there is a centrally placed 1.5 m diameter acrylic chimney, or neck, that extends up 6.8 m for calibration source deployment. The acrylic was designed to have very low levels of radioactivity (^{232}Th and ^{238}U levels both measured at < 1.1 pg/g [26]). It has good optical transmission over the visible spectra but has a lower cutoff of ~ 300 nm.

2.4 Photomultiplier Tubes

The cross section of the PMTs used in SNO is shown in Figure 2.5. The inner surface of the evacuated curved glass shell is coated with a thin layer of photocathode from which electrons can be released by photons via the photoelectric effect. The quantum

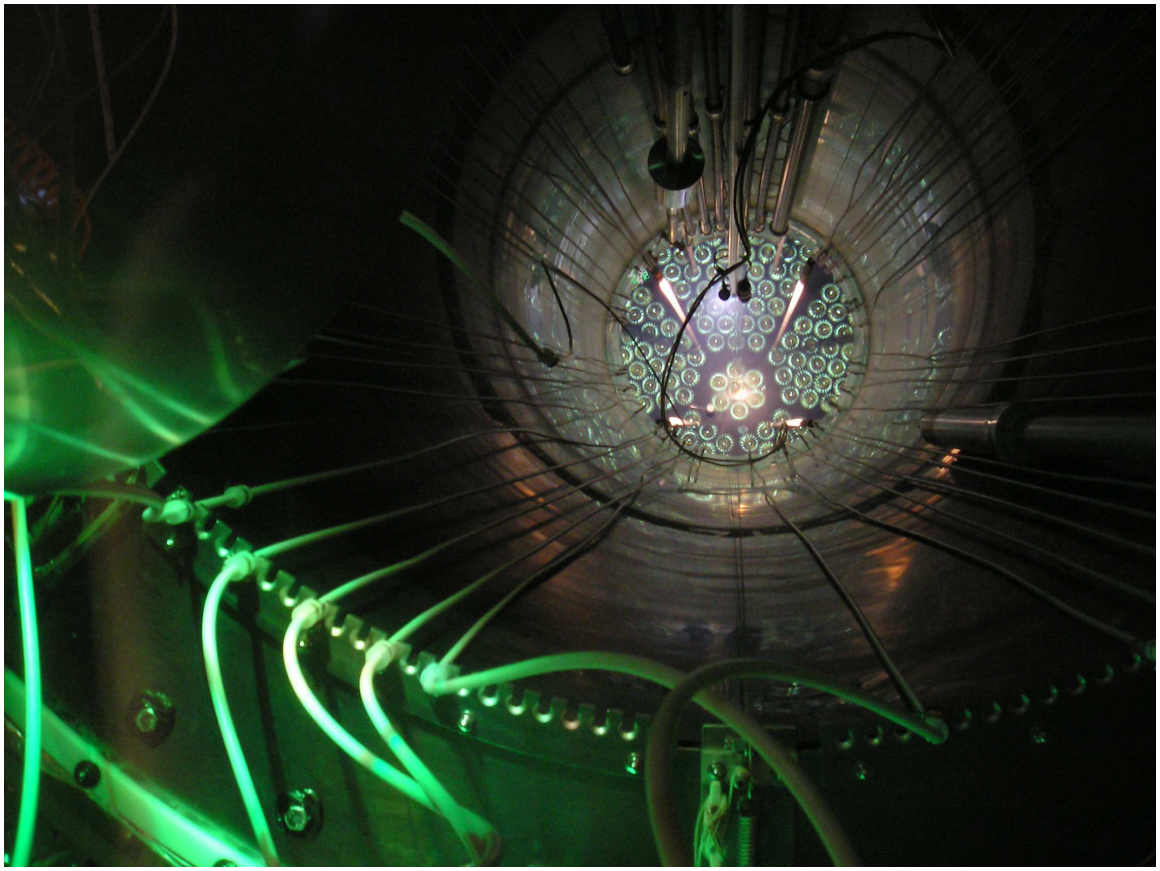

Figure 2.4: A view down the neck of the acrylic vessel showing the PMTs at the bottom of the detector. This picture was taken during the deployment of the neutral-current detectors, some of which are visible anchored in their array positions.

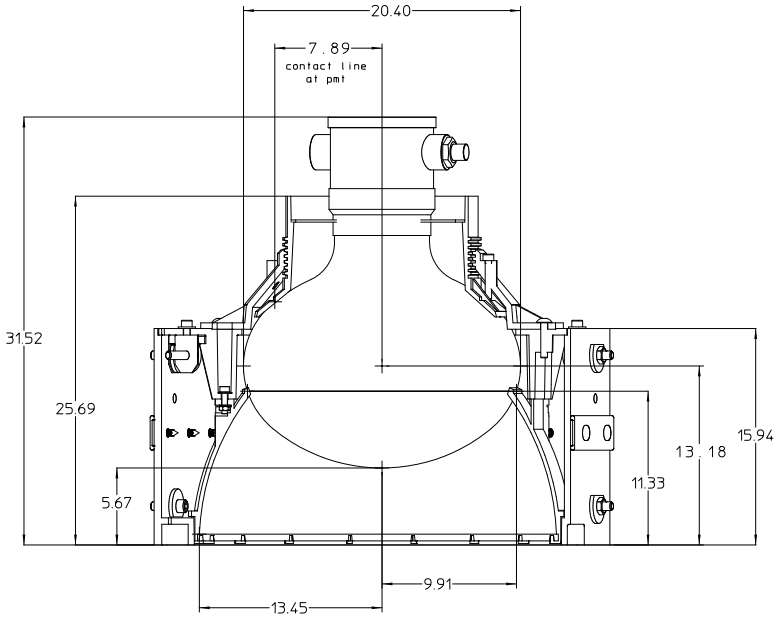

Figure 2.5: A cross section of a Hamamatsu R1048 PMT, with dimensions given in centimetres. Figure taken from [26].

efficiency for this photocathode over the range 250-500 nm is $sim10\%$ [35] and the electron acceleration time from the cathode to the anode is ~ 30 ns, with a spread of 1.5 ns. The signal is amplified through a nine chain dynode stack with total gain of approximately 2×10^7. A 75 Ω cable (length $\sim$ 33.5 m) for each PMT provides the operating voltage, between 1700 V and 2100 V, and transports the signal to the front end electronics via a PMT interface card. Magnetic compensation coils surrounding the detector balance out the vertical component of the Earth's magnetic field, reducing the effect of the Earth's field on the gain to an insignificant level.

The PMTs in SNO have levels of intrinsic radioactivity that are a factor of 14 lower than the design specifications [36], < 120 ng/g ^{238}U and < 90 ng/g ^{232}Th, mainly because of the minimal levels in the custom made glass.[3] They are highly water resistant, crucial since they must be submerged for the entirety of the experiment and cannot be replaced, demanding a low failure rate.

All the inward looking PMTs are housed in separate 27 cm diameter black plastic hexagonally shaped Winston cone concentrators allowing 85% tessellation across the stainless steel tubular panelled support structure. The inner surface of the concentrator is

[3]The units of g/g indicate the number of grammes of contaminant per gramme of material

made of aluminium strips coated with ($\lambda/4$)-thick layers of differing refractive indices, to enhance the reflectivity (and provide protection from water corrosion), thereby increasing the effective coverage of the photocathode from 31% to 59%. The 56° angular cutoff of the concentrator limits the view of the PMT to the centre of the detector and ~1 m of light water, which enhances the signal to background ratio.

There are 91 outward looking PMTs to veto external events, in particular muons, and 49 PMTs are low gain for large burst event analysis. Four smaller tubes reside at the top of the neck and veto light originating in the neck region (possibly from static discharge of the acrylic). A further 23 tubes monitor the continuous effect of submersion in D_2O and are positioned near the top of the support structure for ease of removal.

Tubes gradually fail over time at a rate of about two a week, mostly due to breakdown induced by submersion in water. These are not replaced so the number of working tubes is constantly decreasing which will contribute towards a finite lifetime of the detector.

2.5 Electronics

The front end electronics in SNO, shown schematically in Figure 2.6, were custom designed [37] to record the analogue signals from the PMTs and convert this to digital signals for comparison with the specified trigger settings. The advantage of an analogue trigger is its speed as there is no summation involved at that stage; the time taken for a global trigger to reach the front end electronics is dominated by the $\sim$ 240 ns of transmission along the length of the cables. Although the average rate is $\sim$ 20 Hz, the system can support short term bursts of events of upto 2 MHz, as would be generated by a supernova.

Each of the 32 channels on a PMT interface card interfaces with an individual PMT. There are 16 interface and front end cards per crate and 19 crates, allowing for up to 9728 signals from PMTs in the array.

The signal of eight PMTs is passed to one of four daughter boards on the front end card and fires a discriminator if the signal exceeds the specified threshold. This releases two discrete pulses integrated over 100 ns and 20 ns. The 100 ns-width pulse includes all the prompt light (transit time for light to cross the detector is 93 ns), and some reflections. The 20 ns pulse has the capability to study backgrounds from the centre of the detector.

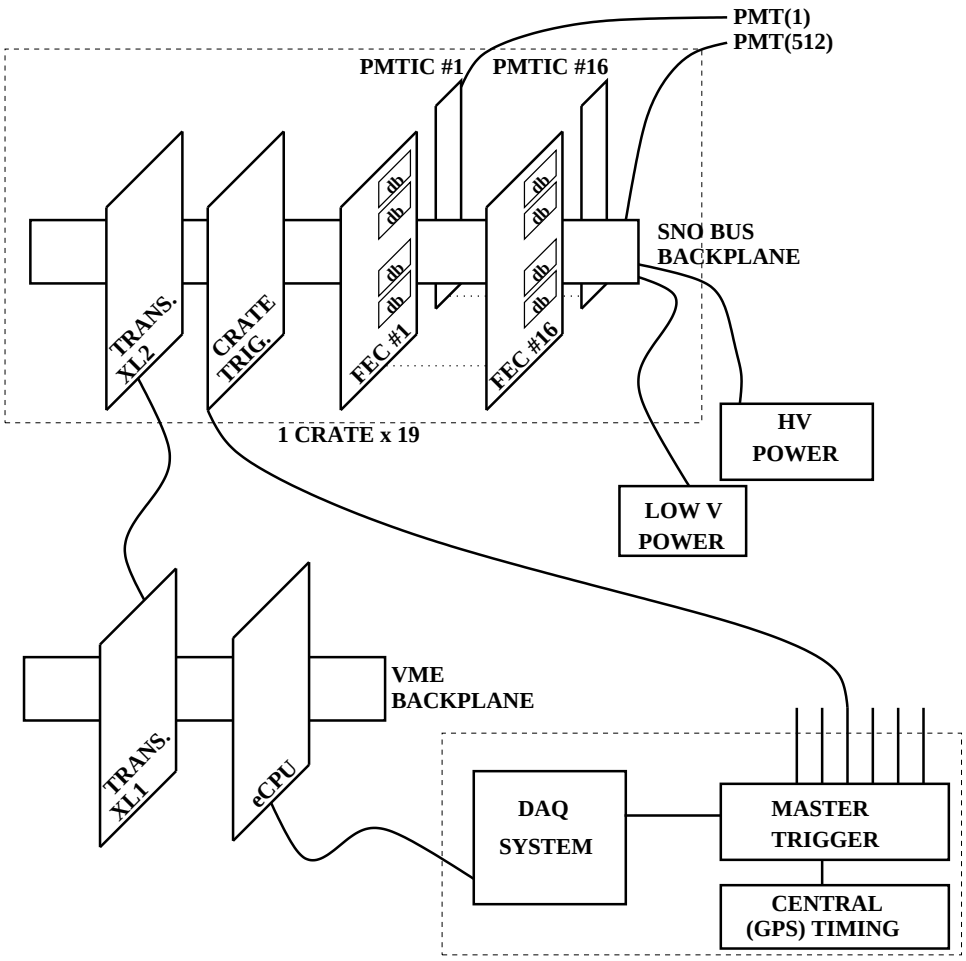

Figure 2.6: Overview of the custom built front end electronics. Figure taken from [26].

Once triggered, the PMT current is split (1:16) into low gain:high gain, and is passed to an integrator for long (400 ns) and short (70 ns) charge integrations. The charge information, essentially a shaped pulse similar to the PMT output, is useful for detector diagnostics but it is the 100 ns discrete signal that is the primary trigger in SNO. Each trigger is summed for the 32 input channels and is digitally stored in 4 MB of on-board memory, large enough to buffer a supernova burst. The values are reset after a $\sim$ 400 ns time interval if no global trigger is released. A backplane for each crate distributes the power and sums the analogue signal. This information is passed to the crate trigger card which determines whether the signal from all the crates exceeds the global trigger. A global trigger is defined as more than 16 PMTs firing in a coincidence window of 100 ns. The inter-event time is registered by a 50 MHz high precision quartz oscillator and is compared to a 10 MHz clock, used to gauge the start and stop times of runs.

2.6 Calibrations

2.6.1 Electronics Calibrations

It is vital that the charge and time measurements across all the PMTS are synchronised. The electronics calibration (ECA) uses electrical pulses to the channels to calibrate the conversion of digitised information about the charge and timing into empirical values.

- The charge pedestal is calculated by triggering the discriminator with no input and measuring the mean analogue-to-digital conversion values for each channel to determine the individual zero offset associated with each channel.

- The time pedestal is calibrated by determination of the delay between the last discriminator firing and receipt of the global trigger.

- The pulsed global trigger fires at a rate of 5 Hz and is used to calculate the average noise rate associated with the PMTs, determined to be approximately 500 Hz over the global trigger window. This is dependent on an accurate calculation of the number of working tubes for an event.

- Delaying the response from the time pedestal to the global trigger by varying widths profiles a time to amplitude conversion (TAC) slope. These calibrations are run twice a week and interpolated to minimise the amount of neutrino deadtime.

2.6.2 PMT Calibrations

The electronics calibrations for individual PMT timing cannot account for any delay introduced by the differing cable lengths from the PMTs to the electronics. Also a further necessary calibration is the discriminator walk correction; higher charges will trigger the discriminator earlier. The spread can be as large as 5 ns, which has repercussions for the subsequent reconstruction of an event and thus the associated energy, as explained in Chapter 3.

Both of these PMT calibrations are assessed with a "laserball" deployed within the detector over a range of positions by careful manipulation of the support-rope tensions, as shown in Figure 2.7. The 10 cm diameter diffuser ball releases very short pulses ($\sim$ 10 ns) of light, of externally controlled wavelengths in an isotropic fashion around the detector.

Comparing the light yields integrated over all source positions builds a profile of light behaviour in the detector for deducing optical constants and the relative efficiency of the PMTs. The apparatus to produce the light that is transmitted down optical fibres to the laserball is housed in the clean-room area immediately above the detector. Five wavelengths in the range 337 to 650 nm can be produced there, by the combination of a 50 Mhz pulsed laser producing 0.6 ns width bursts of 337.1 nm wavelength light, and one of four dye cells.

2.6.3 Source Calibrations

A range of sources of known energy are deployed throughout the light and heavy water regions to mimic the expected physical interactions and calibrate the energy response of the detector. The neck and side ropes allow for reasonable scanning in all three planes within the D_2O although access is limited in the regions just below the neck and at the edges of the AV. No such mechanism is available within the H_2O and so calibration sources in th elight water are deployed down guide tubes which limits the coverage.

^{16}N Source

The primary source used for energy calibration is the ^{16}N source which β decays, the dominant branch emitting a monoenergetic 6.13 MeV γ ray. The 7.13 s half life demands quick manufacture of ^{16}N, via an (n,p) reaction on the oxygen in CO_2. This is held in a stainless steel container held in the D_2O, to absorb the electrons (whose energy extends up to 10 MeV). The strength of the source has been measured as producing more than 300 ^{16}N per second and yields a 6.13 MeV γ ray 66% of the time.

^{252}Cf Source

The majority of ^{252}Cf decays (96.9%) are via α emission but the remaining 3.1% of decays are spontaneous fission, releasing neutrons. The average neutron multiplicity for each fission is 3.768 ± 0.005, and the strength of the source has been measured as producing 17.12 ± 0.17 neutrons per second on 1st September 2000 [38]. The source is contained within a solid acrylic cylinder of diameter 2.5 cm to absorb the majority of background events from β decay of fission fragments. Additional γ ray contamination is reduced through implementation of a temporal cut to remove

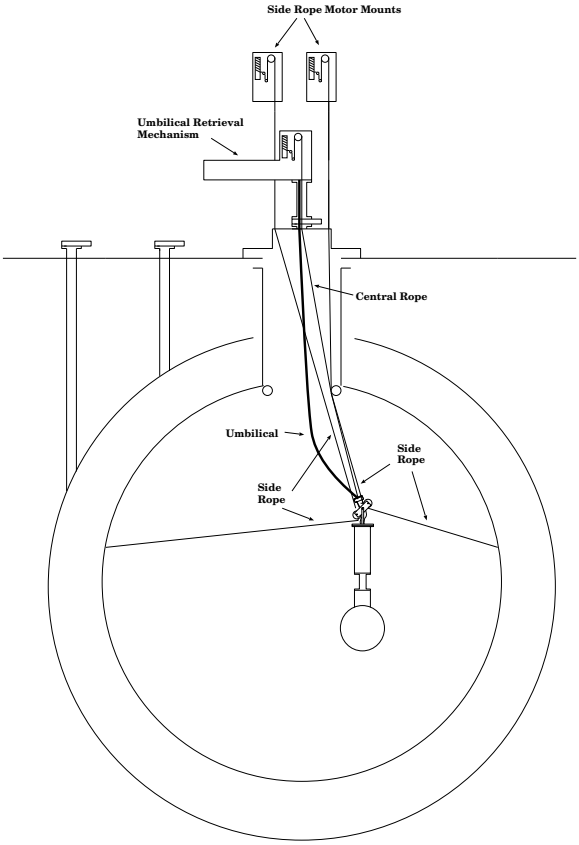

Figure 2.7: The neck of the acrylic vessel allows for deployment of calibration sources into the D_2O fiducial volume.

prompt events, providing an almost pure neutron source. In the pure D_2O phase there was a large enough distance between γ and neutron capture that a radial cut around the source was employed, but the neutron capture length is shortened in the salt phase and so the radial cut still allows significant levels of background.

^{8}Li Source

The neutrinos that SNO can detect are emitted when ^{8}B in the Sun decays to the first excited state of ^{8}Be. This is the analogue reaction ^{8}Li decays, and so it provides an ideal source to replicate the CC interaction (as the Sun produces electron-type only neutrinos). A deuterium-tritium generator (also used to make the ^{16}N source) produces 14 MeV neutrons that can capture on ^{11}B and induce an (n,α) reaction to give ^{8}Li. This is piped into a container in the D_2O where it β decays, releasing electrons whose energy extends up to 13 MeV. This decay is followed by two α particles of energy 1.7 MeV each, which can be detected by a PMT inside the source.

Tagging such events achieves a purer signal.

"Super-hot" Thorium Source

One of the most valuable sources in the second phase of running has been the super-hot ^{232}Th source to replicate neutron capture on ^{23}Na in the added salt. A source of strength $1.18(\pm 5\%)\times 10^{9}\,\gamma$s per hour was deployed for 20.25 ± 0.5 hours in September 2001. The probability of a 2.614 MeV γ to photodisintegrate deuterium is $2.19(\pm 5\%)\times 10^{-3}$ and the chance that one of these neutrons activates ^{23}Na is $1.37(\pm 3\%)\times 10^{-2}$, giving an activation probability of $3.00(\pm 6\%)\times 10^{-5}$. The β γ decay of ^{24}Na is similar to that of ^{208}Tl and so it can be used to check the Monte Carlo simulations of these decays, a primary source of background described in Chapter 5.

Radon Spike

A "spike" is a relatively large quantity of uncontained radioactivity that almost immediately overwhelms any other detectable events in either the light or heavy water, depending on its point of injection. ^{222}Rn is an intermediary in the ^{238}U chain. Its half life of 3.82 days is an ideal length for it to be used as a source to investigate modelling of the ^{214}Bi decays within the D_2O, whose importance is detailed in Chapter 5. A spike of strength 81 ± 4 Bq [39] was introduced into the detector in February 2003, implying a contamination of 6.50×10^{-12}g/g ^{238}U. The D_2O was circulated four days after source deployment for homogeneity across the detector.

Chapter 3

Data Quality

3.1 Data Processing

SNOMAN, the **SNO** **M**onte Carlo and **AN**alysis package, is a Fortran 77 based software tool, originally developed at Oxford and now continuously updated throughout the collaboration. Oxford maintains overall responsibility for the management of the code. It runs as a modular system to ease distribution and to simplify changes to the configuration. The units are controlled by the ZEBRA memory manager, part of the CERN library. SNOMAN allows the user to generate simulations of many types of events with outcomes specific to the geometry and actual status of the SNO detector at a particular time.

All Monte Carlo simulations used for final and published analyses (and within this thesis) were generated for the collaboration by an automated program within SNOMAN to ensure consistency in the models used and standardised parameter values. Signal Monte Carlo was generated at 200× the SSM rate for the ^{8}B neutrinos, and rates of 2 Hz for the ^{214}Bi and 0.17 Hz for the ^{208}Tl and ^{24}Na simulations. Standardised modules include the source calibration defined optical constants, the detector geometry and how it changes with respect to the distribution of working tubes. Standard radiation transport interactions are modelled externally in EGS4 (**e**lectron **g**amma **s**hower) and is applicable to a wide range of particle physics experiments. This module can be referenced in SNOMAN simulations by look up tables, after which any alterations are made, such as to account for Mott terms [31], or to include interactions on deuterium [40], and production of Čerenkov light in D_2O.

3.2 Event Reconstruction

3.2.1 Fitter

The location (vertex) of an interaction in the detecting media is obtained from the relative times that the Čerenkov light from a Compton scattered electron arrives at the PMTs. The vertex is reconstructed back as the point for which the timing residuals of all PMTs hit are as small as possible. The timing residual, corrected for the time taken for the Čerenkov-emitted photons to arrive at the PMTs, is described as:

$$T_{\text{residual}} = T_{\text{PMT}} - T_{\text{fit}} - \frac{|\vec{x}_{\text{fit}} - \vec{x}_{\text{PMT}}|}{< \text{c} >} \ , \tag{3.1}$$

where <c> is the average group velocity of light. Even for an event that has occurred at the centre of the detector the residuals will not all be zero because of the resolution of the PMTs and the electronics, and the scattering of the light along its path. The most likely vertex is determined through maxiumum likelihood, using probability density functions of the time at which each PMT fires constructed from laserball calibration runs and Monte Carlo simulations. The distribution is approximated after 15 ns, to avoid implementation of detailed scattering and reflection algorithms.

Likelihood is again employed to determine the most probable trajectory of an emittant electron after its interaction, given the angular distribution of the Čerenkov photons. This is compared to a model of the angular distribution of photons based on simulated (and thus of known direction and origin) distributions of light from 8 MeV electrons. Minimisation of the logarithm of $\mathcal{L}_{\text{direction}}$ determines the most likely direction of a single electron giving rise to the Čerenkov light, by taking the photonic angular distribution for the event direction convolved with the direction to each PMT over a prompt time window ± 10 ns either side of the time residual. For events involving multiple electrons (*e.g.* neutron capture on ^{35}Cl) the direction is an average of the direction of all the emitted electrons, given by all the hit PMTS. Only prompt photons are used to avoid complications from scattering and reflections. Determination of the event direction is particularly important for the ES interaction which has a strong directional dependence; an additional parameter for separation from the CC signal.

3.2.2 Energy

The number of PMTs hit in an event, $\boldsymbol{N_{\mathrm{hit}}}$, is proportional to the number of photons produced from Čerenkov light, as described in section 1.6, and so gives a direct handle on the energy of the electron. N_{hit} can be used as a raw variable to monitor the energy of an event but there are no corrections for noise, PMT failure, or drift (*e.g.* that due to the temporal degradation of the detector or change in energy response because of increased attenuation). However, accurate Monte Carlo simulations which replicate the state of the detector for each run will suffer the same attenuation of light from most of these effects. N_{hit} also has a spatial and directional dependence that decreases its resolution.

An energy scaling relationship that takes into account multiple hits of photons on single PMTs, cross-talk between electronics channels and second order energy loss processes of the electron, such as bremsstrahlung radiation and production of delta rays, demonstrates that the light yield is closely linearly proportional to the energy [41], down to the Čerenkov threshold of 0.26 MeV. Additional time dependent factors such as the energy drift and detector configuration do not significantly detract from the linearity. The energy response estimator, response providing the acronym **RSP**, uses a time of flight corrected measure of the number of tubes that fire within a prompt time window of ± 10 ns [38]. In such a restricted time window it can not account for any scattered or reflected light, but Figure 3.1 shows that to a good approximation most of the light from an event will occur in this window, for which greatly simplified optical corrections can be applied. Output from a PMT is only used if electronics calibration demonstrates good timing. RSP corrects for the noise rate by subtracting off an estimation from a 5 Hz pulsed electronics trigger of typically 0.1 hits per event, or about 10 keV. The fitter normalises all prompt light events through an estimation of the reconstructed position, thereby removing both the directional and spatial dependences that affects N_{hit}. Correction factors for the optics and temporal drift are also applied in the response efficiency term. The number of working tubes in an event uses the electronics calibration information and ignores channels with low occupancy rates.

$$N_{\mathrm{corrected}} = \frac{N_{\mathrm{prompt}} - N_{\mathrm{noise}}}{\epsilon_{\mathrm{response}}} \frac{\mathrm{PMT}_{\mathrm{total}}}{\mathrm{PMT}_{\mathrm{working}}} \, . \tag{3.2}$$

The most likely energy is then assigned to an event of *known* N_{hit} and *estimated* position, using ^{16}N calibration data. A drift correction is applied at the time of processing, to

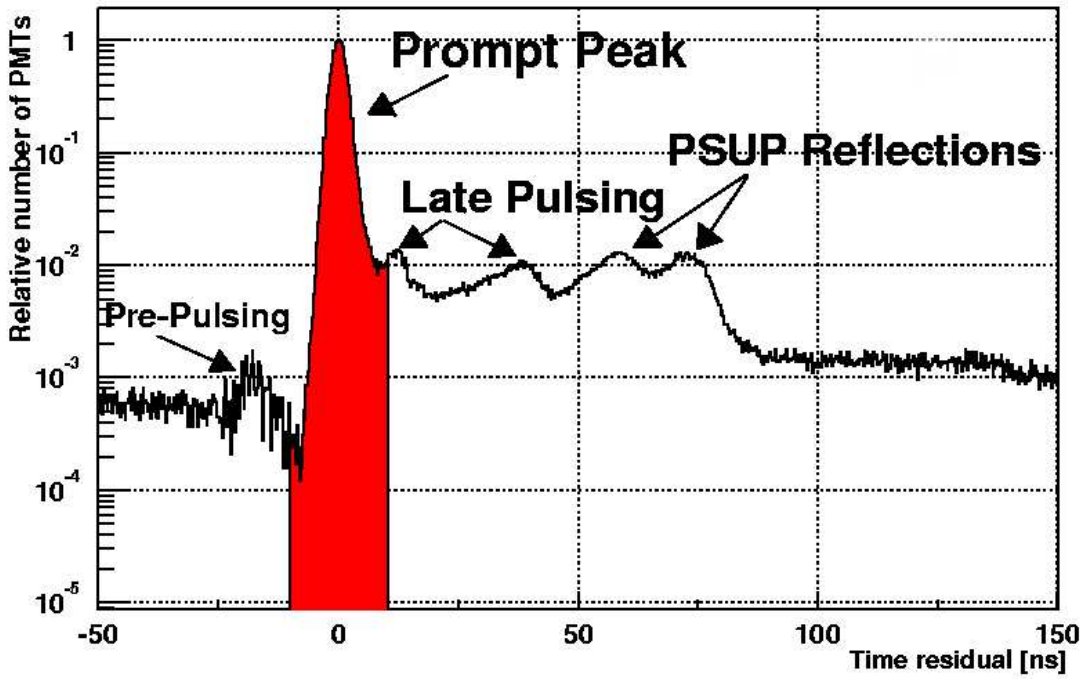

Figure 3.1: PMT timing distribution for an ^{16}N calibration source deployed at the centre of the detector [38]. The late pulsing is of unknown origin, but could possibly be caused by reflections within the PMT. The PSUP reflections occur for light that has travelled all the way to the edges of the support structure and undergone reflection back into the D_2O before being detected.

account for the changing D_2O attenuation lengths, probably due to an increasing level of manganese compounds and organics during the salt phase. There was also an increase in the attenuation close in time to when the salt was added due to a change in the angular response of the PMTs of unknown origin [42]. The drift is derived by observing the change in calibration of optical constants over the phase, yielding a correction factor of:

$$N^*_{\text{corrected}} = \frac{N_{\text{corrected}}}{1.51918 - 5.35013 \times \text{Julian date}} \; . \tag{3.3}$$

Julian date is commonly used for SNO analyses as a way of normalising all days to a nominal date: 0 hr (UT) on 31$^{\text{st}}$ December 1974.

To convert from the corrected number of hit PMTs to an actual energy, simulations of isotropic electrons are generated over a range of energies. A Gaussian distribution is fit to these to obtain the mean of the $N_{\text{corrected}}$ distribution for each energy in the form of a look up table. This is shown in Figure 3.2. A continuous energy distribution is obtained

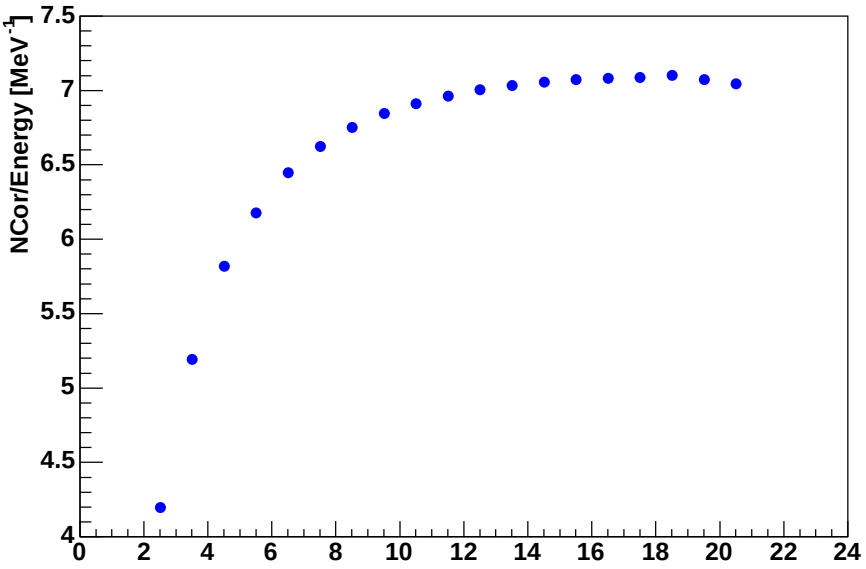

Figure 3.2: Figure kindly provided by R. Maclellan.

by interpolating between the discrete $N_{\text{corrected}}$ values. An energy mapping relationship, Equation 3.4, derived by comparing volume weighted RSP mean energies to electron energies [42], is applied to both data and Monte Carlo simulations after processing:

$$E_{\text{corrected}} = \frac{E_{\text{RSP}}}{0.9851 + \frac{0.09652}{E_{\text{RSP}}}} \ . \tag{3.4}$$

Finally, the kinetic energy is obtained by subtracting off 0.511 MeV.

3.3 Backgrounds

Given that the expected rate of ^{8}B solar neutrinos is approximately 10 per day and yet the detector runs at $\sim$ 20 Hz, the majority of signals in SNO are background and pulser events. Selection criteria (*cuts*) have been developed to remove background events, whether caused by instrumental effects or actual physical events that do not arise from ^{8}B neutrinos. These must be optimised to increase statistics whilst still ensuring that the data is of high quality. If the cuts are too stringent then a larger fraction of the data could be mis-identified as background (*sacrifice*); vice versa if the cuts are too relaxed to avoid losing data then some more background events might leak into the assumed signal region (*contamination*).

3.3.1 Instrumental Backgrounds

Breakdown of the PMTs working under high voltage, static discharge and electronic pickup and cross-talk from high charge are the most common occurrences of detector events that cause instrumental backgrounds. Exploiting the unique distributions in timing, geometry and charge that instrumental backgrounds exhibit allows for easy identification; see Figure 3.3.

A particular example of an instrumental background is a "flasher", which occur at a rate of $>\sim 50\,\mathrm{hour}^{-1}$ in SNO, possibly due to static discharge in the PMTs. A greater

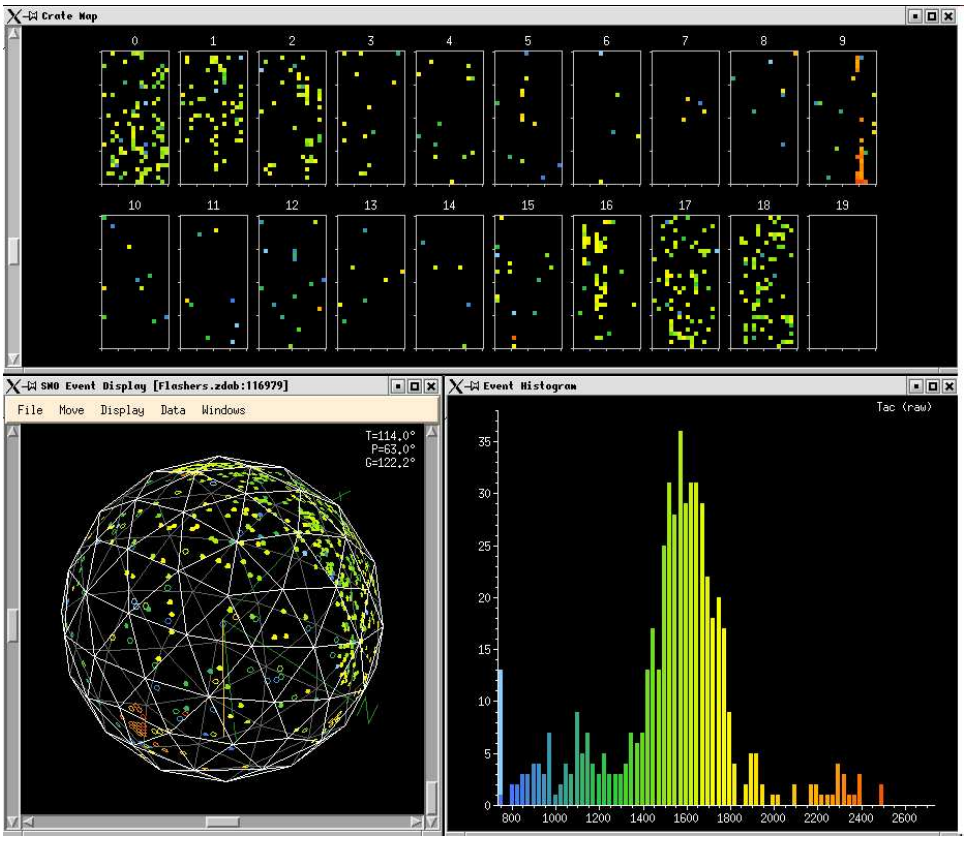

Figure 3.3: The timing, charge and geometry distributions for a flasher, a common form of electronics background in Čerenkov detectors. The timing distribution (bottom right) indicates an early burst of light, shown in orange. This can be colour-matched in the crate map (top) to the firing of two slots in the same card in crate 9, indicating a probable electronics failure. The elliptical distribution of hit PMTs across from a cluster of PMTs with very high charge is visible in the 3D detector display (bottom left).

understanding of the behaviour of these backgrounds led to a cut based on their geometry as described below. It is particularly useful in cases when the original burst of light from

the discharging PMT is not registered. As the light from the back of the PMT propagates across the detector, an ellipse of light is produced on the other side due to the shielding. This leaves a distinct signal easily separable from a neutrino event, which projects a ring (smeared through scattering) of Čerenkov light on a two dimensional plot of the array of PMTs, as shown in Figure 3.4. These backgrounds can also be removed with a cut that focuses on the arrival time of the late light.

As well as their unique geometry, flashers (and other electronic failures) exhibit large clusters of charge that are unphysical and allow separation from neutrino events. An analogue measurement board identifies the total charge, independent of individual channels and their associated failures. Once the charge pedestal has been normalised to zero using calibration data extrapolated to zero hits, the deviation of the analogue values from the mean can be used to give an indication of good events, since these typically deposit all their charge within a well defined, narrow time window. Events which lie more than $3.7\,\sigma$ from the mean are generally the result of instrumental failures, mainly due to flashers and pickup.

Pickup causes neighbouring tubes to fire. As well as having a distinct pattern in the electronic spacing of the channels, there is no integrated charge over a long enough time interval so analysis of the charge against time for an event can easily remove pickup events.

Other prominent sources of instrumental background may originate from cross-talk, when high charge from one PMT can induce a signal in the neighbouring electronics channel, and neck events, possibly caused by static discharge on the neck acrylic in the region of cover gas above the water, causing light signals at the bottom of the detector. A detailed account of the instrumental backgrounds and methods to remove them from the data set is found in [43].

Instrumental sacrifice is determined by analysis of the ^{16}N and ^{252}Cf calibration data, for electrons and neutrons respectively. Note that no comparison can be drawn between

Particle Type	Sacrifice (%)
Electrons	$0.37^{+0.15}_{-0.09}$
Neutrons	$0.40^{+0.15}_{-0.09}$

Table 3.1: The instrumental sacrifice levels are derived from looking at ^{16}N and ^{252}Cf data.

the data and Monte Carlo as instrumental problems have not been included in modelling scenarios. The values presented in Table 3.1 are independent of the fitting parameter (see Chapter 7) and purely represent the number of events that fail the cuts as a fraction of the total number of events. The statistical and systematic uncertainties have been summed in quadrature, the systematic uncertainties drawn from the spatial and temporal distributions (two scans of calibrations were performed at the beginning and end of data taking), as well as uncertainties associated with the stability of the electronics.

3.3.2 Physical Backgrounds

The physical backgrounds can be subdivided according to whether or not they generate Čerenkov light that is not distinguishable from neutrinos. If the light is distinguishable, the event will display different characteristics from a typical neutrino candidate event, which can be isolated through implementation of cuts associated with the timing and angular distribution of the light pattern. Cuts used to remove those backgrounds have been designed to accept signal rather than reject background, and can be applied to both data and Monte Carlo simulations. Any discrepancy between the data and the simulated events must be convolved into the sacrifice value. As they were developed after the instrumental cuts they also remove some previously undetected background, and certain events which mis-reconstruct inside the D_2O.

3.3.2.1 Distinguishable Backgrounds

In Time Ratio (ITR)

Photons from a Čerenkov cone are released essentially simultaneously, giving a well defined initial peak of light within a narrow time window, whereas those from other physical processes may have a much broader distribution of light (*e.g.* over time). The amount of light in the prompt window is compared to the overall amount of light. The number of hits that occur within $-2.5 \rightarrow 5$ ns of the time residual peak [44] is divided by the total number of hits, giving a ratio. The asymmetric range within the time residual distribution takes the additional scattering of late light into account. Neutrinos have an average in time ratio value of 0.75, compared with 0.35 for flashers. Excluding events with a value of ITR > 0.55 obtains the best balance of sacrifice and contamination of the data. The boundary value is the

same as it was in the D_2O phase as the addition of salt does not affect the timing distribution of an event.

Isotropy

The isotropy of an event can be determined by looking at the mean of the angle between any hit pair of PMTs, shown in Figure 3.4 as θ_{ij}. The Čerenkov rings are not generally as clearly seen because of multiple scattering of the electron which means that ring fitting algorithms can not be used. However, the average angle between all hit PMTs is a powerful indicator of the type of event. The average angle for a single ring event from a monoenergetic electron is much smaller than the average angle over two or three rings caused by multiple electrons from several γ rays. In pure D_2O a neutrino event produced a cone of light with a well defined θ_{ij} of ~ 1.1, corresponding to a Čerenkov angle of 42°; since multiple γ events were rare the isotropy could be defined purely by θ_{ij}. Lower bounds ($\theta_{ij} > 0.75$) removed badly reconstructed events and higher bounds ($\theta_{ij} < 1.45$) removed almost fully isotropic events that reconstruct back to the AV. Although these remain of unknown origin it is thought they could be due to stress relief at the bonding points of the acrylic plates. These events limit the width of the isotropy cut (and the fiducial volume) that may be used for a clean analysis.

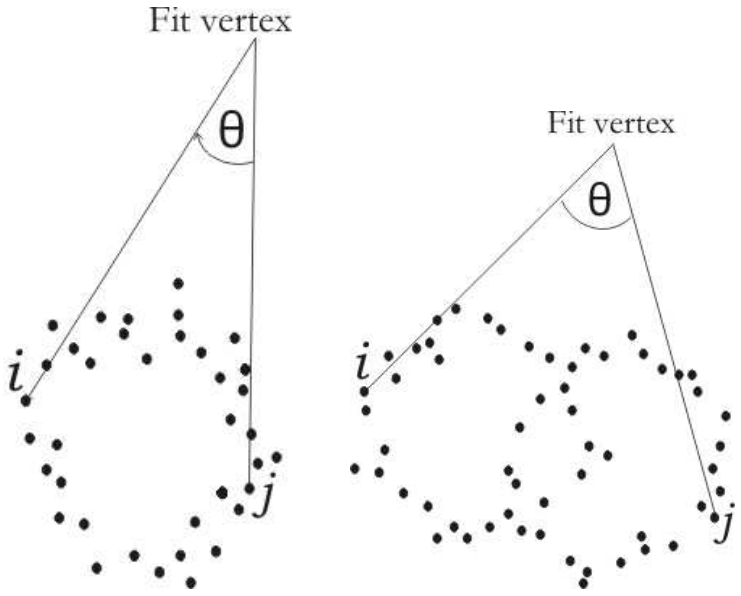

Figure 3.4: Isotropy distributions for one and two ring events

The addition of salt allows for increased neutron capture on ^{35}Cl, releasing a cascade of γ rays. Each of these γ rays, travelling in different directions, will induce a Čerenkov cone, resulting in a pattern resembling a single enlarged and blurred cone as those from all γ ray scattered electrons overlap, as shown in Figure 3.4. The average angle between all the hit PMTs is therefore broader for neutrons in salt; spanning from $0.8 < \theta_{ij} < 1.6$. Note that the isotropy cut in the D_2O phase would have had sacrifice levels of the order of 8% in the salt phase, thereby significantly impacting on the statistics. As in the D_2O phase, the level of scattering inhibits ring fitting algorithms, but the marked difference in cone size is a clear advantage for signal separation which lead to development of a new isotropy parameter. The Legendre polynomials of the average *cosine* of θ_{ij} were expanded to exploit the isotropy of an event for parameterised separation, the optimal separation [31] for events being a combination of terms:

$$\beta_1 + 4\beta_4 = \beta_{14}. \tag{3.5}$$

Since $\beta_1 = \cos(\theta_{ij})$, the isotropy of an event parameterised using the Legendre polynomials is approximately reversed from the average angle; multiple electron events (*e.g.* neutrons) have *lower* values of β_{14} than single electron events. The boundaries for β_{14} were determined, by balancing the sacrifice and contamination levels of electrons and neutrons, as $-0.12 < \beta_{14} < 0.95$. This yielded overall sacrifice measurements as shown in table 3.2.

Signal	Sacrifice (%)
NC	$0.68^{+0.16}_{-0.11}$
CC	$0.57^{+0.16}_{-0.11}$
ES	$0.86^{+0.21}_{-0.17}$

Table 3.2: The combined instrumental, isotropic and timing sacrifice levels for the three types of neutrino signals are all below 1%, as they were in the D_2O phase.

3.3.2.2 Non-distinguishable Čerenkov Backgrounds

Radioactive Decays

The majority of the Čerenkov backgrounds are those caused by radioactive decays from the ^{232}Th and ^{238}U chains, whose identification forms the basis of this thesis.

They are covered in more details in Chapter 5 and 6 . The addition of salt provided a new background through possible activation of ^{24}Na, producing neutrons to mimic the NC reaction. This is also discussed in more detail in Chapter 5.

Muons and Muon Followers

Despite the depth of SNO, muons from cosmic ray interactions in the atmosphere

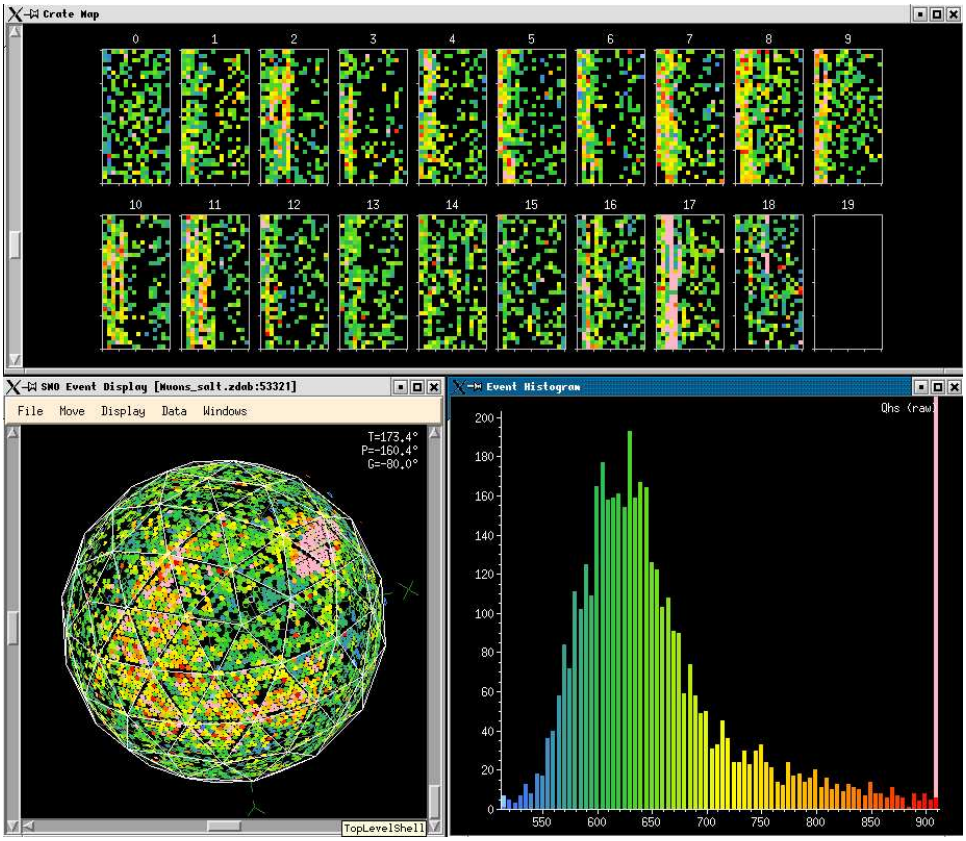

Figure 3.5: The path of the muon as it passes through a slice of the detector is visible as the two isolated regions of very high charge. A muon follower would typically illuminate all the PMTs in the event display immediately afterwards.

(see Equation 1.20) pass through the PSUP region of the detector at a rate of $\sim 3\,\mathrm{hr}^{-1}$. The muons may produce neutrons through spallation, mostly of deuteron but also, to a lesser extent, of ^{16}O. Muons can be identified by two regions (entrance and exit) of very high energies registered in both the inner and outer regions of the detector as the muon passes straight through. They can also be recognised if an event follows one which has triggered more than 150 PMTs (and so is most likely to be a muon). These events, induced neutrons, are called muon followers,

and must occur within a time window of 250 ms after the muon. This criterion is particularly useful in tagging contained muons, which only deposit high charge on entering the detector. Muons and muon followers can be eliminated from the data set through a timing cut that removes data up to 20 s after a muon. This provides one of the largest sources of deadtime but must necessarily be this large to account for the small, but still significant, number neutrons produced by ^{16}O spallation. The reaction produces ^{16}N whose relatively long half life of 7.13 s before emitting a γ ray capable of photodisintegration presents a problem: 90% of the neutrons following ^{16}O spallation occur up to 20 s after the muon has interacted in the detector. Given the relatively low rate of occurrence of such reactions, the 10% or so that fall outside this timing restriction were considered to be of negligible impact on the data set.

(α,n) Reactions

The acrylic and heavy water contain isotopes of H, C and O that may produce neutrons via (α,n) reactions if the incident α particle exceeds the energy threshold of 0.5871 MeV (necessary for capture on ^{17}O). There are 16 α particles in the ^{238}U and ^{232}Th chains that may induce the reactions, giving a very small calculated background of 0.016 ± 0.001 neutrons per day in the D_2O, which is subtracted from the total number of candidate neutrino events from NC interactions. A larger source of α particles are those from ^{222}Rn daughters on the surface of the acrylic, presumably from ^{2}10Pb deposited during construction, together with photodisintegration neutrons produced by ^{232}Th and ^{238}U in the AV or in the H_2O. As neutrons produced this way reconstruct back to the AV their unique radial profile means they may be fitted out in parallel with the neutrino signal.

Additional CC Interactions

A correction to the CC flux of 1.0078 [45] is necessary to account for the similar interactions that ^{8}B neutrinos have with ^{17,18}O, and in the salt phase the additional ^{23}Na and ^{35}Cl isotopes.

Fission

The branching ratio for the spontaneous fission of ^{238}U has been calculated as 5.45×10^{-7} [45], which would produce bursts of neutrons as background to the NC signal. These should however be tagged by several of the cuts that remove instrumental

backgrounds. Visibility of the prompt γ rays before the neutron burst is detected provides an additional tag to veto these events.

3.4 The Final Salt Data Set

The salt data set [39] used in this thesis covers the period 26$^{\text{th}}$ July 2001 to 28$^{\text{th}}$ August 2003, unless otherwise stated. Run selection procedures, including Chauvenet's criterion (discussed later), selected 1212 runs of actual livetime 391.432 days. This excludes the deadtime (mostly due to the 20 s muon follower cut), equivalent to 7.159 days [46]. A preliminary salt data set that formed the basis of the first paper of the salt phase [47], covered 254 days of livetime.

3.4.1 Run Selection

Needless to say, not all data can be considered worthy of analysis. A lot of effort is focused on attaining the best possible data, through careful detector monitoring and development of unbiased selection criteria. The first point of rejection is if the detector is in calibration mode or undergoing maintenance, including human activity in the region directly above the detector where the electronics racks are stored. Note that unless specific problems are documented by the operator the detector continues to take data during mine blasting and the majority of assays, the exception being the sample line assays which produce large quantities of light. The detector should be in good working order, that is to say that all PMTs are working between the nominal voltages, the compensation coils are functioning, and the laboratory is at a temperature and humidity suitable for smooth running of the electronics. The minimum length for a run to be selected is 30 mins; any shorter implies there were problems either side of the run which could have affected data quality.[1] Runs with jumpy rates were accepted but those whose average rate exceeds 60 Hz (the overall average rate is about 20 Hz), or whose rate exceeds this limit for more than 20% of the run, were rejected. Above 60 Hz the sacrifice is noticeably affected [48]. Also rejected were those runs where the main trigger threshold varied by more than 25% from the nominal value. There are second stage criteria that must be satisfied after the data has

[1] Conversely the maximum length for a run is 8 hours so that in case a problem has not been identified there is an upper limit to the amount of data lost.

been collated into an analysable form, such as rejection if data cleaning cuts removing burst events reduced the run time by more than 20%.

3.4.2 "Sims' Spike"

A preliminary study of the data to monitor the low energy backgrounds indicated that ^{238}U contamination overwhelmed any contribution from ^{232}Th, in contrast to what was expected from the previous experience of the D_2O phase results. Looking at the data on

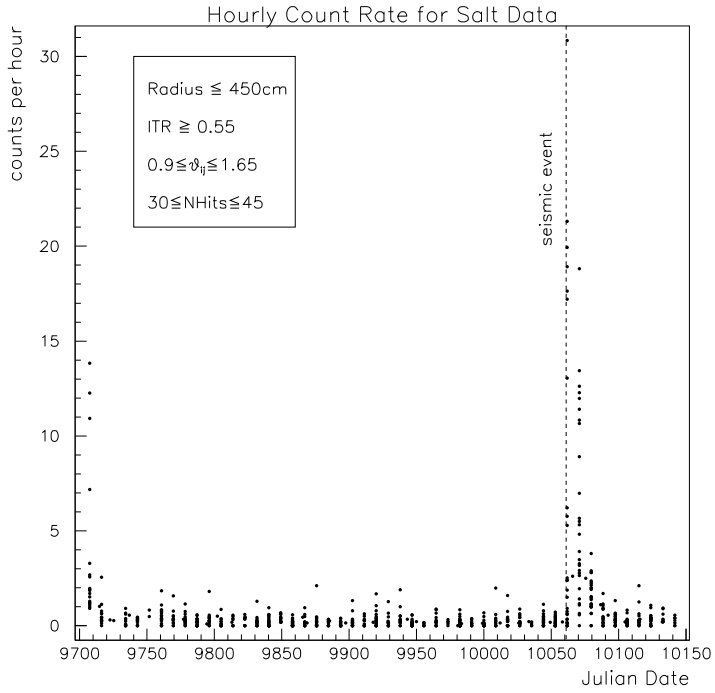

Figure 3.6: The data exhibits a large increase in count rate after Julian day 10060, equivalent to 18thJuly 2002, which coincided with a significant seismic event. There is also a much smaller increase in the event rate at the beginning of data taking, which was seen to occur immediately after deployment of a ^{252}Cf source for neutron calibrations, thus indicating residual neutrons from salt activation.

a run-by-run basis showed that a sequential group of runs was responsible for a 200-fold increase in the hourly count rate on 18th July 2002, shown in Figure 3.6, at least an order of magnitude higher than any high background rates in the D_2O phase. There is also a slight increase in the event rate at the beginning of data taking. The PMT isotropy distribution of these runs, shown in Figure 3.7, almost matches that of ^{214}Bi and one can

immediately tell how different the distribution is from the rest of the early salt data. The number of events from these runs, corresponding to 18 days of livetime, is comparable to the total number of events in the initial salt data set, spanning 254 live days. The

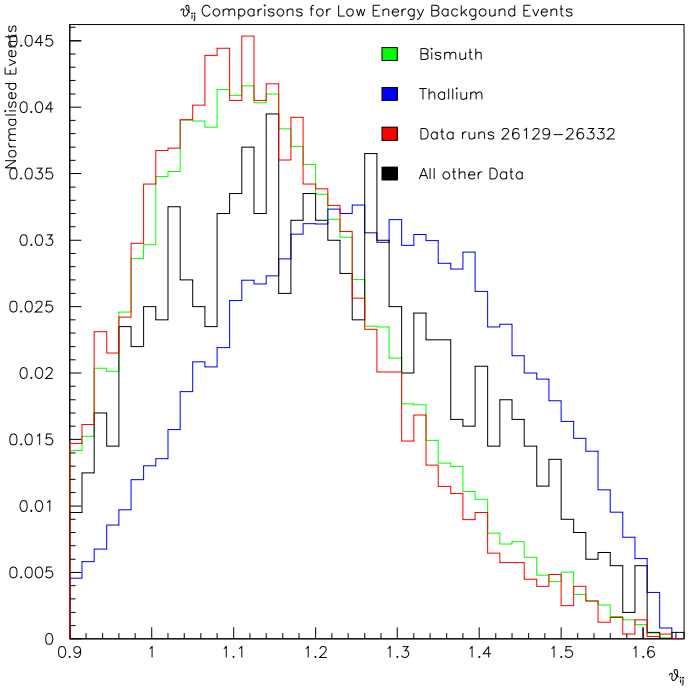

Figure 3.7: A comparison between the isotropy distributions for the period of very high rate and a preliminary data set of 254 live days, indicated that events in the high count rate period resembled ^{214}Bi events.

similarity in the PMT isotropy distribution to ^{214}Bi suggests possible ^{222}Rn ingress into the detector. This would be confirmed by the (usually) weekly ^{222}Rn assays as shown in Figure 3.8, for dates that correspond to Figure 3.6. Indeed for the smaller peak in event rate occurring 31$^{\text{th}}$ July 2001 (runs 20739 to 20744), ^{222}Rn assays indicated ^{238}U levels an order of magnitude higher than average; however given these runs followed ^{252}Cf source deployment there was a viable explanation for the increase; see section 5.4.

Seismic Event

A large seismic event registering 3.6 [49] on the Richter scale on 18$^{\text{th}}$ July prevented the assay scheduled for the same day. Coupled with the summer shutdown of the mine which terminated the assay programme until 10$^{\text{th}}$ September, there was

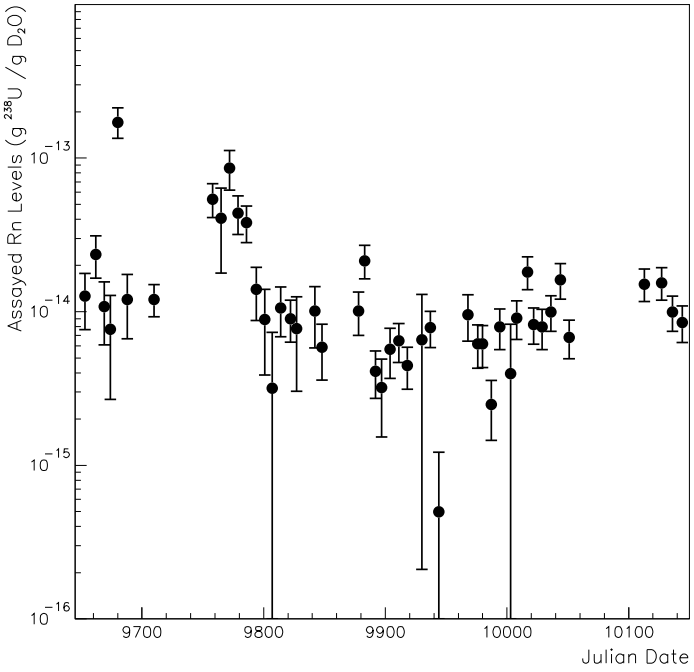

Figure 3.8: Results of Rn assays in the salt phase. There is an indication of above average ^{238}U contamination at the beginning of the data set, matching a time period after source deployment. No assays were taken during the months of the summer shutdown.

no cross-check available for the selection of runs which seemed to show such high ^{222}Rn levels. The seismic event was investigated as a possible cause of contamination, whether through the ingression of ^{222}Rn, or by having caused a problem with the electronics. The rate of flashers, known to increase with mine activity, was particularly high after the event occurred. It could be felt clearly in the SNO surface buildings, more than 2 km away from the detector. All the electronic channels showed substantial increase in trigger rate even up to 20 minutes afterwards, and over 1 hr later eight channels were still exhibiting exceptionally high trigger rates. If the increase in event rate were due to detector failure one would expect the rates to be much lower when measured using RSP, since it uses only the prompt light. The event rates are the same in N_{hit} and RSP for the initial (and smaller) ^{222}Rn spike, visible in Table 3.3, but Table 3.4 shows discrepancies between the rates for the runs immediately following the seismic burst. The rates, whilst still high, only converge

Run	$N_{\rm hit}$ Hourly Rate	RSP Hourly Rate
20739	14.13 ± 2.06	16.84 ± 2.25
20741	12.49 ± 1.67	16.07 ± 1.89
20742	11.14 ± 2.38	14.18 ± 2.68
20744	7.30 ± 0.84	9.44 ± 0.96

Table 3.3: Agreement in $N_{\rm hit}$ and RSP rates for the early ^{222}Rn spike on 31$^{\rm st}$ July 2001, following ^{252}Cf source deployment.

for the two energy estimators after run 26227. However the decrease is only by a factor of two and is thus still much higher than the average rate of 0.5 counts per hour, as derived from analysis of the quiet data periods. Hence the seismic event can not entirely explain the increase in event rate. The diagnostics trigger measuring

Run	$N_{\rm hit}$ Hourly Rate	RSP Hourly Rate
26147	96.40 ± 9.31	55.86 ± 7.09
26149	80.42 ± 3.58	51.28 ± 2.86
26153	98.60 ± 3.08	52.08 ± 2.24
26155	37.23 ± 1.36	47.26 ± 1.53
26158	27.45 ± 1.09	36.86 ± 1.26
26159	22.10 ± 4.03	33.14 ± 4.94
26160	23.59 ± 1.18	31.14 ± 1.36

Table 3.4: Lack of agreement in $N_{\rm hit}$ and RSP rates in runs immediately after the seismic event

electronics induced noise showed a four fold increase [50] in the $N_{\rm hit}$ average for runs 26149 to 26155. Since RSP corrects for noise according to an *average* rate, not all of the noise indicated by this trigger would have been removed. The seismic event certainly affected the event rate but whether it could have let ^{222}Rn in is unclear. A possible explanation could be disturbance of the cover gas, allowing in laboratory air with a high ^{222}Rn content. It was thought that perhaps ^{222}Rn was entering the D_2O through the chimney but analysis showed the count rate was not unusually high in the neck region. This was determined by comparing the background rates in the upper and lower half of the detector, and also by applying a $\vec{u} \cdot \vec{r}$ cut to the data, which can be used to preferentially select events entering into the D_2O. Standard events will have an equal chance that their direction of travel points into the

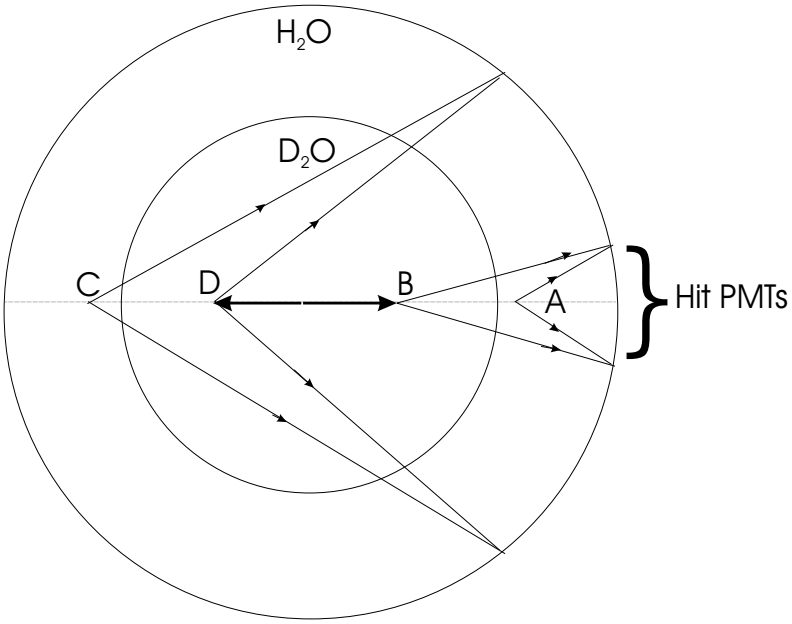

Figure 3.9: The event A in the H_2O may be misreconstructed back to B in the D_2O because the forward cone of light has poor timing resolution to the PMTs. The cone of light for an event C may be forward reconstructed to D but the event has better timing resolution given the larger distance travelled to the PMTs, so misreconstruction is less likely. Given the direction of travel of the event with respect to the centre of the detector, A $\rightarrow$ B will have a positive value of $\vec{u} \cdot \vec{r}$ and event C $\rightarrow$ D a negative value. Note that the width of the cone of light from event A is very small and most of these events will fail the lower bound of the isotropy parameter.

centre of the vessel, or towards the edges of the vessel. Figure 3.9. A convolution of the direction of the event with the radius to give a directional parameter $\vec{u} \cdot \vec{r}$, can discriminate somewhat between both background events that have been misreconstructed into the D_2O and events whose direction of travel points towards the centre of the vessel, (for which $\vec{u} \cdot \vec{r} > 0$) and events which originate from the D_2O and should be uniformly distributed across the directional parameter's spectrum: $-1 < \vec{u} \cdot \vec{r} < 1$. No significant bias was seen, indicating few background events within the sample had misreconstructed inside the D_2O or that a large proportion of the events were ^{222}Rn ingress from the neck.

Pump Failure

During D_2O circulation on 17^{th} July 2001, the loss of fibre signals lead to several power outages throughout the day, starting at 10.30 am. These caused the degassing

Pfeiffer pump (see Figure 2.3) to stop at about 2 pm and prematurely ended the circulation by tripping the water systems at 5 pm. This leaves a period of $\sim$ 3 hours in which laboratory air could have entered the D_2O circulation systems via the degasser, effectively turned into a *regasser*. On inspection it was noticed that there

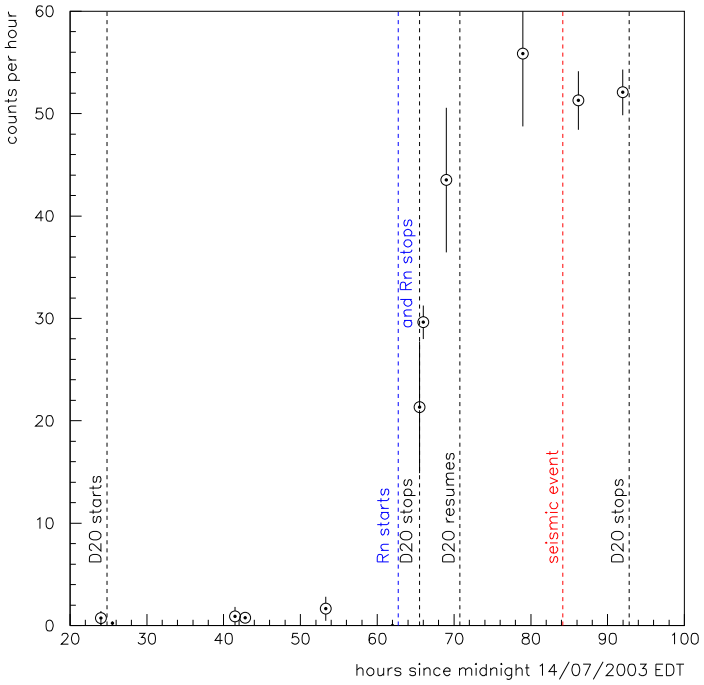

Figure 3.10: The increase in the count rate over time, matching the times of water circulation, pump failure and seismic events.

was no interlock between the Pfeiffer pump and the degasser isolation valves as previously thought, supporting the idea of ^{222}Rn ingress. Isolation valves have since been installed to prevent further leaks. Circulation recommenced 5 hours after the water system shutdown. Figure 3.10 clearly shows how the event rate increases after the pump failure and how D_2O circulation further increases the count rate through mixing. Confirmation of ^{222}Rn ingression is shown in Figure 3.11, which fits the data to a ^{222}Rn decay curve starting after the pump was noticed to be off, and at which point no more ^{222}Rn was entering into the detector.

Data Loss

Figure 3.11 confirms that the seismic event did not cause any ^{222}Rn leaks, otherwise the ^{222}Rn would soon reach equilibrium and no exponential decay would be seen. The seismic burst caused a change in the energy scale. The agreement is much better when the decay is fit to both the pump failure and the seismic burst. The ^{222}Rn ingress meant that the data could not be used for neutrino analysis. As the pump failure was coupled with the seismic event it could not even be used as a calibration source as there would be too much uncertainty regarding the energy scale and no way of separating the two effects to determine the absolute shift in the energy scale.

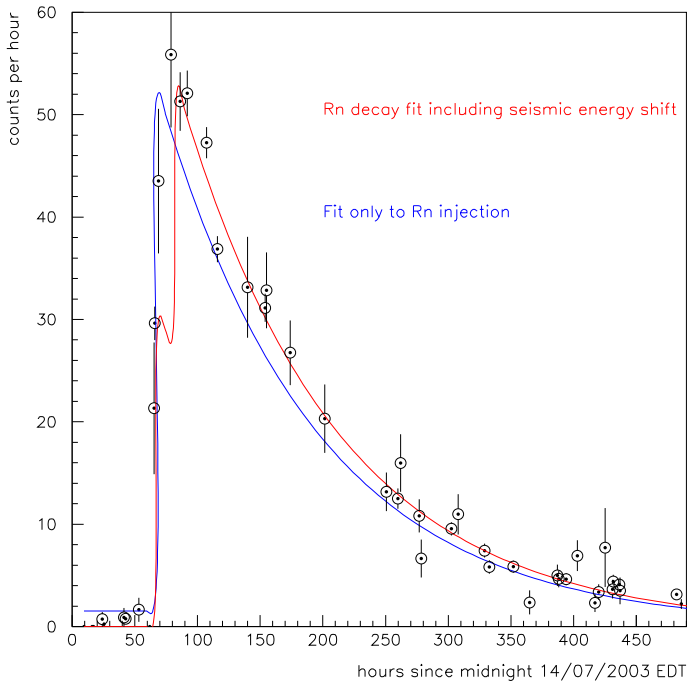

Figure 3.11: A fit of the high rate data to the time when the Pfeiffer pump was off, and the resulting exponential fall-off. If the fit includes an arbitrary value to account for a shift in recognised energy at the time of the seismic event the data points match the fit extremely well.

3.4.3 Chauvenet's Criterion

The probability of obtaining a statistically unlikely measurement changes with the number of observations, N, is $1/(2N)$. The probability of an event actually having occurred is determined by comparison with the standard deviation of a nominal quiet period of data: the 671 runs of the original salt data set after the Sims' spike had been removed.[2] Chauvenet's criterion states that the event may be justifiably eliminated from the data set if the probability of its occurrence is lower than the probability of it being unlikely.

Following the observation of the low energy spike relatively early on in the salt data taking period, Chauvenet's criterion was convolved into the selection process as a way of rejecting data thought to be statistically unlikely. This prevents human bias when subjectively deciding whether a run contains too much background to be considered good quality data.

Once flagged, the run is rejected if the high rate could be explained with additional detector information, such as anomalies in water shift log checks or taking place temporally close to calibration source deployment. Three sections were removed with the application of this additional selection method: residuals from the Rn spike in the D_2O and from the separate one in the H_2O, and residuals from ^{232}Th source deployment in the neck and subsequent circulation of the D_2O. Nine runs, of livetime 0.22 days, were flagged by both Chauvenet's criterion and a method for determining excess neutrons from calibration source deployment (more than 5% of the expected number from the SSM integrated over the livetime of the run [51]) as they occurred immediately after a ^{252}Cf source. Flagged data runs were kept if no explanation for the high rate was determined, which applies to 56 runs [52] with a livetime 4.2% that of the full salt data set.

[2] this also includes four runs whose event rates were not available due to clock problems and so had to be removed from the data set

Chapter 4

Deuteron Breakup

4.1 Introduction

This brief chapter outlines the theoretical models that are used to determine the cross sections for deuteron breakup. This is possible via interaction with a neutrino (the NC reaction), or a γ ray whose energy exceeds the binding energy of the deuteron; a process called photodisintegration. Since the products of these reactions are identical, and there exist sources of above threshold γ rays in the detector, photodisintegration provides a significant form of background to the NC signal, important for the calculation of absolute flux values and subsequent determination of oscillation parameters. Thus there must be a firm understanding and modelling of cross sections in any simulations of the interactions applicable to SNO. The subject of this thesis is the determination of the low energy backgrounds which inhibit the NC reaction through photodisintegration. Testing of possible separation and extraction methods rely on using Monte Carlo simulations (see Chapter 6) so it is vital to make sure these simulations accurately represent the physical processes that are being modelled.

Existing predictions of the rates of photodisintegration within SNO use a phenomenological fit to cross sections derived from effective range theory, dominated by contributions from the E1 transition, but also very slightly affected by the M1 transition near threshold. However, there are both theoretical and experimental limitations on using ERT: the effect of mesonic exchange currents are considered to be negligible and the fit is particularly statistically limited near threshold because of the difficulty of conducting experiments in that region and thus the lack of data.

Over the last few years the importance of improving the accuracy of deuteron disin-

tegration calculations has become apparent. Calculation of the cross-section of the time reversed form of deuteron photodisintegration has been a focus of much attention as it is key in determining the baryonic density in the initial stages of big-bang nucleosynthesis (BBN) [53, 54]. A relatively new approach uses effective field theory (EFT) in the modelling of the nucleon-nucleon (NN) interactions. The application of EFT within nuclear physics allows greater understanding of how certain processes (those requiring an overlap of knowledge from the nuclear and particle regimes) rely on scales and interactions determined by quantum chromodynamics (QCD), and the fundamental forces and principles of the Standard Model. A combination of EFT in nuclear physics and Lattice QCD can for example, allow detailed calculations of complex hadronic systems.

Since the energy range of interest for BBN is the same as for SNO, and the cross sections are equivalent, these conceptual developments are relevant to the understanding of photon-induced backgrounds in the SNO detector. The neutrino deuteron breakup simulations incorporate EFT predictions, but they have not yet been included in the photodisintegration simulations that SNO uses to verify the background. The refinements are shown to be small enough that the modified cross section would not affect any predictions regarding the rate of photodisintegration in SNO.

4.2 Photodisintegration

The phenomena of photodisintegration, initially referred to as the nuclear photo-effect, was first formalised in 1935 by Bethe and Peierls [55], by considering only the electric dipole (E1) transition, the most probable form of electromagnetic interaction, in the long wavelength limit. This constraint limits its application to very low energy photons ($< 10\,\mathrm{MeV}$) which do not have sufficient energy to probe into the structure of the nuclear wavefunction. Within this regime the range of the NN force is small enough to be negligible.

The differential cross section for a photon of energy ω, resulting in an emergent nucleon of average mass M and centre-of-momentum wavelength k, is

$$\frac{d\sigma_{\mathrm{E1}}}{d\Omega} = 2\pi^2 e^2 \omega k \mathrm{M} |\mathbf{D}_{fi} \cdot \varepsilon|^2 \,, \tag{4.1}$$

where ε denotes the polarisation vector of the photon, Ω is the solid angle, e^2 is the fine structure constant and $\mathbf{D}_{fi}$ indicates the electric dipole transition matrix element between

the initial (bound) and final (free) state. The final state must be a free plane wave as transition to the ground state, is forbidden by the Pauli exclusion principle. The matrix element after volume integration reduces to

$$\mathbf{D}_{fi} = i\frac{\sqrt{\alpha}}{\pi}\frac{\mathbf{k}}{(\alpha^2+k^2)^2} \ , \tag{4.2}$$

$\mathbf{k}$ being the final state momentum vector, and α^2 a constant value: the product of the average nucleon mass and the binding energy of the deuteron ϵ, $\alpha^2 = M\epsilon$, also related to the wavelength by $\alpha^2 + k^2 = M\omega$. Equation 4.1 can then be rewritten, for a particular angle θ between the incident photon and the momentum of the initial nucleon, as

$$\frac{d\sigma_{\mathrm{E1}}}{d\Omega} = \frac{e^2}{\alpha^2}\frac{(\gamma-1)^{3/2}}{\gamma^3}\sin^2\theta \ , \tag{4.3}$$

in which γ is the dimensionless ratio ω/ϵ. The accuracy of Equation 4.3 is dependent on experimentally determined observables, whose uncertainties are far larger than that of the binding energy of the deuteron or the mass of the nucleon [40]. The resultant energy-dependent error on the cross section (from the E1 contribution only) is $\simeq 0.2\%$.

4.2.1 Effective Range Theory

The zero-range force approximation breaks down in the asymptotic limit where there is significant divergence from the behaviour of a finite size wavefunction. Expanding the photodisintegration theory to incorporate those effective range correction terms appropriate for low energy nucleon scattering, allowed amplitude normalisation for a wide range of data. These data spanned the period from 1950 to 1980 [56] and were collected using various experimental techniques. Complications associated with the variation in energy of the incident nucleons are avoided in this particular case, as the deuteron is in a bound state of determined energy. The correction factor to the radial function is therefore both straightforward to evaluate, and exact. Integrating isotropically over all radii, the total modified cross section for an neutron-proton triplet of effective range r_{t} is

$$\sigma_{\mathrm{E1}} = \frac{8\pi}{3}\frac{e^2}{\alpha^2}\frac{(\gamma-1)^{3/2}}{\gamma^3}\frac{1}{1-\alpha r_{\mathrm{t}}} \ . \tag{4.4}$$

The experiments all expressed results that diverged from such theoretical predictions as the threshold was approached; the binding energy of the deuteron. Such behaviour was first noticed by Fermi [57], who observed that slow neutron capture in paraffin was in direct

contradiction to theoretical predictions. The only capture relevant to such low energies is from the continuum S waves, a process uniquely allowed by magnetic dipole (M1) radiation. This magnetic contribution modifies the disintegration cross section, which at higher energies is dominated by the electric dipole transitions. The M1 contributions have also been modelled using effective range theory [58]:

$$\sigma_{\mathrm{M1}} = \frac{2\pi}{3}\frac{e^2}{\mathrm{M}^2}(\mu_p - \mu_n)^2 \frac{k\alpha}{k^2+\alpha^2} \times \frac{(1 - \alpha a_{\mathrm{s}} + 0.25 a_{\mathrm{s}}(r_{\mathrm{s}} + r_{\mathrm{t}})\alpha_2 - 0.25(r_{\mathrm{s}} - r_{\mathrm{t}}k^2)^2}{(1+k^2\alpha^2)(1-\alpha r_{\mathrm{t}})} , \tag{4.5}$$

where μ_{p}, μ_{n} are the proton and neutron magnetic moments respectively, and a_{s} and r_{s} are the singlet's scattering length and effective range of interaction respectively. This assumes a dominant transition to the ground state, and explicitly accounts for the difference in effective range for a singlet and a triplet state.

The cross section for disintegration of the deuteron is thus the sum of the contributions from the E1 and M1 transitions:

$$\sigma_{\mathrm{PD}} = \sigma_{\mathrm{E1}} + \sigma_{\mathrm{M1}} \ . \tag{4.6}$$

A weakness in applying ERT to determine the M1 contribution is that any mesonic exchange currents are ignored, which contribute to the magnetic moment operator of the overall state and thus affect the contribution to the cross section. Noyes [40] estimated these would be accounted for by applying a $9.5 \pm 1.2\%$ correction factor to Equation 4.5. This far exceeds the random error associated with the M1 contribution, mainly derived from the uncertainty on the singlet scattering length and the triplet effective range. The error is correlated to the energy of the incident photon; evaluation for a photon near the peak of the deuteron photodisintegration cross section yields an error of $\simeq 0.08\%$ [40].

4.2.2 Effective Field Theory

Effective Field Theory was instigated by Weinberg [59] who applied the same chiral expansions that are used for the treatment of mesons and individual nucleons to the NN potential. He subsequently determined observable phase shifts by inserting the derived potentials into the Schrödinger Equation. The NN interactions are explored through a

series of perturbations. The expansion parameter used is the ratio of the light (NN scattering length, deuteron binding momentum, and nucleon momentum) to the heavy (pion) mass scales, which allows a phenomenological deduction of the dominant coupling parameter [60]. The technique allows for the thorough and systematic incorporation of relevant gauge fields. For treatment of low energy systems (relevant for SNO), the pion (and thus further hadronic excitations) has a scattering range of such negligible impact that it is not treated as a dynamical particle. Hence the [much simpler] *pion-less* EFT is applied, necessarily divergent as the mass of the pion is approached, so that the only dynamical degrees of freedom are the nucleons and the external currents.

J. Chen and M. Savage [53] have made significant improvements to the understanding of deuteron photodisintegration by using EFT to calculate the M1 contribution up to next-to-leading order (NLO), and the E1 contribution up to next-to-next-to-next-to-leading order (N^3LO). The following equations are taken from [53]. The E1 transition (dominant for $E_\gamma \lesssim 4.3\,\mathrm{MeV}$[1]) can be exactly calculated up to N^3LO as it is reliant solely on NN phase shift data. It is thus expected to be in very good agreement with expressions derived from ERT. Refining the calculation to a higher order [54] is no longer exact as it requires more experimental input for parameterisation of locally contributing operators [53]. Thus the contribution from the electric dipole transition can be expressed via its amplitude as

$$|X_{\mathrm{E1}}|^2 = \frac{|\mathbf{P}|^2 \mathrm{M}^2 \alpha^4}{(\alpha^2 + |\mathbf{P}|^2)^4} \times \left[1 + \alpha r_\mathrm{t} + (\alpha r_\mathrm{t})^2 + (\alpha r_\mathrm{t})^3 + \frac{\mathrm{M}\gamma}{6\pi}\left(\frac{\gamma^2}{3} + |\mathbf{P}|^2\right)\left(C_2^{(^3P_0)} + 2C_2^{(^3P_1)} + \frac{20}{3}C_2^{(^3P_2)}\right)\right], \tag{4.7}$$

where M, r_t and α are as defined for ERT, and $\mathbf{P}$ is the centre-of-mass momentum of each nucleon. The coefficients C_2 for P-wave final state interactions, which are significant for E1 transitions at N^3LO, are derived from phase shift analysis.

The M1 transition is expected to show more pronounced deviation from ERT as it necessarily accounts for the mesonic exchange currents that are absent from ERT treatment. EFT includes additional terms from interactions of the S_0 and S_1 channels, and couplings between the four nucleon fields and the photon, and the M1 coefficients. At NLO it is reliant on inclusion of a four-nucleon-one-magnetic-photon [53] counterterm.

[1] for which the centre of mass for either incident nucleon would be 1 MeV

This can however be phenomenologically determined by fitting the derived cross sections to experimental data for cold neutron capture, since the cross section at low energies near the threshold is overwhelmingly dominated by M1 transitions. The M1 amplitude is given by

$$|X_{\rm M1}|^2 = \frac{\kappa_1^2\alpha^4(\frac{1}{a_{\rm s}}-\alpha)^2}{(\frac{1}{a_{\rm s}^2}+|\mathbf{P}|^2)(\alpha^2+|\mathbf{P}|^2)^2}\times \\ \left(1+\alpha r_{\rm t}-r_0\frac{(\frac{\alpha}{a_{\rm s}}+|\mathbf{P}|^2)|\mathbf{P}|^2}{(\frac{1}{a_{\rm s}}+|\mathbf{P}|^2)(\frac{1}{a_{\rm s}}-\alpha)}-\frac{L_{\rm np}{\rm M}(\alpha^2+|\mathbf{P}|^2)}{2\pi\kappa_1(\frac{1}{a_{\rm s}}-\alpha)}\right) , \tag{4.8}$$

where κ is the isovector nucleon magnetic moment. As before, $a_{\rm s}$ is the singlet scattering length. Hence the total cross section for $np\to d\gamma$ can be expressed as

$$\sigma(np\to\gamma d)=\frac{4\pi e^2(\alpha^2+|\mathbf{P}|^2)^3}{\alpha^3{\rm M}^4|\mathbf{P}|}\left(|X_{M1}|^2+|X_{E1}|^2\right) . \tag{4.9}$$

This is related to the inverse reaction of photodisintegration, *i.e.* that relevant to backgrounds in SNO, by

$$\sigma_{\rm PD}=\frac{2{\rm M}(E_\gamma-\epsilon)}{3E_\gamma^2}\sigma(np\to\gamma d) . \tag{4.10}$$

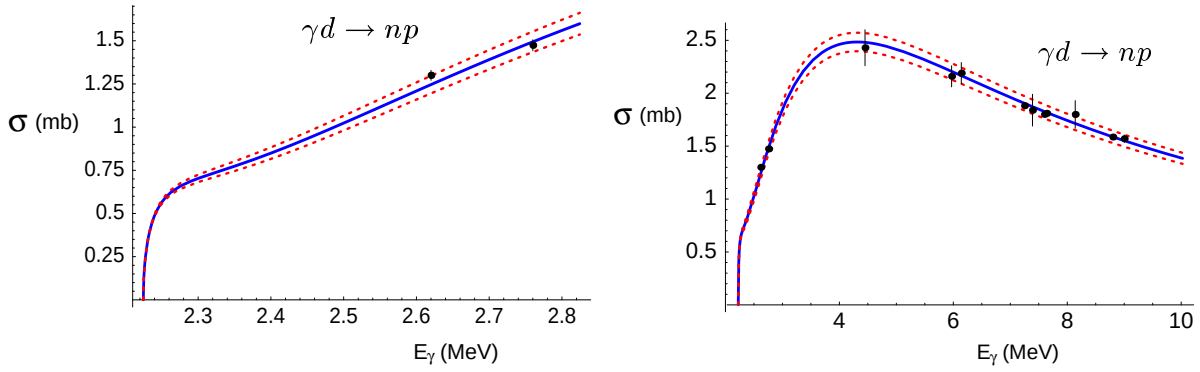

Figure 4.1: EFT derived cross sections in the energy region of interest to SNO, showing specifically the region of interest from the main sources of low energy backgrounds in the zoomed in section. Figure taken from [53].

The left hand plot of Figure 4.1 shows the deuteron photodisintegration cross sections derived using EFT for incident γ rays in the 1 MeV above threshold, specifically indicating two energies shown in Table 4.1. The cross sections for a 2.445 MeV γ ray from ^{214}Bi decay and a 2.614 MeV γ ray from ^{208}Tl can be read off as 0.8 mb and 1.25 mb. The

E_γ (MeV)	M1 (mb)	E1 (mb)	M1 + E1 (mb)	Data (mb)
2.62	0.380	0.866	1.25 ± 0.05	1.300 ± 0.029
2.76	0.327	1.167	1.50 ± 0.06	1.474 ± 0.032

Table 4.1: EFT-derived values of photodisintegration cross sections for two energies just above threshold, for comparison to experimentally determined values. The experimental values were taken from [56].

right hand plot shows the cross sections for γ rays up to 10 MeV, with the cross section peaking at $\simeq 2.5$ mb for γ rays in the region of 4 MeV. The red dotted line indicates the width of uncertainty associated with the theory, less than 4%. Excellent agreement with experiments is shown by comparison with the black data points taken from [56].

4.3 Comparison

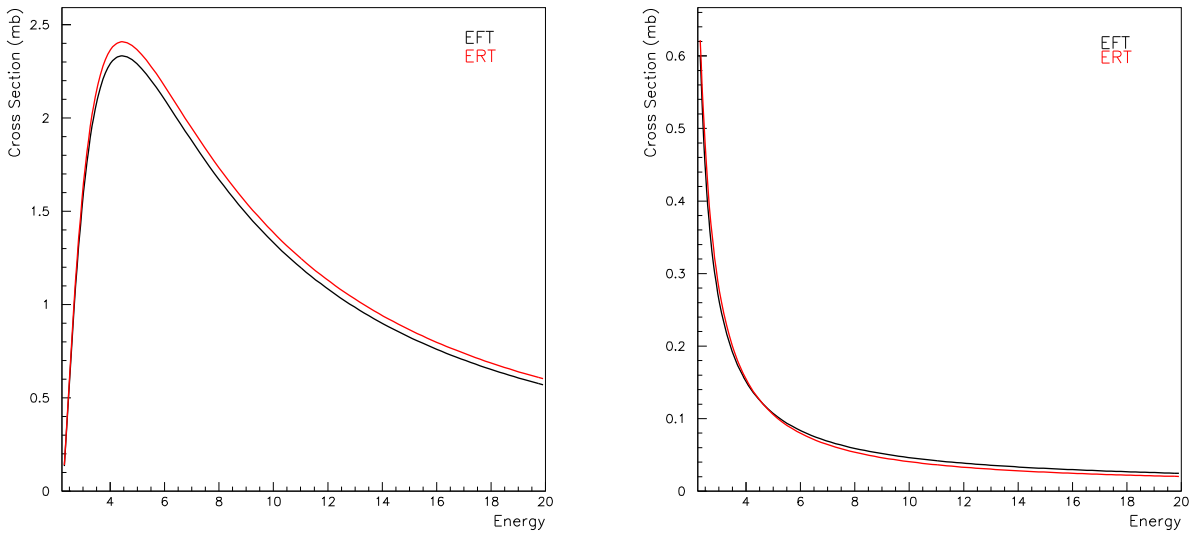

(a) E1 contribution

(b) M1 contribution

Figure 4.2: Comparison between the EFT and ERT derived deuteron photodisintegration cross sections.

This section compares the expected photodisintegration cross sections using effective range and effective field theories, for an energy range appropriate to SNO. Figure 4.2(a)

was obtained by creating functions using Equations 4.4and 4.7 , and Figure 4.2(b) was similarly obtained with functions created by Equations 4.5 and 4.8. When compared to Figure 4.1, taken from [53] and so using the same equations, there was found to be 1% difference in the calculated cross sections from the E1 transition (and thus total contribution). Contact with the authors indicated that they had independently calculated the cross sections and had obtained results that differed from each other by 1%. Since this was consistent with the overall error of 4%, one set of numbers was chosen for publication. Hence the results obtained within this chapter are in exact agreement with the results of the first author [61].

Since the M1 contribution is very small in comparison with the E1 contribution, Figures 4.2 and 4.3 seem to indicate that only a simple downward scaling factor of 0.963 ± 0.098 would be necessary to incorporate the EFT corrections into the total cross sections.

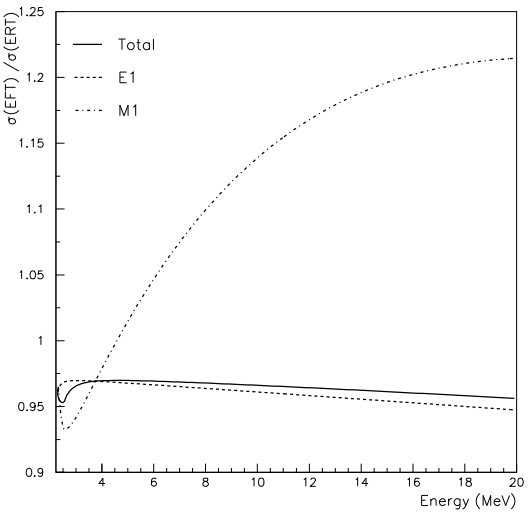

Figure 4.3: The ratios of the cross sections for deuteron photodisintegration.

However, the actual photodisintegration cross sections used in SNO are not the same as the theoretical values obtained from ERT. Above 20 MeV (and up to 440 MeV), use is made of a phenomenological fit by Rossi, which incorporated data collected from a variety of experimental methods to directly measure the deuteron photodisintegration cross section. It is statistically limited by selecting only experiments which employed monoenergetic gamma ray sources, with the dominant error being that associated with the

gamma ray flux. The fit is not very robust therefore between 10-20 MeV. An interpolation function designed to smoothly align the cross section across the energy spectrum, from the ERT approach above threshold, to the phenomenological fit, required a slight modification to the ERT derivation. This was determined by J. Lyon in [40], where more details can be found. He considered the functional form

$$\sigma_{\rm C} = \sigma_{\rm PD} \sum_{n=0}^{m} a_n x^n \ , \tag{4.11}$$

and imposed the boundary condition that, at the energy threshold (ϵ), the fitted function should converge with the theoretical cross section. With this in mind, the function that gave the smallest scale difference was

$$\sigma_{\rm C} = \sigma_{\rm PD}(a_0 + a_1 x + a_2 x^2)$$

$$\begin{aligned} a_0 &= +0.997141042790 \\ a_1 &= -0.005874520855 \\ a_2 &= +0.000031855970 \ . \end{aligned} \tag{4.12}$$

With the incorporation of this function, the cross section values are changed by only 0.3% to give a corrected cross section as shown in Figure 4.4. This now differs from EFT by

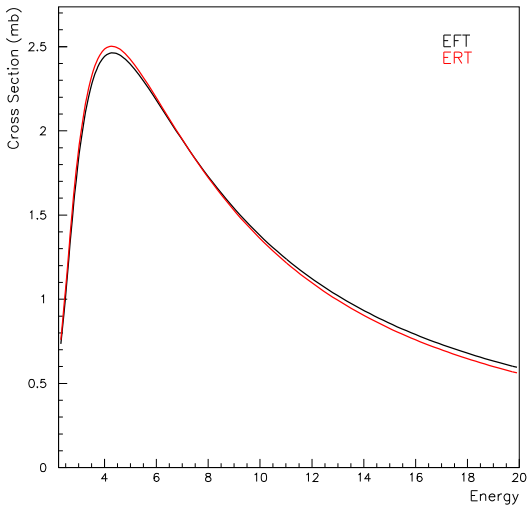

Figure 4.4: The ratios of modified cross sections for deuteron photodisintegration.

an average of 1.022 ± 0.101 Since the EFT error of 4% is double this correction factor

difference, there is little to be gained from incorporating EFT into the calculations of the photodisintegration of the deuteron. It was therefore decided to continue using the ERT derived calculations. However any future improvements in the error bounds on EFT calculations should be monitored to see if the error on the cross sections used in SNO could be significantly reduced.

Chapter 5

Low Energy Backgrounds

5.1 Introduction

Any γ ray whose energy exceeds 2.225 MeV, the binding energy of the deuteron, is able to split the nuclei into its constituent parts, a proton and a neutron; a process known as photodisintegration and extensively described in the previous chapter. The emitted neutron may be mistaken for one from a neutrino induced NC reaction. SNO must be able to determine the number of γ rays above this threshold in the D_2O, and hence predict the yield of neutrons from photodisintegration. This number of neutrons is then deducted from the number that provide the NC signal. Without this background subtraction, there would not be confidence in the total flux of neutrinos that SNO can uniquely measure with the NC reaction.

5.2 Background Radioactivity

Any element whose half-life exceeds the age of the Earth ($\sim 4.5 \times 10^9$ yr) has the potential to undergo a chain reaction through a series of α, β or γ decays until it reaches a stable element. The naturally occurring Thorium (^{232}Th) and Uranium (^{238}U) both have decay chains that produce γ rays capable of deuteron photodisintegration, shown in red in Figures 5.1 and 5.2. There are naturally occurring elements as well as ^{238}U and ^{232}Th with suitably long half-lives, such as the relatively rare isotopes ^{87}Rb, ^{144}Nd and ^{147}Sm, but their immediate decay to stable states, emitting α or β particles ($Q_{max} = 2.31$ MeV) well below detector threshold ($Q_{tot} > 3.5$ MeV or $E_\gamma > 2.2$ MeV), means they do not present a worry for SNO.

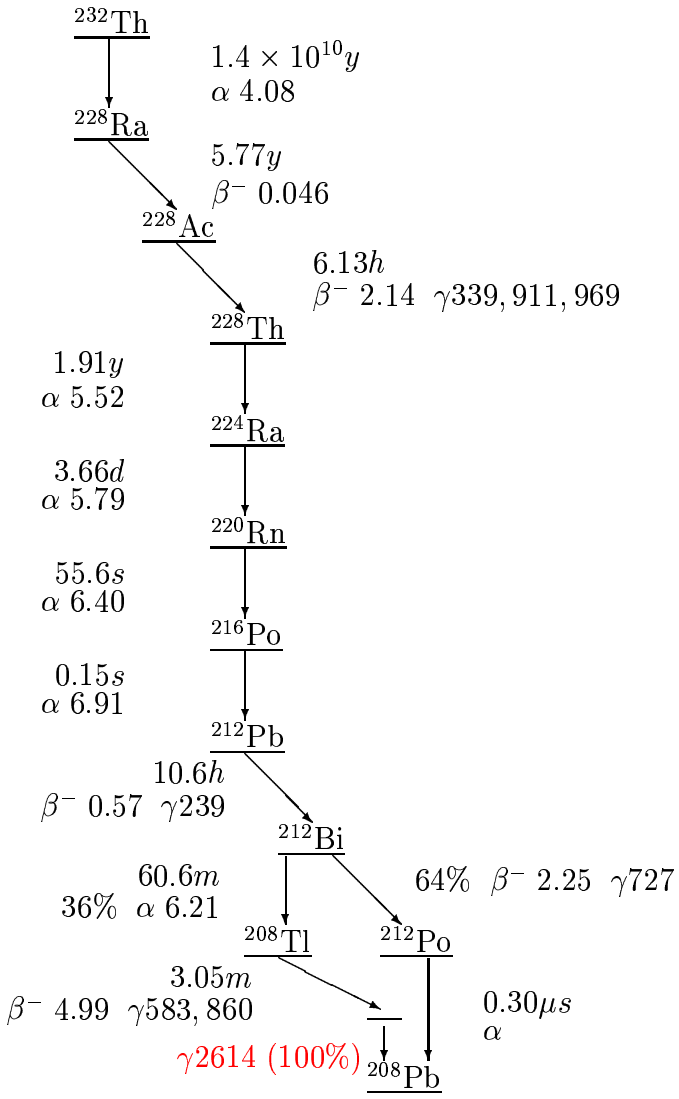

Figure 5.1: The ^{232}Th decay chain. All half-lives are shown, with the Q values of α and β decays in MeV, and γ rays in keV. Taken from [62].

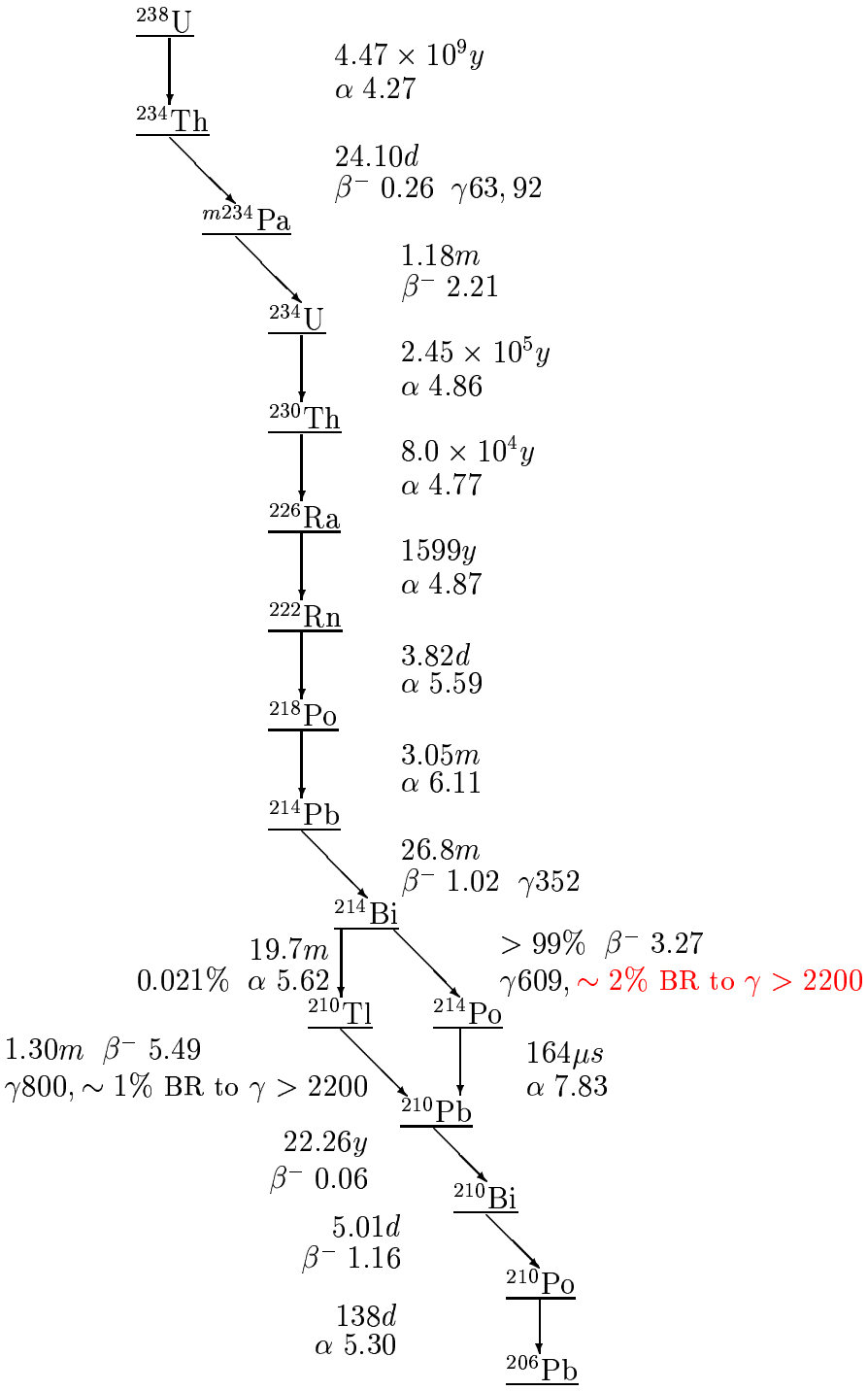

Figure 5.2: The ^{238}U decay chain. All half-lives are shown, with the Q values of α and β decays in MeV, and γ rays in keV. Taken from [62].

The radioactive isotope of Potassium, ^{40}K, has a branching ratio of 89% to a β particle of endpoint 1.31 MeV, the other branch giving a 1.50 MeV γ ray; although the γ ray is below the photodisintegration threshold there is a very small statistical probability of detecting the β particle above threshold. However, coupled with its extremely low natural abundance of 0.0117% there is negligible chance of detection.

No other naturally occurring radioactive chains contain γ rays capable of photodisintegration: thus the only radioactive elements that present sizeable background problems to SNO data are ^{232}Th and ^{238}U. The γ rays they emit occur near the bottom of both chains; in ^{232}Th in the decay of ^{208}Tl and in ^{238}U in the decay of ^{214}Bi, as shown in Figures 5.3 and 5.4. The nuclei are supported in the heavy water by any dissolved Radium, ^{224}Ra and ^{226}Ra, or dissolved Radon: ^{222}Rn is the principal concern as it has a half-life of 3.82 days and is naturally abundant in both the surrounding air and the rock.

Both radioactive chains are visible through Čerenkov light from the β γ decays of their daughters. Detection of this Čerenkov light allows an inference of the number of γ rays that may cause photodisintegration and produce background neutrons, as explained in Chapter 6. There is minimal contribution to the visible energy spectra from the backgrounds above a kinetic energy threshold of 5.5 MeV, as used for the solar neutrino analysis in salt phase.

5.3 Photodisintegration

A daily limit of one neutron per decay chain in the D_2O, roughly 10% of the NC signal, was initially considered a tolerable (and achievable) background level. This demands precise knowledge of the cross section for deuteron photodisintegration in the energy range $2.225 < E_\gamma < 10$ MeV, *i.e.* above the process threshold and inclusive of γ rays produced by the radioactive decays of ^{208}Tl and ^{214}Bi, as has been demonstrated in Chapter 4.

Both β and γ decays in the radioactive chains produce Čerenkov light, the γ rays through Compton scattering. The energy range of the scattered particle, given the energy of the initial γ ray is shown in Equation 5.1,

$$E_{\max} = \frac{E_\gamma}{1 + \frac{E_\gamma}{m_e c^2}(1 - \cos\theta)} \, . \tag{5.1}$$

The cross section in heavy water is at least two orders of magnitude more than for photodisintegration; however, if large enough numbers of γ rays are produced then the small

cross section for photodisintegration becomes significant. The maximum residual energy of a Compton scattered γ ray is at $\cos(\theta) = \pi$, so even after scattering there may still be some photons whose energy will exceed that necessary for photodisintegration.

Since the amount of Čerenkov light from ^{208}Tl that corresponds to one photodisintegration of deuterium is different than that from ^{214}Bi, their contribution to the NC background must be determined separately. This is achieved by measuring the amount of Čerenkov light from their decay products in the low energy region, between analysis and detector threshold. Confidence must be established that in this region the only signals are those generated by ^{208}Tl and ^{214}Bi decays from the main dominant radioactive chains.

5.3.1 Thorium

Figure 5.3 illustrates the ^{232}Th decay scheme. ^{208}Tl is part of the ^{232}Th decay chain with a branching ratio of 36%. As it decays to the radioactively stable ^{208}Pb it emits a 2.614 MeV γ ray (99.8%); the cross section for photodisintegration is 1.2 mb compared with the dominant Compton scattering cross section of 125 mb. The number of γ rays from the decay of ^{208}Tl needed to produce one neutron in SNO, as determined [63] from Monte Carlo simulations within SNOMAN, is 482.8 ± 6.9, equivalent to 1341 ± 19 ^{232}Th decays by scaling according to the branching ratio. Given the daily limit, the maximum contamination level in the D_2O is just 3.7×10^{-15} grammes ^{232}Th per gramme of D_2O, (g/g), which can determined using the radioactive decay law:

$$\frac{dN}{dT} = -\lambda N \ . \tag{5.2}$$

where λ is the decay constant (the reciprocal of the half life of either ^{238}U or ^{232}Th as shown in Figures 5.2 and 5.1) and N is the number of molecules, which can easily be converted into a mass using Avogadro's constant. Note that the typical natural abundance in light water for both radioactive elements is about 10^{-9} grammes per gramme of H_2O [63].

In the ^{232}Th chain, only the decay of ^{208}Tl has enough energy to trigger the detector. The almost negligible (5.5×10^{-6}%) branching ratio of ^{228}Ac α decays to ^{224}Fr, which in turn emits a 2.39 MeV γ ray, does not contribute to photodisintegration, nor does the 2.25 MeV β particle, released in two-thirds of ^{212}Bi decays within the ^{232}Th chain.

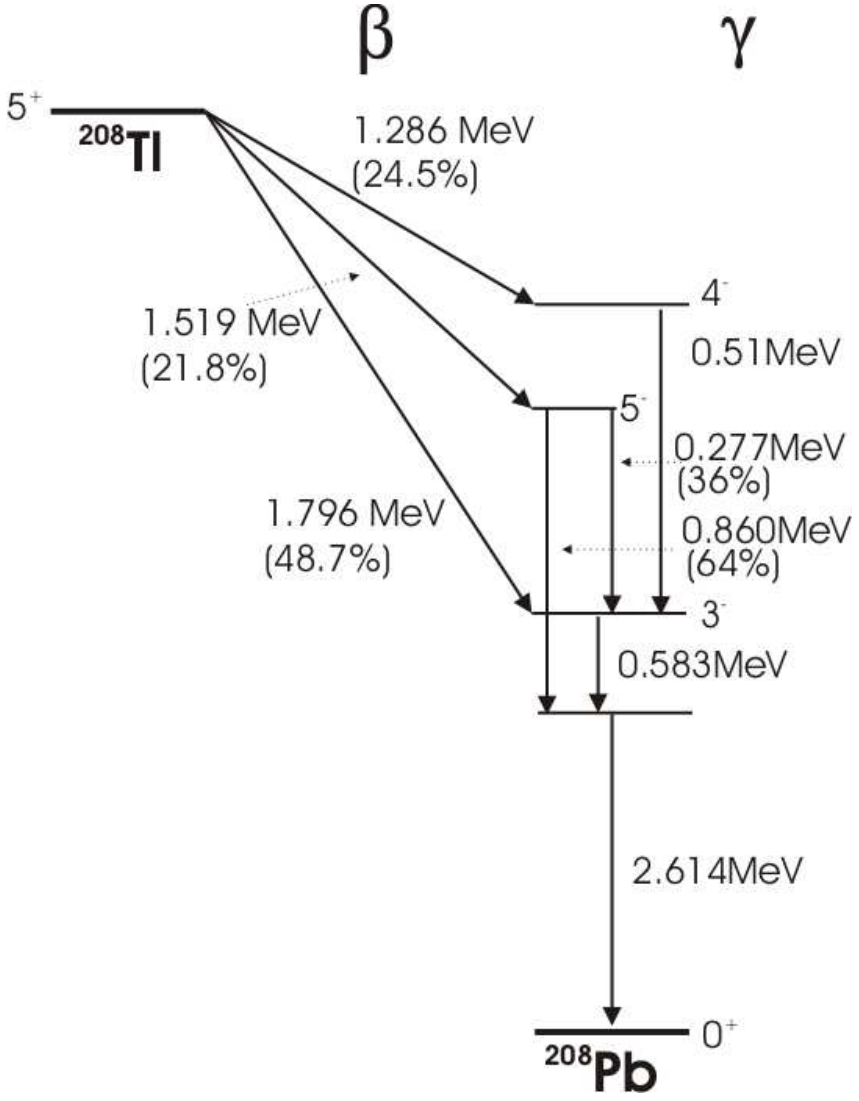

Figure 5.3: ^{208}Tl decay scheme.

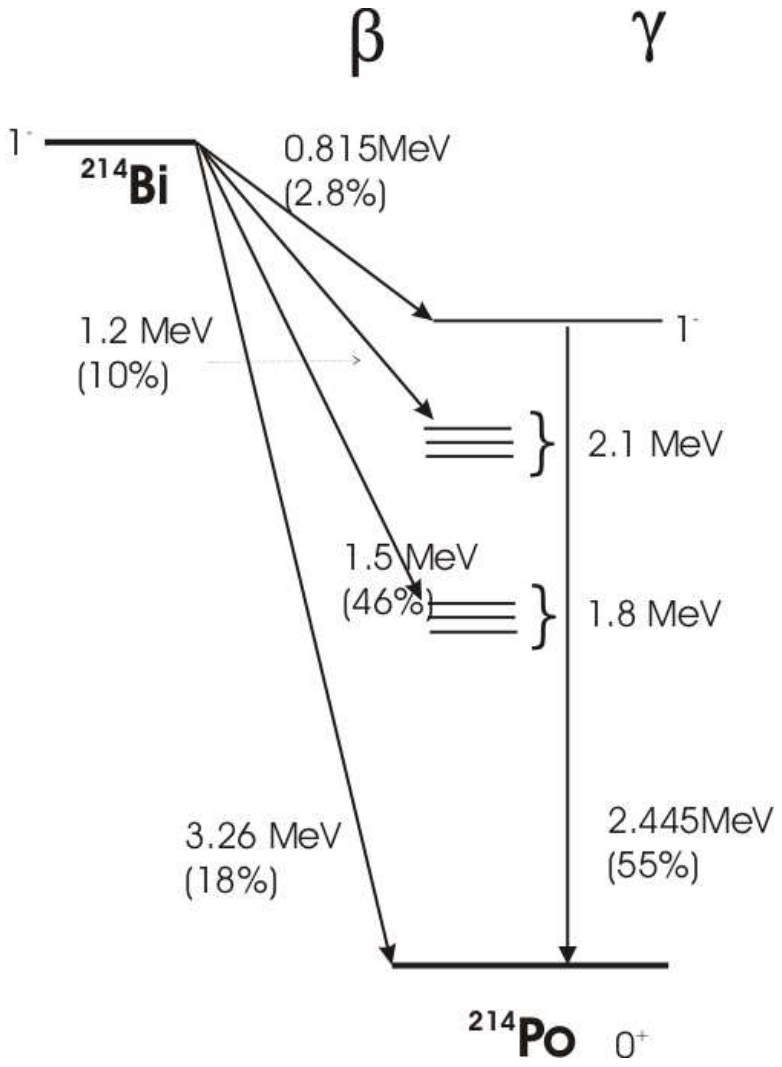

Figure 5.4: ^{214}Bi decay scheme. There are also several very small branching ratios to γ rays >2.2 MeV which increase the total branching ratio to $\sim$ 2%.

5.3.2 Uranium

^{214}Bi is present in the naturally occurring ^{238}U decay chain, but Figure 5.4 shows that only $\sim 2\%$ of the γ rays have energies greater than 2.2 MeV. This means that much higher levels of ^{214}Bi are required to produce the same number of neutrons via photodisintegration as ^{208}Tl. The 0.021% branching ratio of ^{214}Bi to ^{210}Tl, which has only a 1% branching ratio to γ rays exceeding the photodisintegration threshold, is assumed to be so small it may be ignored. ^{234m}Pa emits a 2.21 MeV β particle which contributes $\sim 6\%$ of the Čerenkov light in the ^{214}Bi signal. Studies in the D_2O phase [62] determined that in the given monitoring window this would account for only about 1% of the events attributed to ^{214}Bi decays, and so its effect is considered negligible.

Approximately 20% of the ^{214}Bi decays are to the ground state, emitting a 3.27 MeV β particle. The number of ^{214}Bi decays that would yield one neutron in SNO, using detector simulations, is 32051 ± 962. As a daily upper limit, the levels in the heavy water region must be maintained at $< 30 \times 10^{-15}$ g/g, also derived using Equation 5.2. The cross section of photodisintegration for a γ ray of this energy is 0.8 mb, significantly smaller than the Compton collision cross section of 130 mb. After scattering, 7.2% of the γ rays still have sufficient energy to cause photodisintegration.

5.4 Additional Radioactivity with the Addition of Salt

The neutron capture rate was enhanced in the salt phase through the addition of 1950 kg of salt (NaCl) to the D_2O. The majority of neutrons produced capture on ^{35}Cl rather than deuterium (the cross sections for thermal neutron capture are 44 b compared to 0.0005 b respectively). The addition of salt provides an extra source of background neutrons through ^{23}Na activation, which has a thermal neutron capture cross section of 0.40 b [64]. Neutron capture on ^{23}Na from the salt creates ^{24}Na which decays to ^{24}Mg with a relatively short half life of 14.96 hrs and releases a 2.75 MeV γ ray, as shown in Figure 5.5. The 2.75 MeV γ ray can produce a neutron through photodisintegration if it captures on a deuteron nuclei, with a probability of occurrence 2.6×10^{-3}. The neutron may either capture on deuterium or on ^{35}Cl, (Eqn 2.7, 2.8), mimicking the NC reaction.

The neutrons necessary to initiate ^{23}Na activation can come from naturally occurring

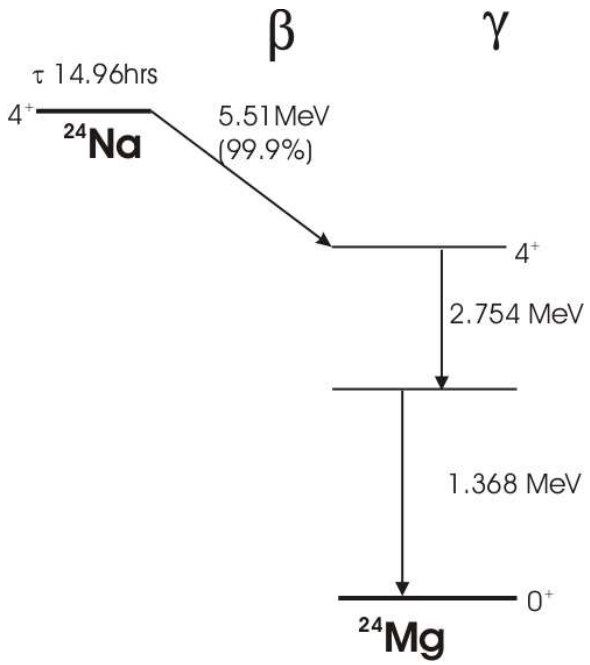

Figure 5.5: The ^{24}Na decay scheme includes γ rays capable of photodisintegration.

radioactivity within the rock cavity around the detector. The ^{232}Th arrives at a stable state, ^{208}Pb, through six α and four β decays. The ^{238}U arrives at a stable state, ^{206}Pb, through eight α and six β decays. All fourteen of the α particles are above threshold for neutron production via capture on ^{16,17,18}O since ($E_{min}(\alpha) = 2.215$ MeV); see Figs 5.1, 5.2. The β decays produce γ rays, which in the case of the decay of ^{208}Tl $\rightarrow ^{208}$Pb, E(γ) = 2.614 MeV exceeds the photodisintegration threshold.

The ^{238}U is able to produce neutrons via fission reactions as well as (α,n) reactions. If the 2.445 MeV γ ray, emitted as ^{214}Bi decays to ^{214}Po, Figure 5.2, is able to leave the rock and enter the D_2O water systems, then it can also produce a neutron through photodisintegration.

The neutrons produced within the rock or from γ rays in the rock would present a sizeable background problem to the NC reaction, but normally all of them are shielded out with the 7000 tonnes of H_2O that surround the D_2O. However the neck and water circulation systems do not have this light water protection and are vulnerable to the ingression of rock wall neutrons and γ rays whose energy exceeds the photodisintegration threshold. Once the neutrons have entered the D_2O via the neck or circulation systems they can capture on the ^{23}Na in the salt. The 14.96 hr half life of ^{24}Na allows it to arrive

within the D_2O fiducial volume if the water is circulating, where the 2.75 MeV γ ray produced in its decay to ^{24}Mg can give rise to a neutron. Without fully understanding the source of these neutrons, the amount of ^{232}Th would be overestimated, leading to a larger photodisintegration rate attributable to radioactive backgrounds rather than neutrinos.

Two studies have been conducted and are presented below, that give confidence that the neutrons from ^{24}Na can be determined such that remaining neutrons in the low energy region are only attributable to ^{232}Th or ^{238}U contamination or the very small levels of neutrinos. Levels have also been calculated for time periods split into day and night portions, for subsequent use in a day-night asymmetry analysis.

5.5 Modelling the Salt Activation

The calibration sources ^{16}N, ^{252}Cf and ^{232}Th produce γ rays and neutrons, and hence ^{24}Na within in the AV. There are three other main regions of ^{24}Na production: in the neck, in the heavy water pipes in the utility room, and in the reserve tank used to maintain the heavy water level in the AV. When there is no active D_2O circulation, there are only a few ^{24}Na produced within the analysis fiducial volume ($R < 550$ cm). These come from ^{24}Na produced in the neck of the vessel, which is not shielded by light water from radiation from the rock of the cavity. When there is active circulation, as in an assay or a level adjustment maintenance, the amount of ^{24}Na is increased, as ^{24}Na is injected from the pipes and the reserve tank into the AV; there is also an increased amount of ^{24}Na drawn down from the neck into the fiducial volume.

Using ^{24}Na Monte Carlo simulations there are 6.46 ^{24}Na Čerenkov events for each photodisintegration neutron produced. This is determined by measuring the number of Čerenkov events detected within the *in-situ* monitoring window for a calibration source of known strength and neutron production. As only 2.9% of neutron events lie within this window,[1] their contribution is negligible.

5.5.1 Neutrons from Calibration Sources

As well as capturing on deuteron or ^{35}Cl nuclei in salt, the neutrons from calibration sources can produce ^{24}Na through capture on ^{23}Na, which, because of its 14.96 hr half life,

[1] when compared to the livetime weighted number of NC events from [47]

may decay after the source has been removed from the detector. The emitted 2.75 MeV γ ray can create further neutrons to mimic the NC reaction while neutrino data is being taken. To eliminate the majority of these events, whilst minimising the livetime penalty, a constraint has been placed on data taken after a calibration run. In the standard run selection procedure, if the number of neutrons expected from ^{24}Na activation is $\geq 5\%$ of the SSM flux integrated over the length of the run, then the data are removed. The number

Period	^{24}Na Neutrons
Day	4.18
Night	7.06
All	11.24

Table 5.1: Total number of ^{24}Na neutrons produced within the AV from salt activation after calibration source deployments.

remaining after this constraint on the data [65] is shown in Table 5.1. Source transitional runs and maintenance runs have not been included and are assumed to have a negligible contribution because of their length. Maintenance runs during source deployment are always very short, and transitional runs only cover the time period when a source is being repositioned, which generally takes a couple of minutes.

The number of neutrons produced by the decay of ^{24}Na during the daytime of a run, $n_{\rm day}$, is determined by the number of ^{24}Na atoms at the beginning of a run, $N_{\rm run}$, the time to the start and end of the day, $t_{\rm startday}$ and $t_{\rm endday}$, since the start of the run, and the probability for photodisintegration of the deuteron by a 2.75 MeV γ ray, $P_{\rm PD}$, which is 2.6×10^{-3}. The relationship is:

$$n_{\rm day} = \sum_{\rm run} P_{\rm PD} N_{\rm run} (e^{-\lambda t_{\rm startday}} - e^{-\lambda t_{\rm endday}}) \ . \tag{5.3}$$

Likewise, the number of neutrons produced during the night, $n_{\rm night}$, is given by Eqn 5.3, but with $t_{\rm startnight}$ and $t_{\rm endnight}$. A uniform deadtime of 1.801% [46] is assumed to correct the number of neutrons to the actual livetime of the runs.

It is also possible to remove the periods of time during which high levels of ^{24}Na neutrons have been produced, to form a *reduced livetime* data set. The ideal situation is to cut the *most* neutrons and the *least* livetime.

After cutting out data livetime during assays, the livetime is reduced to 52% if

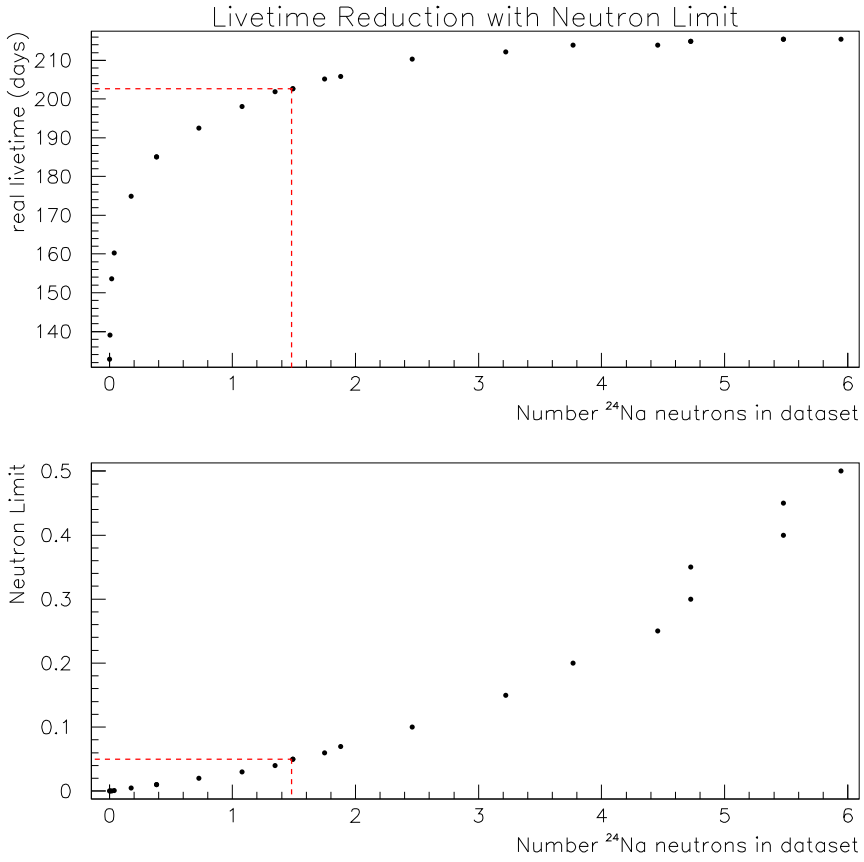

Figure 5.6: Optimising the livetime whilst reducing the neutron contamination from ^{24}Na activation is demonstrated over a preliminary data set of 254 days.

all the neutrons are removed, but Figure 5.6 shows that at least 4 out of 6 neutrons within a preliminary data set can be removed without significantly affecting the livetime. By cutting all runs which are calculated to have more than 0.05 neutrons due to salt activation from a calibration source, only an estimated 1.48 neutrons remained in a data set of 254 days. The livetime is minimally reduced to 78%.

5.5.2 Neutrons from Circulation

The water system lacks the H_2O shielding that the detector has, and so there is a significantly larger ingression of radioactivity from the rock (neutrons and γ rays from ^{238}U and ^{232}Th decay chains) that can cause salt activation in the pipes and the reserve tank. Neutrons from salt activation within the water system and the neck may enter the vessel when there is D_2O circulation. This occurs about 20% of the total period of time the detector is on (rather than actual running time); 86.44 days for the salt data set. The amount of runtime that overlaps with circulation is shown in Table 5.2, and accounts for 47.43% of the total circulation time for the data set. Initial analyses to determine the

Period	Time During Circulation (days)	% of Runtime
All	30.78	7.59
Day	12.67	6.18
Night	18.30	8.10

Table 5.2: Amount of runtime that occurs during circulations over the duration of data taking in the salt phase.

contribution to the photodisintegration neutrons from background levels of ^{24}Na did not calculate the percentage overlap between circulation and runtimes, instead providing only an upper limit on the number of neutrons that could be produced by all the circulations. Large gaps between data taking and circulations, for instance due to long periods of calibration source deployment, would cause this number to be significantly over-estimated as the ^{24}Na levels would have been continually decaying away. It is also unclear how much ^{24}Na would actually enter the AV, and therefore be capable of causing a deuteron photodisintegration, and whether that section of AV would be within the analysis fiducial volume: only then could the resultant neutron be mistaken for an NC interaction. An approximate flow model based on activity seen with a ^{232}Th source deployed in the neck

aimed to reduce the errors on determination of the number of neutrons within the data set from ^{24}Na atcivation.

5.5.2.1 The Flow Model

The fraction of ^{24}Na produced by circulation that enters the fiducial volume is dependent on the flow model used. The model described below is compared to other models (such as flat front) and explained in more detail in [66]. During circulation the heavy water generally enters close to the neck and leaves from the bottom of the AV, taking a certain length of time for the water front to go down a certain distance, x. When circulation occurs at a flow rate of ~ 100 litres/min, observations on the dispersal of a cloud of ^{24}Na produced near the neck indicate that after about $0.5 \rightarrow 1$ day the water front is horizontal. Earlier there appears to be some mixing and the front is curved and extends further into the AV than if it were flat. Mathematical modelling of the front as either a curved or horizontal front indicated that the best approximation was to to that of a curved surface. Thus the front is treated as part of a spherical surface, as shown in Figure 5.7, that intersects the surface of the AV normally and has its centre on the vertical central axis of the AV.

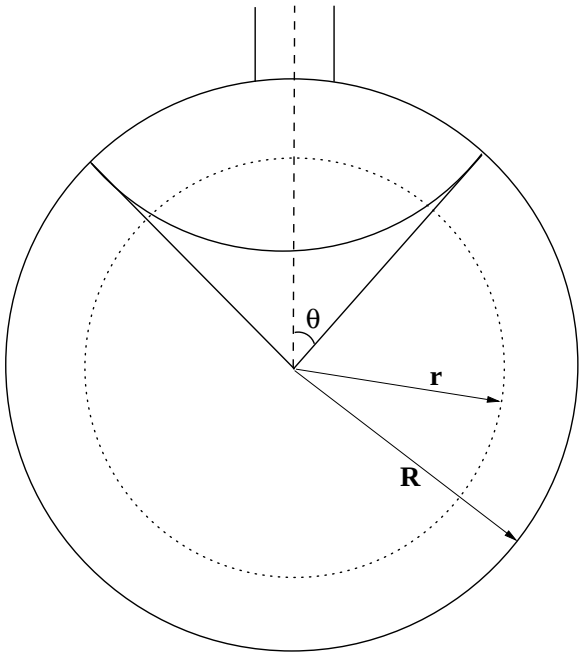

Figure 5.7: Diagram illustrating the curved water front model, taken from [66].

A ^{232}Th source was deployed in the top of the neck to build up a significant level

of ^{24}Na. A short circulation of 6 hrs was then made and Figure 5.8 shows the amount of ^{24}Na brought down into different fiducial volumes during the activation, the circulation and afterwards. Following the circulation, the decay of the activity with a half life of $\sim$ 15 hrs can be seen. The fact that activity is seen within the central fiducial volume of 450 cm indicated that the modelling of a curved water front represents the data better than a flat front would, which would not have allowed for any active water within this region.

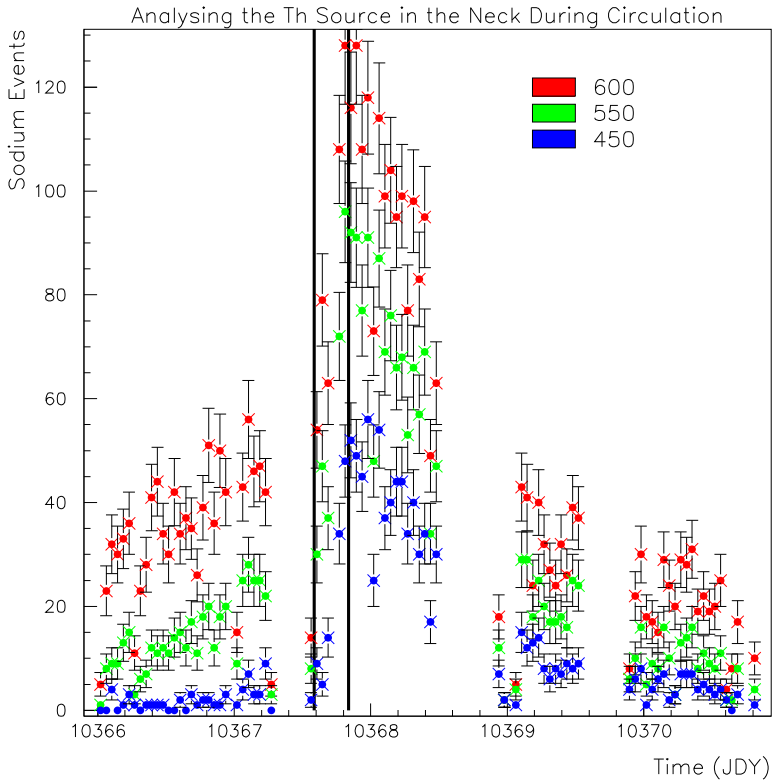

Figure 5.8: Plot showing the distribution of ^{24}Na activity in the AV following a six hour circulation. Before the circulation, indicated by the two vertical lines, ^{24}Na was produced in the neck by deploying a ^{232}Th source.

The fraction $F(t)$ of ^{24}Na within the fiducial volume:

$$F(t) = 1 - \frac{1 - (\frac{r}{R})^2}{2\tan\theta(\sec\theta - \tan\theta)} \ , \tag{5.4}$$

is dependent on the radius r after a circulation time of length t, as well as on the angle θ the front makes to the AV, which in turn depends on the distance the front has travelled. Providing that the fraction of water y contained within the spherical surface is less than

half ($y < 0.46$) that within the entire AV, so that only the upper hemisphere is under consideration, a reasonable approximation for the angle is given by

$$\theta = (1.485 + y^{0.6})y^{(0.35+y/5)} \ . \tag{5.5}$$

In the time interval during an assay, $t_{\rm assay} \rightarrow (t_{\rm assay} + \delta t_{\rm assay})$, a number of ^{24}Na nuclei $\delta N{=}P(t_{\rm assay})\delta t_{\rm assay}$ will be added to the AV per day, where $P(t_{\rm assay})$ is the production rate of ^{24}Na from the neck, pipes and reserve tank at that particular time. A fraction $F(t_{\rm circ})$ of these ^{24}Na flow into the fiducial volume defined by a radius r during a circulation time $t_{\rm circ}$. In the interval $t_{\rm run}$ to $t_{\rm run} + \delta t_{\rm run}$ in the neutrino data taking run, these ^{24}Na nuclei have an activity G:

$$G = \lambda F(t_{\rm circ})\delta N \ \delta t_{\rm run} \ e^{-\lambda(t_{\rm run}-t_{\rm assay})} \tag{5.6}$$

To convert the number of active nuclei into an equivalent number of neutrons, n, requires the probability of photodisintegration: $P_{\rm PD}$. The number of neutrons produced in a given time interval is then

$$\delta n = P_{\rm PD} G \delta t_{\rm run} \tag{5.7}$$

so that the total number of neutrons is obtained by summing over all $\delta t_{\rm assay}$ and $\delta t_{\rm run}$ within the assay times and run times, respectively:

$$n = \sum_{\delta t_{\rm run}}^{t_{\rm run}} \sum_{\delta t_{\rm assay}}^{t_{\rm assay}} \delta n(t_{\rm run}, t_{\rm assay}) \tag{5.8}$$

In this model the short distance ($\sim$ 14 cm) between production and capture of a neutron is ignored, *i.e.* neutrons are assumed to be captured where they are produced. Although the probability of neutron capture in the salt phase is, as shown in Figure 5.9 dependent, on the radial position, the average capture probability, determined as 0.90, has been assumed throughout this analysis. Comparisons between a flat and curved water front model have shown that after the expected flow rate over several hours, the capture rate for ^{24}Na from the water systems would have deviated very little from the average, and thus any corrections would have limited impact on the derived quantity. Therefore it is a reasonable approximation to assume that the neutrons are produced uniformly within the chosen fiducial volume.

Each 10 min section of the data has been analysed to see what the contribution from the current, if relevant, and all previous assays is. These assays were also analysed

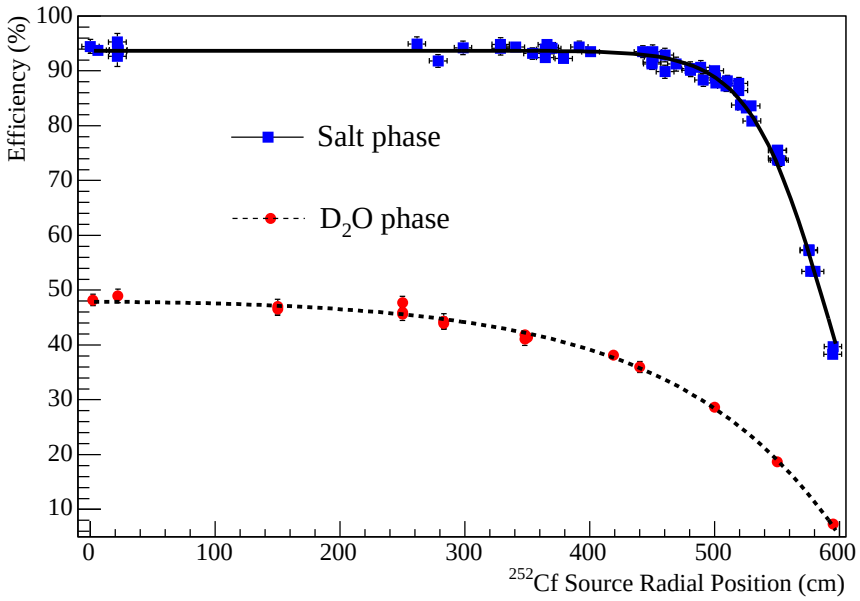

Figure 5.9: The difference is shown between the radial capture profile for neutrons in Phase I and II of SNO. Figure kindly provided by M. Kos.

in discrete 10 min periods. A 10 min period was not computer intensive enough to significantly affect the speed of the analysis, and was found to give only marginally different results from analyses that used even smaller time periods. This was confirmed through comparisons with 5 min, 2 min and 1 min sections over a smaller portion of the data, and so comparison with fewer assays. The contribution from assays more than 10 half lives before a run is assumed to be negligible.

The total number of ^{24}Na produced neutrons over a fiducial volume defined by a radius of 550 cm is shown in Table 5.3, and over a fiducial volume defined by 450 cm (to reduce external background contribution), in Table 5.4.

Period	^{24}Na Neutrons
Day	4.79
Night	3.31
All	8.11

Table 5.3: Total number of ^{24}Na neutrons created in the water systems over the solar neutrino analysis fiducial volume defined by a radius of 550 cm.

The number of neutrons from the water systems can be deducted from the total

Period	^{24}Na Neutrons
Day	1.36
Night	0.97
All	2.33

Table 5.4: Total number of ^{24}Na neutrons created in the water systems over the *in-situ* analysis fiducial volume defined by a radius of 450 cm.

number of neutrons in the data set that are likely to be attributable to background sources, thereby reducing the number of neutron background sources, that remain, to just ^{232}Th, ^{238}U, and neutrinos.

There is still however a tiny residual of 0.49 neutrons from ^{24}Na atoms from the water systems that remain even after removing the livetime when the ^{24}Na were most likely to enter the fiducial volume (when run time overlaps with a period of circulation or within 2 half lives of the end). Times shown in Table 5.5 give an indication of certain periods in the data taking which are expected to have higher than average levels of contamination from salt activation, due to circulation. Runtimes can then be compared to these times to see what the overlap is, and what the contribution from previous assays might be. An indication of the number of seconds that overlap between circulations (or 2 half lives afterwards) and runs is shown in Table 5.6 for only the first 100 runs in the data set.

By performing separate analyses of the low energy backgrounds when modelling the ^{24}Na and when removing time periods containing high levels of ^{24}Na, one can determine how reasonable the model assumptions are. If the modelling does not accurately represent the amount of ^{24}Na actually present in the analysed volume, it will directly affect the prediction of the amount of ^{208}Tl, since the two backgrounds are so correlated across all possible extraction parameters, *e.g.* energy and isotropy. Chapter 6 uses maximum likelihood to statistically separate ^{208}Tl and ^{214}Bi over the full data set when the ^{24}Na is constrained in the fit according to the model presented here, and over a reduced data set where periods of high ^{24}Na contamination have been removed from the data set. The poorer statistics in the latter case should be reconciled by lower uncertainties on the ^{24}Na in the data set. There is very little difference in the determined levels of ^{208}Tl in each case, indicating that the model is valid. Disagreement would have required an estimate of the backgrounds using only the reduced data set, then scaled up to cover the full data set. However, this would assume that there was no temporal variation in the ^{208}Tl and ^{214}Bi

background levels. If it were possible that circulation could have introduced daughters of either of the ^{238}U or ^{232}Th radioactive chains into the detector, their background levels would have been underestimated once these time periods were removed.

Start (m/d, h:m:s)		Stop (m/d, h:m:s)		Length (d)	TSLC (d)
08/02	11 : 25 : 33	08/03	21 : 19 : 20	0.162	0.025319
08/03	09 : 09 : 31	08/04	15 : 34 : 51	0.018	0.002746
08/09	13 : 44 : 05	08/10	20 : 41 : 57	0.040	0.006271
08/23	17 : 56 : 26	08/25	00 : 23 : 23	0.019	0.002917
09/10	15 : 01 : 35	09/12	19 : 17 : 20	0.928	0.144706
09/11	21 : 38 : 39	09/15	17 : 01 : 57	2.558	0.399017
09/19	11 : 25 : 27	09/20	20 : 15 : 47	0.118	0.018455
09/24	12 : 41 : 13	09/27	20 : 10 : 58	2.062	0.321719
10/03	11 : 12 : 44	10/04	21 : 07 : 18	0.163	0.025412
10/09	13 : 29 : 23	10/10	19 : 37 : 52	0.006	0.000920
10/10	10 : 19 : 46	10/11	20 : 19 : 09	0.166	0.025927
10/11	09 : 22 : 44	10/12	15 : 42 : 37	0.014	0.002153
10/17	11 : 59 : 22	10/18	21 : 11 : 29	0.133	0.020810
10/22	14 : 43 : 10	10/23	20 : 48 : 16	0.004	0.000546
10/22	16 : 57 : 30	10/26	04 : 43 : 56	2.241	0.349534
10/25	01 : 06 : 13	10/26	20 : 28 : 06	0.557	0.086876
10/31	15 : 23 : 13	11/01	21 : 36 : 58	0.009	0.001482
11/01	10 : 04 : 01	11/02	19 : 09 : 46	0.129	0.020124
11/07	10 : 48 : 21	11/08	20 : 50 : 13	0.168	0.026208
11/14	11 : 23 : 09	11/15	22 : 39 : 18	0.220	0.034242
11/19	11 : 00 : 20	11/21	01 : 10 : 26	0.340	0.053087
11/19	21 : 06 : 54	11/21	07 : 54 : 54	0.200	0.031153
11/20	13 : 07 : 53	11/22	04 : 55 : 27	0.408	0.063648
11/21	02 : 56 : 20	11/24	06 : 16 : 30	1.889	0.294731
11/23	08 : 20 : 24	11/24	20 : 02 : 35	0.238	0.037066
11/27	09 : 13 : 58	11/28	19 : 52 : 50	0.194	0.030217
12/03	13 : 32 : 23	12/05	00 : 10 : 27	0.193	0.030124
12/04	00 : 32 : 24	12/08	21 : 13 : 07	3.612	0.563410

Table 5.5: The assay times that cover the first 100 runs indicate the typical lengths and frequencies of assays. The time periods within these assays are expected to have increased levels of ^{24}Na due to D_2O circulation. The stop date and time is the end of the assay plus 2 half lives ($\approx$ 30 hrs) and TSLC indicates the number of days since the last circulation.

Run	Overlap (s)	Assay Number
20773	31953	2
20807	54919	3
20852	37727	4
21541	51447	6
21562	32680	7
21566	40137	7
21620	10303	8
21628	39086	8
21629	50898	8
21643	7488	8
21674	11982	9
21681	3574	9
21682	4814	9
21693	5902	9
21711	5707	10
21713	3161	10
21715	34807	10
21717	32999	10
21730	11483	11
21736	23843	11
21809	10130	13
21810	12670	13
21865	9680	14
21880	38841	14
21884	16452	15
21898	4003	16
21901	19037	16
21903	36545	16
22063	37937	19
22126	11569	20
22397	20939	24
22399	66478	25
22414	13009	26
22417	1925	26
22418	16522	26
22419	86402	26
22420	36491	26
22444	6204	27
22491	68492	27
22498	6741	28

Table 5.6: The number of seconds in a run that overlap with an assay, or two half lives after one, given for the first 100 runs in the data set. This gives an indication of the amount of time lost if the data set is reduced to exclude high levels of ^{24}Na and also indicates that the amount of time cut from each run varies significantly.

5.5.2.2 Sources Within the Circulation Systems

The number of neutrons attributable to salt activation are further analysed in the subsections below that indicate their particular source within the water system and calculations of the production rate. In each case, the tables indicate the breakdown of the total number of neutrons from the water systems within 550 cm.

Neutrons from the Pipes

The production rate, P, of ^{24}Na from salt activation in the circulation pipes, from γ rays above the photodisintegration threshold, and neutrons within the rock is estimated below. The levels of the main radioactive sources have been estimated as 3.3 ppm ^{232}Th and 1.2 ppm ^{238}U in the norite [67]. The model used assumes that neutrons at a depth of more than 2 m (and γ rays at more than 1 m) in the rock will not be energetic enough to escape from the rock. Within the pipes, these simulations give 17.75 captures per day on ^{23}Na from (α, n) reactions and 8.27 from (γ) reactions so that $P = 26.02\text{day}^{-1}$ [67]. The water systems comprise about 150 m total length of polypropylene piping, of inner diameter 7.32 cm and outer diameter 8.94 cm [63].

Starting with unactivated D_2O in the pipes, an equilibrium number of ^{24}Na in the pipes is achieved after about two half lives ($\sim$ 8 days). When circulation starts, there is an initial spike of ^{24}Na injected into the AV followed by a constant production rate from the (α, n) and (γ) reactions.

Period	^{24}Na Neutrons
Day	2.00
Night	1.38
All	3.38

Table 5.7: Number of neutrons from salt activation within the pipes attributed to day and night time periods.

Neutrons from the Reserve Tank

The level of D_2O in the $\sim$ 150 cm diameter neck of the vessel is carefully maintained, with respect to the level of H_2O, to avoid placing undue stress on the AV. It is constantly monitored through ultrasonic measurements and when the levels change

by more than half of the deadband (typically between 0.4 cm and 0.8 cm) access to the reserve tank is allowed. They may be necessary because of slight temperature drops in the AV or by leaks in the cavity causing the H_2O levels to fall and thus requiring a corresponding level adjust of D_2O. The cylindrical tank is 120 cm in diameter and 190 cm in height. Of two tonne capacity and typically containing 450 l, the reserve tank can accept excess D_2O or provide it to the maintained volume. Any water that flows out of this tank will contain ^{24}Na nuclei from the same sources as for the pipes. All components of the circulation system are situated underground, separated from the rock walls only by layers of shotcrete that act primarily as waterproofing. The production rate is much larger as the dimensions of the tank are much bigger than the diameter of the pipes. There are a total of 291.2 captures per day from (γ) reactions and 24.6 per day from (α, n) reactions [68], and so 0.701 captures per day per litre. The number of ^{24}Na atoms that progress into the

Period	^{24}Na Neutrons
Day	0.24
Night	0.17
All	0.41

Table 5.8: ^{24}Na neutrons from the reserve tank, attributed to both day and night time.

AV therefore depends on the flow rate out of the tank. This is extremely hard to estimate as during the course of a typical assay the valve to the reserve tank may be constantly opening and closing for just a few seconds or minutes at a time. Time periods can be this short because the maximum flow rate through the valve has been estimated as $\simeq 1.5\,\mathrm{l\,min^{-1}}$ [69] and level adjusts typically only require of the order of a couple of litres. Analysis of an assay time period when the valve to the reserve tank was known to have been open almost continually [2] yielded upper and lower estimates on the flow rate as $12^{+8}_{-5}\,\mathrm{l\,d^{-1}}$ [69]. If it is assumed that any flow of D_2O back into the tank would have negligible dilution impact on the activity per litre within the tank, then the ^{24}Na entering the D_2O from the tank is taken to be of constant ^{24}Na concentration. The production rate is then

$$P = \frac{FC}{V}\frac{1}{\lambda_{\mathrm{Na}}}\,, \tag{5.9}$$

[2] such a period occurred during the transition between the salt and NCD phases

where F is the flow rate out of the tank, C is the capture rate for the entire tank and V is the volume actually contained within the tank.

Neutrons from the Neck

External neutrons and high energy γ rays incident on the D_2O in the neck of the AV produce ^{24}Na at a steady rate A in the upper part of the neck. This has been estimated as 70.3 per day[68] and gives rise to a number of ^{24}Na nuclei, K, within the neck at any time. During circulation water is removed from the bottom of the vessel and enters it through the top, *i.e.* near the base of the neck. Thus, any activity within the neck may be drawn down into the vessel during circulation. Even when there is no circulation they may be a slight downwards drift of ^{24}Na atoms within the neck into the fiducial volume. The amount that is transferred down was determined by deploying a ^{232}Th source in the neck. The activity at the base of the neck where the circulated water enters the D_2O is gK when there is circulation, and fK in the case of no circulation. Analysis of the increased activity within the fiducial volume during the source deployment in the neck determined the fractions $g/\lambda = 0.44$ and $f/\lambda = 0.046$ [70]. The *number* of ^{24}Na atoms produced is then given by

$$N = \frac{j}{\lambda} K \ , \tag{5.10}$$

and so the production rate is simply

$$P = jK \ , \tag{5.11}$$

where $j = f, g$, depending on the state of circulation. K then satisfies:

$$\frac{dK}{dt} = -\lambda K + A - jK \ , \tag{5.12}$$

since jK atoms are being dragged down from the neck. This has the solution:

$$K = \frac{A}{\lambda + j}(1 + \frac{j}{\lambda}\ e^{-(\lambda + j)t}) \ . \tag{5.13}$$

The number of ^{24}Na in the neck is initially A/λ and falls to $A/(\lambda + j)$.

5.5.3 Combined Levels of ^{24}Na in the Salt Data Set

Table 5.11 shows the number of total number of neutrons within 550 cm, assuming full mixing of the sodium produced by the calibration sources and thus an homogeneous

Period	^{24}Na Neutrons
Day	1.86
Night	1.26
All	3.12

Table 5.9: ^{24}Na neutrons from the neck outside circulation.

Period	^{24}Na Neutrons
Day	0.80
Night	0.58
All	1.38

Table 5.10: ^{24}Na neutrons from the neck during circulation.

Period	^{24}Na Neutrons
Day	8.00
Night	8.73
All	16.75

Table 5.11: Total number of ^{24}Na neutrons over the analysis fiducial volume defined by a radius of 550 cm.

distribution of the neutrons. Over the livetime of the salt data set, the photodisintegration rates from ^{24}Na are

$$\mathbf{0.043}^{+\mathbf{0.013}}_{-\mathbf{0.011}} \text{ n/d}$$
$$\mathbf{0.045}^{+\mathbf{0.018}}_{-\mathbf{0.017}} \text{ n/d in the day}$$
$$\mathbf{0.041}^{+\mathbf{0.016}}_{-\mathbf{0.014}} \text{ n/d in the night.}$$

These estimates will allow for the statistical separation of ^{208}Tl and ^{214}Bi as described in the next chapter. The photodisintegration neutron rate from each of these radioactive decays will have to be deducted from any determined NC signal before it can be scaled into a measure of the total active solar neutrino flux.

Chapter 6

Photodisintegration Backgrounds

6.1 The *In Situ* Method

The *in-situ* approach, based on Monte Carlo studies by X. Chen [62] and data analysis in the D_2O phase by G. M*c*Gregor [63], observes β particles and γ rays within the D_2O and infers from them the levels of ^{214}Bi and ^{208}Tl, from which the total photodisintegration rate may be deduced. With 1000 tonnes of heavy water the Standard Solar Model predicts a flux of ^{8}B neutrinos which would give $\sim$ 13 neutrons per day via the NC interaction. A limit of one neutron per day from photodisintegration was set for each chain from radioactivity within the heavy water. The *in-situ* technique measures ^{238}U and ^{232}Th by determining the amount of Čerenkov light from the decay of their daughters, ^{208}Tl and ^{214}Bi, in a low energy monitoring window. The conversion to ^{232}Th and ^{238}U amounts uses efficiencies, $\epsilon_{\mathrm{Tl,Bi}}$, as determined by Monte Carlo simulations. The efficiency is defined as the number of events in the window from a number of ^{208}Tl and ^{214}Bi events generated uniformly in the D_2O at a constant rate. However, above the low energy threshold ($\sim$ 4 MeV) the energy spectra are indistinguishable as shown in Figure 6.1, so the individual amounts can not be identified according to their energy. Although 4 MeV is above the energy of the ^{214}Bi emitted β particle, the production of Čerenkov light and its detection are statistically governed processes, and so the amount of light from such an electron can sometimes be the same as the average amount from a 4-5 MeV electron. The relative amounts can be determined however, by looking at the distribution of the PMT hit pattern from their decays; the isotropy of the event.

6.1.1 Statistical Separation with Isotropy

Above the threshold of $\sim$ 4 MeV the energy spectra are indistinguishable, as shown in Figure 6.1, so the individual amounts can not be identified.

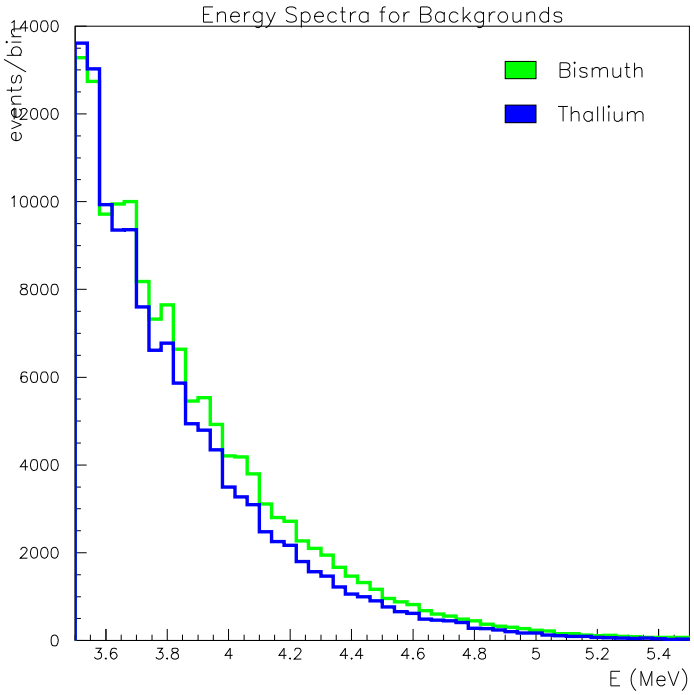

Figure 6.1: The spectra of the low energy backgrounds using Monte Carlo simulations.

The Čerenkov light produced in the decay of ^{214}Bi is dominated, in a low energy region below $\sim$ 5 MeV, by that from β decay to the ground state (Q=3.26 MeV). In the decay of ^{208}Tl the Čerenkov light is dominated by that from several β and γ decays as well as that from the Compton scattered electron from the 2.614 MeV γ ray. This comparison can be seen in Figures 5.1 and 5.2. So, because ^{214}Bi decays are predominantly from a single electron, and ^{208}Tl decays are typically from many electrons, the relative amounts can be determined by looking at the distribution of the PMT hit pattern from their decays; the isotropy of the event. Decays with a single electron give rise to a different distribution of light than those with several electrons, as was shown in Figure 3.4.

This significant difference in the isotropy allows statistical separation of the main background components. Since no information for separation is gained by considering the background dependence on additional parameters, such as energy or radial position,

a one dimensional probability distribution function (1D PDF) is constructed for each of the backgrounds across the allowed isotropy range. Figure 6.2 shows how the isotropy distribution differs for ^{208}Tl and ^{214}Bi Monte Carlo simulations. The most probable

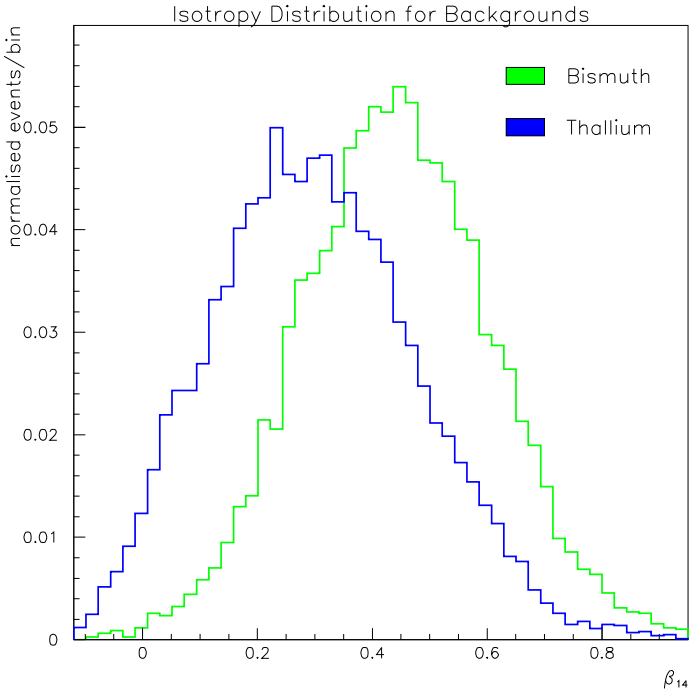

Figure 6.2: The difference in isotropic distributions of Monte Carlo simulations in β_{14} for ^{208}Tl and ^{214}Bi, the primary low energy backgrounds. The distributions have been normalised to unity for an arbitrary number of bins.

combination of ^{208}Tl and ^{214}Bi for a given data set is deduced by maximising the likelihood, $\mathcal{L}$:

$$\mathcal{L} = \prod_{i=1}^{n} P_i(\mathrm{T}, \mathrm{B}) \tag{6.1}$$

where $P_i(\mathrm{T})$ represents the probability that the event is ^{208}Tl and $P_i(\mathrm{B})$ represents the probabiity that the event is ^{214}Bi.

To determine the values which maximise the likelihood function it is simpler to consider the logarithm of the likelihood which will be the sum rather than the product of the probabilities for all observed instants:

$$\ell = \sum_{i=1}^{n} \log(P_i(\mathrm{T}, \mathrm{B})) \tag{6.2}$$

6.1.2 Testing the Maximum Likelihood Method

Figure 6.3 shows the PDFs, in θ_{ij} only, for ^{214}Bi, ^{208}Tl, and a Monte Carlo simulated data set, constructed as a Poissonian distribution of a weighted combination of the two PDFs.

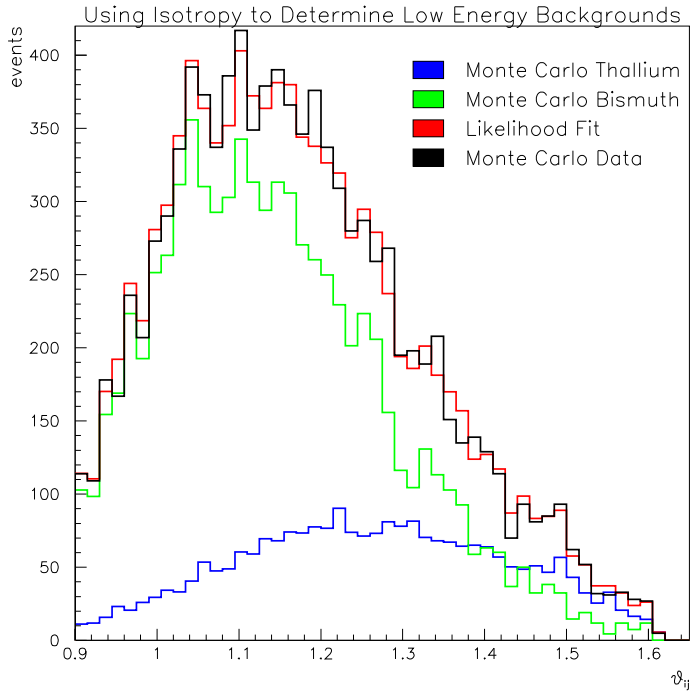

Figure 6.3: Using maximum likelihood to determine the best possible weighting of a set of PDFs for a Monte Carlo simulated data set.

The statistical technique of maximising the likelihood of all fits to determine which combination of PDFs best represents the data is shown in Table 6.1, as an average over 1000 tries, and is in excellent agreement with the Monte Carlo simulated data set, indicating that the method may be relied upon to separate the two signals, providing that any other backgrounds are well enough understood so that they may be accurately constrained.

PDF	MC	$\mathcal{L}$
Bi	7500	7499.01 ± 1.32
Tl	2500	2499.42 ± 1.30

Table 6.1: Maximum likelihood on a Monte Carlo simulated data set.

The maximum likelihood is given in Eqn 6.3,

$$\mathcal{L} = \sum_{\text{events}} (ln(\omega_i P_i) - \omega_i), \tag{6.3}$$

where i indicates the PDF and ω is the binned weight.

6.1.3 Signal Contribution to Background Analysis

Separation within the data set must take account of the ^{24}Na amounts described in the previous chapter, as well as the three neutrino signals, since the data in the low energy region also contains neutrinos, as indicated in the Monte Carlo simulations generated over the salt dataset, shown in Figure 6.4. Since most of the light from the ^{214}Bi decays

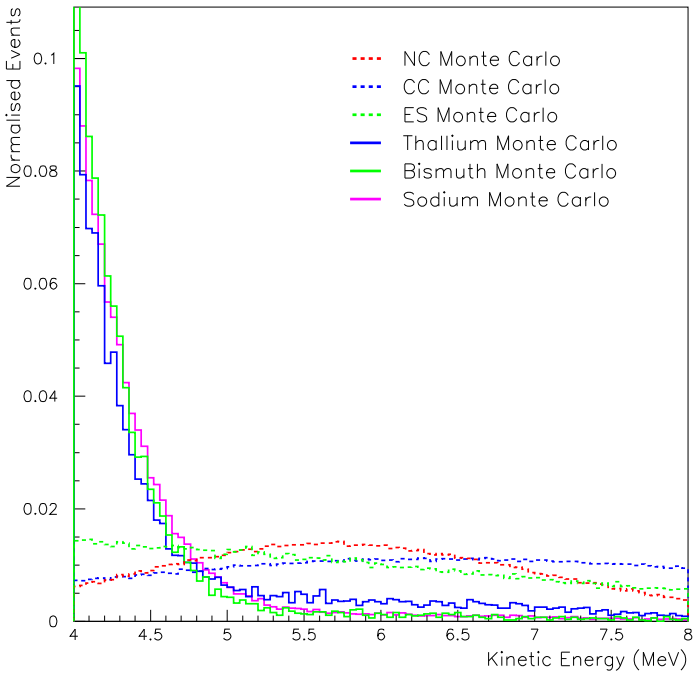

Figure 6.4: The dominant contributions to the low energy signal are radioactive decays from the daughters ^{208}Tl and ^{214}Bi, but there are also contributions from neutrinos and activated ^{24}Na.

comes from β decays to the ground state, it produces Čerenkov light in similar isotropy distributions to that of the electrons from the CC reaction (Eqn 2.3) and the ES reaction (Eqn 2.4). Light from the ^{208}Tl decay however, is dominated by that from the interac-

tion of the 2.614 MeV γ ray and the preceding β γ decays. Its Čerenkov light isotropy distribution is more isotropic and so more similar to that of neutrons. It can not be separated from that of the NC signal (Eqn 2.6). The similarities in isotropy between the backgrounds and the neutrino signals are shown in Figure 6.5.

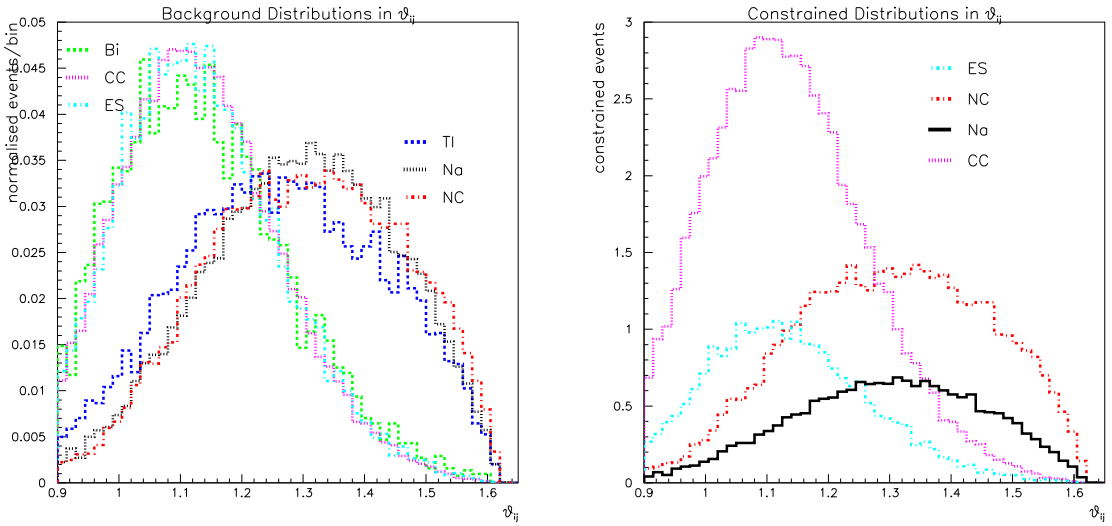

Figure 6.5: The necessity to constrain the isotropy PDFs is shown, along with the constrained PDFs which allow data to be fitted to ^{208}Tl and ^{214}Bi.

Reaction	SSM (%)
NC	1.00 ± 12
CC	0.35 ± 6
ES	0.47 ± 11

Table 6.2: SSM-determined fluxes [71].

Although Figure 6.4 indicates that the energy profiles for the signal and background are quite different between 4 and 8 MeV, isotropy is still the only parameter used to fit out the various backgrounds. Even if the fit were expanded to be two-dimensional, which may be thought to allow more power of separation between signal and background, the energy spectra in the low energy region between the signals themselves are too similar to allow for separation between those with similar isotropy distributions, *e.g.* the CC and ES signals. The neutrino signal is expected to be very small in the low energy analysis region compared to the backgrounds. It was therefore decided to remain with

a 1D fit and to constrain the levels of neutrino signals; *i.e.* they are not treated as free parameters and floated in the likelihood fit. The amounts by which they are constrained are decided according to the SSM values shown in Table 6.2 and the Monte Carlo θ_{ij} or β_{14} distributions are then correspondingly normalised, as shown in Figure 6.5. How well this method works is considered in Chapter 7.

6.2 *In Situ* Analysis in the Salt Phase

The standard salt data set, of 1212 runs over an actual livetime of 391.432 days, is analysed in the following section. The usual suite of selection criteria to remove the instrumental and physical backgrounds, as presented in Chapter 3, constitute the first stage of selection. The events are then selected according to their radial and energetic information to lie within a monitoring window chosen to preferentially select the low energy backgrounds within the D_2O.

To be well above the noise threshold of the detector, and avoid other sources of background (such as background events from the PMTs which are monitored separately) the lowest value for the total energy (when seeing how a shift in energy window affects the amounts) is 4.0 MeV. To minimise the neutrino contribution to this study, (ultimately what is being measured and therefore an undetermined quantity), the upper bound is 4.5 MeV.

The low energy background sample is limited to R$\leq$ 450 cm to remove the ingression of external backgrounds from the H_2O, AV and PMTs. Figure 6.6 demonstrates how important this tight radial cut ($\approx$ 55% smaller than the standard radial cut used in neutrino analyses when considered as a fraction of the D_2O volume) is in order to eliminate backgrounds from external sources.

Unlike the standard signal extraction analyses, no blindness scheme was implemented as neutrino data was not being fitted for, rather it was being constrained according to previously obtained ratios of the SSM, and so there was no possibility of biasing the analysis by looking at all the data. All the cuts are shown in Table 6.3

Fits of the Monte Carlo background PDFs to the data set can be seen in Figures 6.7 and the conversion into levels of ^{232}Th and ^{238}U in units of 10^{-15} g/g[1] is given in Table 6.6.

[1]grams of contaminant per gram of D_2O

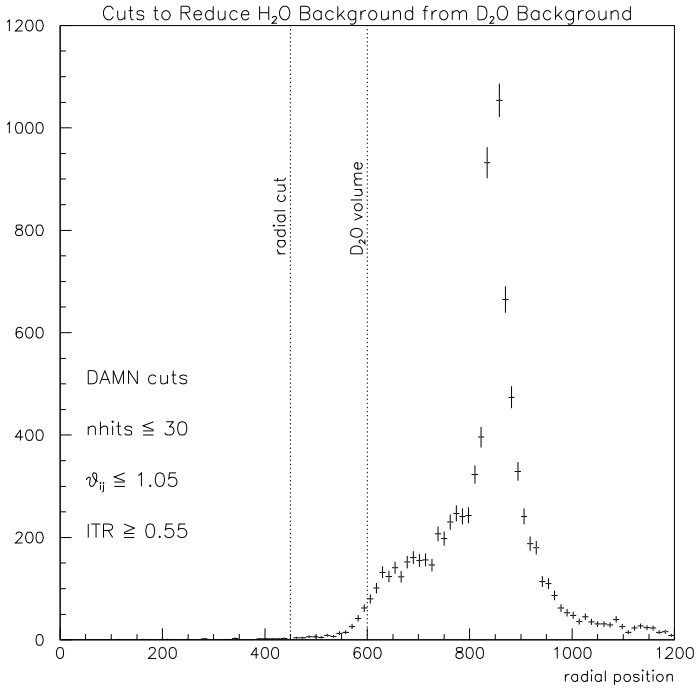

Figure 6.6: Events with low energy and low θ_{ij} are mostly H_2O events.

Parameter	Lower Bound	Upper Bound
KE (MeV)	4.0	4.5
Radius (cm^3)	0	450
β_{14}	-0.12	0.95
ITR	0.55	1.0

Table 6.3: Cuts applied to the data for *in situ* analysis after the removal of the instrumental backgrounds

A 1D+1D fit (the isotropy was conditional on the radius; R$<$ 450 cm) yielded levels of 0.82 and 8.37×10^{-15} g/g ^{232}Th and ^{238}U respectively. A 1D+1D+1D fit (the isotropy was conditional on the radius and the energy: 4.5 $\leq$ Total Energy $\leq$ 5.0 MeV) gave levels of 0.78 and 8.28×10^{-15} g/g ^{232}Th and ^{238}U respectively. These levels are very close (in fact, identical in the case of the 3D fit for ^{238}U) to the values obtained from fitting without accounting for any conditions on other parameters, demonstrating the strength of fitting only over isotropy in the *in-situ* monitoring window.

Type	MC	In $\mathcal{L}$ Fit
Data	-	825
NC	20915	161.1
CC	57558	100.7
ES	15206	35.7
Na	41809	61.5
Tl	10067	$80.0^{+37.3}_{-36.0}$
Bi	7693	$388.7^{+38.3}_{-37.7}$

Table 6.4: The number of events for each PDF within the *in-situ* monitoring window is shown in the left hand column. The number of neutrino events is constrained according to SSM and the ^{24}Na background is constrained according to the number of expected ^{24}Na events according to estimates of the number from the water systems and the number from calibration sources. The fitted backgrounds are shown with statistical errors from the likelihood fit only.

Type	MC	In $\mathcal{L}$ Fit
Data	-	562
NC	15403	118.6
CC	42234	73.9
ES	11151	26.2
Na	30652	11.3
Tl	7354	$58.4^{+30.6}_{-29.4}$
Bi	5670	$271.7^{+32.3}_{-31.7}$

Table 6.5: The number of events for each PDF within the *in-situ* monitoring window over a reduced livetime of the data set to remove large periods of ^{24}Na contamination. The extracted backgrounds of ^{208}Tl and ^{214}Bi for the reduced livetime data set is shown with likelihood statistical errors only.

Background	^{24}Na Model	Reduced Livetime
^{232}Th	$0.94^{+0.43}_{-0.42}$	$0.93^{+0.49}_{-0.47}$
^{238}U	$8.25^{+0.81}_{-0.80}$	$7.82^{+0.93}_{-0.91}$

Table 6.6: The levels of ^{238}U and ^{232}Th, in units of 10^{-15} g/g, comparing the modelling of ^{24}Na produced neutrons and the reduced livetime approach to constraining the ^{24}Na in the fit. The errors shown are statistical only.

6.3 Systematics

Summaries of the systematics are shown below, for the ^{24}Na modelling and the reduced livetime. They were derived by repeating the analysis, having randomly shifted the values

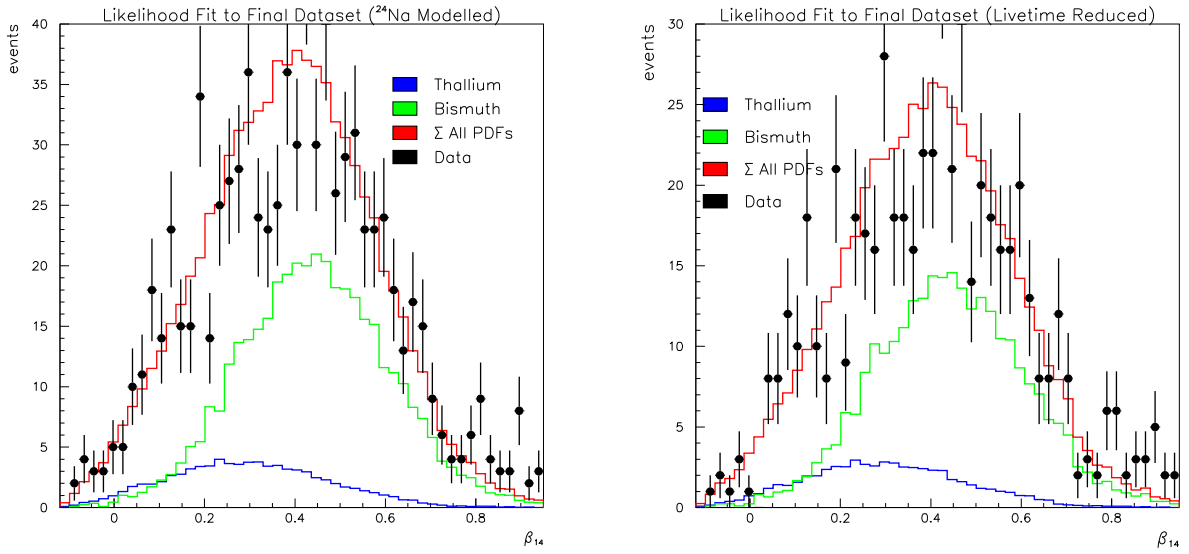

(a) Full Fit

(b) Reduced ^{24}Na Fit

Figure 6.7: Indicating the goodness of fit from maximum likelihood of the background constrained neutrino signal and ^{24}Na background, and ^{208}Tl and ^{214}Bi, to the data set. The left hand figure shows when the ^{24}Na contribution has been modelled, and the right hand plot has a smaller amount of ^{24}Na, reduced through livetime cuts.

of each event according to a upper or lower bound on each parameter in turn.

	^{232}Th (%)	^{238}U (%)
^{24}Na Neutrons from Calibration Sources	$^{+14.8}_{-21.2}$	$^{+0.4}_{-0.4}$
^{24}Na Neutrons from Water Systems	$^{+7.44}_{-23.0}$	$^{+0.8}_{-0.2}$
Normalisation	$^{+10.3}_{-10.3}$	$^{+10.3}_{-10.3}$
NC Flux	$^{+31.9}_{-33.0}$	$^{+1.3}_{-1.3}$
Energy Scale and Resolution	$^{+1.1}_{-31.9}$	$^{+2.3}_{-22.0}$
β_{14} Scale and Resolution	$^{+14.9}_{-12.7}$	$^{+2.5}_{-2.7}$
Sacrifice	$^{+1.0}_{-1.0}$	$^{+1.0}_{-1.0}$
Fitter	$^{+3.0}_{-3.0}$	$^{+3.0}_{-3.0}$
Total	$^{+40.4}_{-58.0}$	$^{+11.4}_{-24.7}$

Table 6.7: Systematics that affect ^{232}Th and ^{238}U levels.

	^{232}Th (%)	^{238}U (%)
^{24}Na Neutrons from Calibration Sources	$^{+0.0}_{-0.0}$	$^{+0.0}_{-0.0}$
^{24}Na Neutrons from Water Systems	$^{+3.2}_{-3.3}$	$^{+0.1}_{-0.1}$
Normalisation	$^{+10.3}_{-10.3}$	$^{+10.3}_{-10.3}$
NC Flux	$^{+34.0}_{-34.0}$	$^{+1.4}_{-1.6}$
Energy Scale and Resolution	$^{+0.0}_{-23.9}$	$^{+8.4}_{-18.6}$
β_{14} Resolution	$^{+13.0}_{-20.6}$	$^{+5.3}_{-1.8}$
Sacrifice	$^{+1.0}_{-1.0}$	$^{+1.0}_{-1.0}$
Fitter	$^{+3.0}_{-3.0}$	$^{+3.0}_{-3.0}$
Total	$^{+38.1}_{-47.7}$	$^{+14.7}_{-21.6}$

Table 6.8: Systematics that affect ^{232}Th and ^{238}U levels, with reduced livetime.

6.3.1 Isotropy

Since the extraction of the number of events uses a one dimensional PDF in isotropy it is important to understand how any errors in the β_{14} resolution might affect the ^{238}U and ^{232}Th determined quantities. Comparing data from both ^{16}N and ^{252}Cf calibration runs to Monte Carlo has allowed construction of energy dependent analytic PDFs in β_{14}. The systematic uncertainties on the mean and the width of the mean were calculated [31] as $\sigma_{\text{mean}} = 0.7\%$ and $\sigma_{\text{width}} = 0.69\%$. These changes are so small that only statistical fluctuations might be seen when the errors are propagated through. The σ_{mean} was increased by varying factors to produce more noticeable effects and the error was scaled accordingly. The error produced by this method was consistent with just changing the PDF by σ_{mean} and σ_{width}.

6.3.2 Normalisation

If the strength of a source is accurately known, one can determine how many decays occur over a specific time period. Factoring in the Monte Carlo efficiency (from a number of events generated uniformly over the AV at a set rate for the livetime of the data set) and a fiducial volume correction allows an estimation of the number of decays expected in the monitoring window. Comparison to the actual number of events gives the normalisation factor.

A ^{232}Th source of strength $1.18(\pm 5\%)\times 10^9\,\gamma$ rays per hour was deployed for 20.25 ± 0.5 hours (t_{source}) in September 2001. The probability of a 2.614 MeV γ photodisintegrat-

ing deuterium is $2.19(\pm 5\%)\times 10^{-3}$. The chance that one of these neutrons subsequently activates ^{23}Na is $1.37(\pm 3\%)\times 10^{-2}$, giving an activation probability of $3.00(\pm 6\%)\times 10^{-5}$. Thus there were 35404 activations per hour, ($R_{\rm activation}$).

Calibration data were sampled over 24 hours ($t_{\rm run}$), starting 9.5 hours ($t_{\rm delay}$) after source retraction. During the runtime there were 200963 ^{24}Na decays as given in Eqn 6.4;

$$N = \frac{R_{\rm activation}}{\lambda}(1-\exp\Big(-\lambda t_{\rm source}\Big)\Big)\Big(\exp(-\lambda t_{\rm delay})-\exp(-\lambda(t_{\rm delay}+t_{\rm run}))\Big). \quad (6.4)$$

The Monte Carlo efficiency, $\epsilon_{\rm Na}$, is the total number of Monte Carlo simulated ^{24}Na decays that are visible within the monitoring window divided by the number of events that were generated uniformly over the AV. The efficiency is 0.0070 over the full livetime of the data set (391.432 days) and a constant generation rate of 0.17 Hz. So the number of ^{24}Na decays expected during this 24 hour run is the calculated number of decays, N, multiplied by the efficiency and a fiducial volume factor. The normalisation is then the percentage difference between the expected number of events and the number actually seen in the data, once a correction for expected backgrounds is made by comparison to a standard run of similar length.

$$\text{Normalisation} = \frac{N\epsilon_{Na}}{\left(\frac{R_{\rm AV}}{R_{\rm monitor}}\right)^3}\frac{1}{(\text{data}-\text{background})} \quad (6.5)$$

Eqn 6.5 gives a normalisation factor for ^{232}Th of 93%. The events are quite uniform across the detector and the strength of the source was reasonable accurately determined.

^{222}Rn is an intermediary in the ^{238}U chain. Its half life of 3.82 days is an ideal length for it to be used as a source to investigate modelling of the ^{214}Bi decays within the D_2O. A ^{222}Rn spike of strength 81 ± 4 Bq [72] was introduced into the detector in February 2003. Circulation of the heavy water for homogeneity across the detector started four days after source deployment and the analysed data of Table 6.9 were taken between 5.13 and 10.50 days after removal of the source. Using Eqn 6.6, the average decay rate $\overline{R}$ over this period of time is 20.37 Bq, a quarter of the original level:

$$\overline{R} = \frac{R_0(e^{-\lambda t_{\rm start}} - e^{-\lambda t_{\rm stop}})}{\lambda(t_{\rm stop}-t_{\rm start})}, \quad (6.6)$$

where $t_{\rm start}$ is the start of the selected runs, $t_{\rm stop}$ is the end of the runs (in time after the source retraction) and λ is the decay constant of ^{224}Rn. An initial rate of 81 Bq implies

Run	Raw Livetime	Deadtime
30122	63001	1113
30123	26883	289
30126	50252	852
30135	61813	924
30138	2469	2
30140	38716	1162
30148	86401	1219
30149	86402	1550

Table 6.9: Livetimes of the mixed ^{222}Rn runs.

a contamination of 6.50×10^{-12}g/g ^{238}U and so an amount of 1.63×10^{-12}g/g over the analysed period, assuming thorough mixing across the AV. 1382 events were selected over the livetime of Table 6.9. ^{214}Bi Monte Carlo generated at 2 Hz over the full data set has an efficiency of 0.0166. Substituting into Eqn 6.7,

$$\text{grams} = \frac{\text{data} \times \text{AU}_\text{U}}{\text{runtime} \times \epsilon_{\text{Bi}} \times \lambda_\text{U} \times \text{N}_\text{A}} \tag{6.7}$$

the data suggests 2.15 mg of ^{222}Rn in the D_2O, or 2.15×10^{-12}g/g. This is a 68% normalisation factor. If mixing were not uniform over the entire D_2O volume there would be a higher concentration of events in the fiducial volume than over the AV. Another explanation for the difference in Monte Carlo and data could be an underestimation of the ^{214}Bi efficiency.

6.3.3 NC Flux

The combined statistical and systematic uncertainty in the NC flux is 13% [71]. This background measuring technique has required fixing the number of NC reactions in the fit as the PDF cannot be distinguished from that of ^{208}Tl for these energies, so this error can have a large affect on the extracted ^{232}Th levels determined from the fitted amount of ^{208}Tl. The number of NC events in the fit must be changed to evaluate this uncertainty. The uncertainties in the CC and ES flux (which account for only 10% and 5% of the number of low energy events) are small enough to have negligible impact on the ^{238}U quantities.

6.3.4 Energy Scale and Resolution

The energy uncertainties are obtained [42] by comparing the energy response for ^{16}N data and simulations. The uncertainty in the scale, determined from a combination of drift, radial, detector asymmetry and source uncertainties is 1.1%. The resolution uncertainty, determined from central run comparisons, is 3.4%. Both the resolution and scale uncertainty have been propagated through the Monte Carlo PDFs. As a check on the stability of the energy window, the study was repeated for two orthogonal energy widths with approximately equal numbers of events; $4.3 \leq$ Total Energy < 4.5 MeV and $4.5 \leq$ Total Energy < 5.1 MeV. The results can be seen in Table 6.10, and seem to indicate that the extracted levels of ^{232}Th are less dependent on the choice of energy threshold than the ^{238}U, which increases with lower energies. This would seem to indicate contamination from other members of the decay chain.

Type	Data	Tl	Bi	^{232}Th	^{238}U
4.3 MeV - 4.5 MeV	872	$75.2^{+40.8}_{-39.2}$	$638.8^{+44.2}_{-39.8}$	0.82	11.94
Reduced	600	$65.0^{+34.0}_{-32.0}$	$449.9^{+37.1}_{-36.9}$	0.96	11.42
4.5 MeV - 5.1 MeV	924	$63.8^{+37.2}_{-37.8}$	$422.5^{+41.5}_{-40.5}$	0.70	8.45
Reduced	627	$50.8^{+32.2}_{-30.8}$	$289.1^{+33.9}_{-34.1}$	0.76	7.85

Table 6.10: Orthogonal energy window checks, for both the ^{24}Na model and reduced livetime for the data set. ^{208}Tl and ^{214}Bi are shown as number of counts fitted by likelihood and ^{232}Th and ^{238}U levels are in 10^{-15} g/g.

6.3.5 Temporal Variations

A rate study over time conducted in the initial stages of the low energy background analysis confirmed that, after removal of certain spikes, the rate was reasonably uniform over the salt phase. However, without performing any time binned *in-situ* analysis it was not possible to tell if the uniform rate was indicative of uniform levels of ^{208}Tl and ^{214}Bi, as the levels could have fluctuating with respect to each other. The lack of large statistics prevented a very thorough investigation of variations in the separate background levels. However, a fit to the low energy backgrounds was carried out on four time periods within the salt data set. Each section contained a quarter of the background events, rather than a quarter of the running time. Splitting the time equally could leave certain

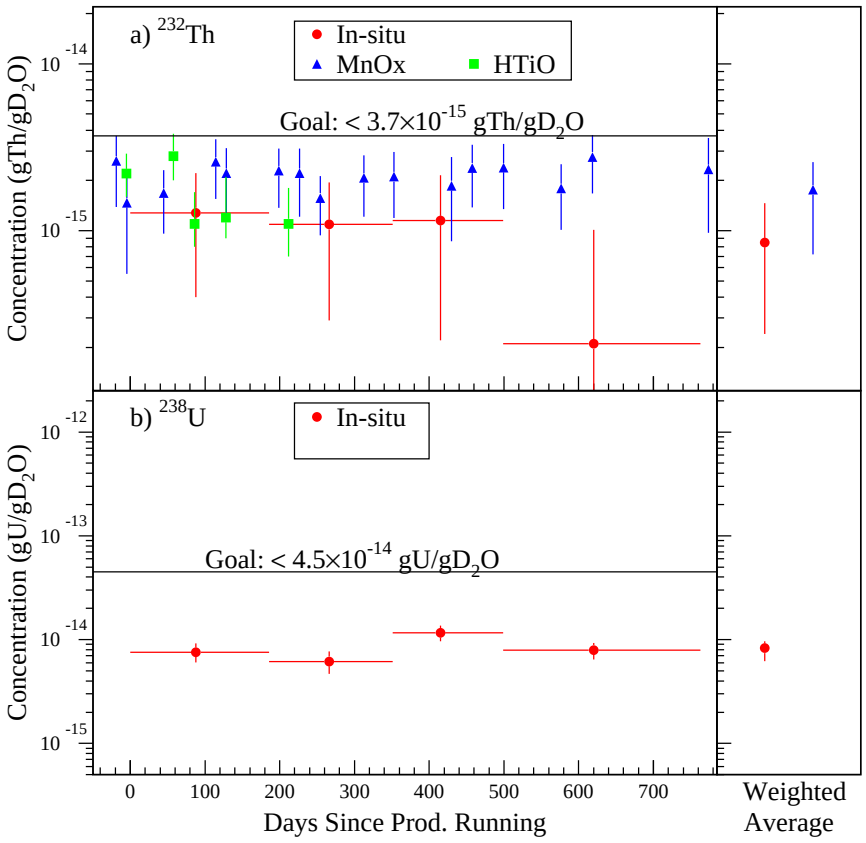

Figure 6.8: The ^{232}Th and ^{238}U levels show little variation over time. The *in-situ* method was statistically limited to performing only four temporally separate analyses. The weighted average of the *ex situ* ^{2}22Rn appears as an upper limit only. This is due to intermittent background appearing in the Radon extraction process.

bins very statistically limited, given that the detector deadtime is not wholly uniform, mainly because of source deployment. The results of the four analyses, each fitting out between 205 and 207 events depending on run boundaries, are shown in Figure 6.8, the central point indicating the temporal occurrence of the median event, rather than the time average for that bin. They did not indicate severe bias in the temporal distribution of the backgrounds, since the number of fitted ^{214}Bi events was relatively constant, and although the extracted numbers of ^{208}Tl events showed significant variation in the last bin, the results were overwhelmed by the large associated statistical error.

Signal	Timebin 1	Timebin 2	Timebin 3	Timebin 4
NC	40.09	45.15	33.4	42.4
CC	25.39	28.2	20.71	26.44
ES	8.94	9.93	7.35	9.51
Na	16.23	17.43	7.73	20.16
Tl	$25.4^{+18.3}_{-17.4}$	$26.3^{+20.7}_{-19.3}$	$20.9^{+18.1}_{-16.9}$	$5.0^{+19.1}_{-6.0}$
Bi	$86.8^{+19.1}_{-17.8}$	$80.7^{+20.3}_{-19.7}$	$114.4^{+19.6}_{-19.4}$	$100.8^{+17.2}_{-18.8}$

Table 6.11: The number of extracted and constrained events in four time bins to investigate any temporal variation in radioactive backgrounds.

6.3.6 Additional Systematics

Sacrifice

The systematic error due to sacrifice was taken as 1%. This is the same value as that used in the standard analysis window that has a large radius (550cm) and a higher kinetic energy threshold of 5.5 MeV.

The Fitter

Evaluation of the vertex shift uncertainty in the fitter of 1% gave a volume uncertainty of 3%.

Neck

In analysis on the preliminary salt data set [47] (254 live days) the number of ^{24}Na neutrons from the neck was *only* treated as a systematic and was not included in the constrained ^{24}Na isotropy PDF. There was no error associated with the number of calibration neutrons, and they were assumed to have been evenly distributed across the fiducial volume. A better estimate, used in this analysis, took the fraction of calibration time that occurred within a radius of 450 cm; for the ^{252}Cf source this was 55%. The lower limit assumed that the calibration sources were uniformly distributed throughout the D_2O so that 42% of the calibration neutrons occurred within this volume. The upper limit assumed that this volume contained 75% of the neutrons produced, allowing for calibration sources outside the fiducial volume to produce neutrons inside it. Error on the production rates in the pipes, reserve tank and neck was estimated as $\pm$50%.

Radius

The radius of the monitoring window was extended out to 500 cm to increase the size of the data set. Out of 1284 events, the fit determined $48.6^{+43.4}_{-42.6}$ to be ^{208}Tl and $733.4^{+42.6}_{-47.4}$ to be ^{214}Bi events . This is equivalent to $0.43 \pm 0.38 \times 10^{-15}$ g/g ^{232}Th and $11.67^{+0.68}_{-0.76} \times 10^{-15}$ g/g ^{238}U, suggesting non-negligible contamination from external $\beta\gamma$ decays of Radon in the light water. The overwhelming number of ^{214}Bi events implied that a tighter fiducial volume was preferable for this study, and levels taken at R$<$ 500 cm underestimate the ^{232}Th and overestimate the ^{238}U.

6.4 Day Night Studies

Studies of the background over the day and over the night were important for a day-night solar neutrino analysis to investigate possible spectral distortions through matter effects. It must be shown that the backgrounds do not contribute towards a day-night asymmetry by not being uniform over a 24 hr time period.

It was important for such a study to have the correct time ordering of the runs. Determination of day or night uses the relative position of the Sun to the horizon, $d_\odot$ with respect to the detector. A positive value assigned to $d_\odot$ places the time during the day and SNOMAN uses astronomical routines to assign all times a value of $d_\odot$ between -1 and $+1$. The time was broken down into 24 zenith angle bins; summing the first 12 gave all the time that occurred during the day, and correlating this with the date allowed this time to be separated into sequential day bins. The first zenith bin to acquire time indicated whether the run started in the day or the night. Using the number of ^{24}Na neutrons estimated within a radius of 450 cm a day night *in-situ* analysis was performed. The systematics were derived in the same way as above. Note that the ^{252}Cf source ran for approximately equal lengths of time in the day and the night, so systematic uncertainty on the number of these neutrons will not affect any calculations of day-night asymmetry.

The fitted number of events converted into levels of ^{232}Th and ^{238}U shown in Table 6.14.

Type	MC	In $\mathcal{L}$ Fit
Data	n/a	376
NC	9453	72.8
CC	26014	45.5
ES	6771	15.9
Na	18764	23.5
Tl	4574	$27.6^{+24.4}_{-22.6}$
Bi	3462	$188.3^{+25.6}_{-25.4}$

Table 6.12: Constrained and extracted backgrounds in the daytime.

Type	MC	In $\mathcal{L}$ Fit
Data	n/a	449
NC	11462	88.3
CC	31544	55.2
ES	8435	19.8
Na	23045	31.4
Tl	5493	$68.0^{+28.0}_{-27.0}$
Bi	4231	$184.6^{+29.4}_{-28.6}$

Table 6.13: Constrained and extracted backgrounds in the night time.

Background	Day	Night
^{232}Th	$0.71^{+0.63}_{-0.58}$	$1.46^{+0.60}_{-0.58}$
^{238}U	$8.89^{+1.21}_{-1.20}$	$7.12^{+1.10}_{-1.11}$

Table 6.14: The levels of ^{238}U and ^{232}Th in units of 10^{-15} g/g for the day and night. The errors shown are statistical only.

6.4.1 Determining the Statistical Correlation

The number of ^{208}Tl and ^{214}Bi events were expected to be highly anti-correlated as they were the only values not fixed in the fit. Shown in Figure 6.10 are the likelihood contours for the extracted number of events in the night, with the best values shown in the centre. The error was determined as the extreme points for each of the two parameters on the $\mathcal{L}_{max} - 0.5$ contour. The correlated errors are graphically represented by the dotted lines on this contour when the error on the other parameter is determined. The angle by which the likelihood contours are rotated off-axis indicates the level of correlation, which is strong and negative for the night and day. Maintenance work during the day limits the

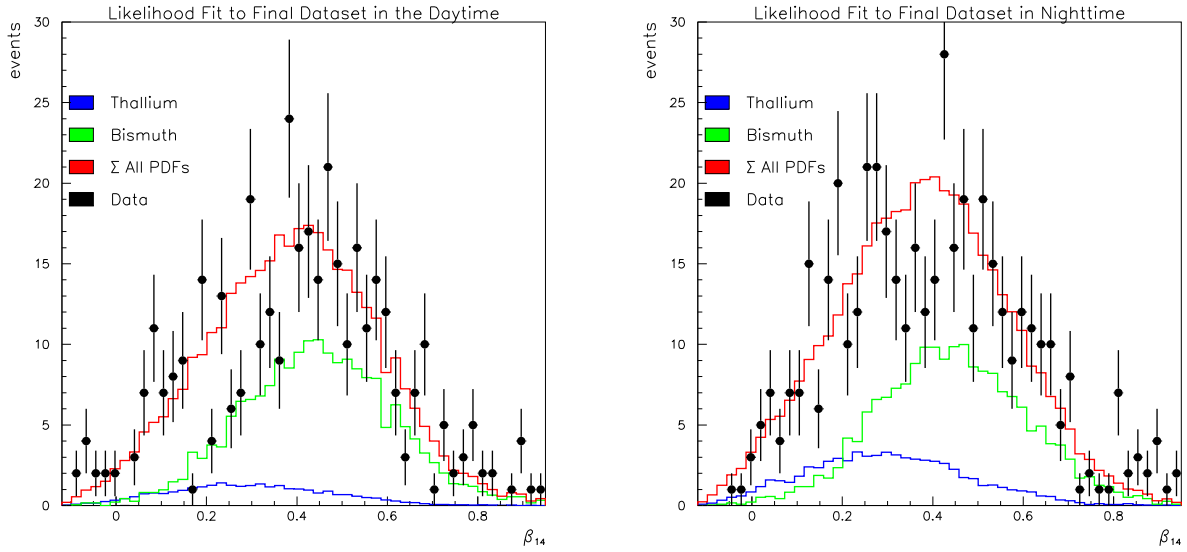

(a) Day Fit (b) Night Fit

Figure 6.9: Indicating the goodness of fit from maximum likelihood of the background constrained neutrino signal and ^{24}Na background, and ^{208}Tl and ^{214}Bi, to the data set for both the day and the night.

statistics and the contours are not particularly smooth, but the degree of correlation is similar to that in the night.

The probability P of two correlated Poissonian distributions, T and B, is [73]

$$P(T,B) = \frac{\sqrt{(2\gamma)}}{2\pi\sigma_T\sigma_B} exp\left(-\left(\frac{T^2}{\sigma_T^2} + \frac{B^2}{\sigma_B^2} + \frac{\rho TB}{\sigma_T\sigma_B}\right)\gamma\right) , \tag{6.8}$$

$$P(T,B) = \alpha\, e^{(\beta(T,B)\gamma)} , \tag{6.9}$$

where γ is a constant that includes the correlation coefficient, ρ. The log likelihood is

$$ln(P(T,B)) = ln(\alpha) + \beta(T,B)\gamma , \tag{6.10}$$

and is maximised when

$$\frac{d\beta}{dT} = \frac{2T}{\sigma_T^2} + \frac{B^2}{\sigma_B^2}\frac{dB}{dT} + \frac{2\rho B}{\sigma_T\sigma_B} = 0 . \tag{6.11}$$

To determine the value of the correlation coefficient ρ, Figure 6.10 shows that when $B = \sigma_B$, $dB/dT = 0$ and so $\rho = T/\sigma_T$. If T and B represent ^{208}Tl and ^{214}Bi then the

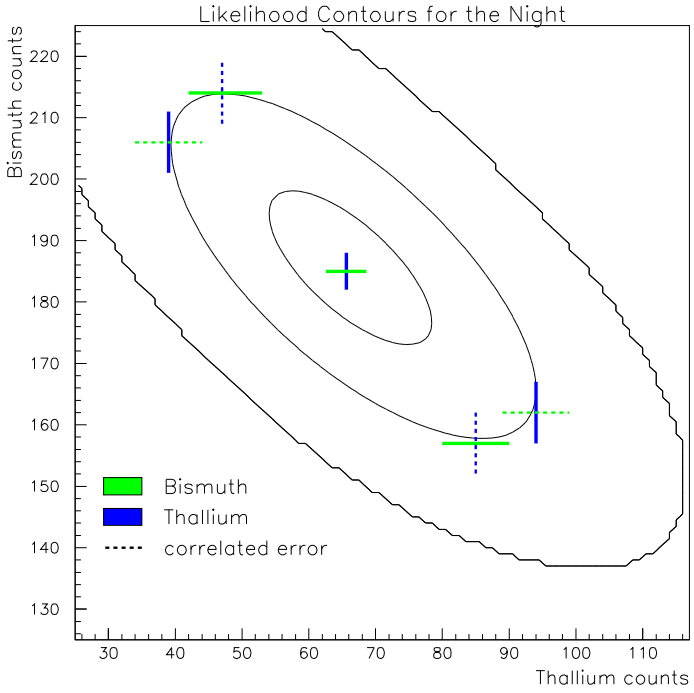

Figure 6.10: Likelihood contours for the extracted number of ^{208}Tl and ^{214}Bi events in the night data set, to illustrate the strength of the correlation and show the width of the statistical errors.

statistical error on the number of ^{208}Tl and ^{214}Bi events is represented by σ_T and σ_B respectively. Hence ρ is the ratio of the value of the correlated error to the actual error.

The correlation can also be determined through the error propagation equation;

$$\sigma_N^2 = \sigma_T^2 \frac{\partial N}{\partial T} + \sigma_B^2 \frac{\partial N}{\partial B} + 2\sigma_{BT}^2 \frac{\partial N}{\partial T}\frac{\partial N}{\partial B}. \tag{6.12}$$

Assuming Poissonian statistics, $\sigma_N^2 = N = T + B + \text{other}$, where other are the neutrino and ^{24}Na backgrounds. The final term is the covariance which can be re-expressed as $\rho = cov(x, y)/\sigma_x\sigma_y$, so that Eqn 6.12 reduces to

$$N = \sigma_T^2 + \sigma_B^2 + 2\rho\sigma_T\sigma_B. \tag{6.13}$$

The form of Eqn 6.13 is valid if the error on the other PDFs is much smaller than the derived uncertainties.

Both methods yielded $\rho_{\rm D} = -0.69$ and $\rho_{\rm N} = -0.72$ in the day and night respectively. Anti-correlations reduced the overall statistical error on the total amount of ^{208}Tl and

^{214}Bi, as shown in the final column of Table 6.15. Note that any asymmetric error here has been symmetrised to simplify calculations.

	^{232}Th	σ_{stat}	^{238}U	σ_{stat}	^{232}Th + ^{238}U	σ_{stat}
Night	0.38	0.15	0.24	0.04	0.62	0.13
Day	0.18	0.15	0.30	0.04	0.48	0.13

Table 6.15: Summary of the day and night photodisintegration rates, showing the statistical error for both ^{208}Tl and ^{214}Bi, and also showing what the combined correlated statistical error would be for a fiducial volume defined by a radius of 600.5 cm.

The total rate for ^{232}Th and ^{214}Bi was determined by a radius of $R < 600.5$ cm, but the ^{24}Na rate was given over $R < 550$ cm. To combine them it was necessary to weight the ^{24}Na rate by a fiducial volume factor. Thus the total internal photodisintegration rate in 600.5 cm^3 is 0.59 ± 0.16 in the day and 0.53 ± 0.14 in the night. The asymmetry on the rate is

$$\mathcal{A} = 2\frac{(N-D)}{N+D} = \mathbf{0.21 \pm 0.28} \tag{6.14}$$

	^{232}Th (%)	^{238}U (%)
^{24}Na Neutrons from Calibration Sources	$^{+15.5}_{-23.9}$	$^{+1.4}_{-7.5}$
^{24}Na Neutrons from Water Systems	$^{+18.3}_{-19.7}$	$^{+0.4}_{-0.2}$
Normalisation	$^{+10.3}_{-10.3}$	$^{+10.3}_{-10.3}$
NC Flux	$^{+43.7}_{-43.7}$	$^{+2.2}_{-0.4}$
Energy Scale and Resolution	$^{+0.0}_{-32.4}$	$^{+3.6}_{-22.3}$
β_{14} Scale and Resolution	$^{+18.3}_{-19.7}$	$^{+3.7}_{-1.4}$
Sacrifice	$^{+1.0}_{-1.0}$	$^{+1.0}_{-1.0}$
Fitter	$^{+3.0}_{-3.0}$	$^{+3.0}_{-3.0}$
Total	$^{+63.1}_{-66.5}$	$^{+12.2}_{-25.9}$

Table 6.16: Systematics that affect ^{232}Th and ^{238}U levels in the daytime.

6.5 *Ex-Situ* Analysis

Another way of monitoring the levels of backgrounds that may cause photodisintegration is to sample the water *ex-situ* for radioactive daughters of the main contaminants. This method is completely uncorrelated to the *in-situ* method, and any of the associated systematic uncertainties. As the name suggests, the procedure involves removing Ra and

	^{232}Th (%)	^{238}U (%)
^{24}Na Neutrons from Calibration Sources	$^{+10.3}_{-16.4}$	$^{+1.1}_{-0.5}$
^{24}Na Neutrons from Water Systems	$^{+5.4}_{-5.4}$	$^{+0.5}_{-0.3}$
Normalisation	$^{+10.3}_{-10.3}$	$^{+10.3}_{-10.3}$
NC Flux	$^{+19.9}_{-20.5}$	$^{+1.3}_{-1.3}$
Energy Scale and Resolution	$^{+0.0}_{-30.1}$	$^{+4.5}_{-20.1}$
β_{14} Scale and Resolution	$^{+8.2}_{-12.3}$	$^{+4.8}_{-2.1}$
Sacrifice	$^{+1.0}_{-1.0}$	$^{+1.0}_{-1.0}$
Fitter	$^{+3.0}_{-3.0}$	$^{+3.0}_{-3.0}$
Total	$^{+26.2}_{-43.5}$	$^{+12.7}_{-22.9}$

Table 6.17: Systematics that affect ^{232}Th and ^{238}U levels in the night time.

Rn through a series of regular assays as described in section 2.2.3, isotopes which are supported by ^{232}Th and ^{238}U, rather than by monitoring the Čerenkov light yield.

There were 16 MnO_x and 6 HTiO assays over the salt data taking period. However, a six-fold increase over the salt phase in the amount of dissolved manganese in the heavy water adversely affected the concentration of Ra when assessed by the HTiO assays. Thus the *ex-situ* values are purely derived from the MnO_x results.

Careful assessment of the assay results was necessary to avoid biasing the *ex-situ* results by including the effect of any activity from the piping between the AV and the MnO_x columns. It was possible to isolate components of the water system, for example the heat exchanger or process degasser, and to perform a reduced assay. Such an approach separated component activity, which totalled 486^{+89}_{-74} ^{224}Ra atoms per day, from the total activity outside the AV, found to be 816 ± 165 ^{224}Ra atoms per day; the difference of 330 ± 184 was thus attributed to the piping, and assumed to be uniformly distributed. Subtraction of the ^{232}Th levels (deduced from daily ^{224}Ra amounts) within the piping is a simplification of the assessment of the ^{232}Th levels within the AV; allowances must be made for the ^{224}Ra within the pipes that may flow into the AV during circulation. Just as flow models, with and without circulation, were needed to account for the amount of ^{24}Na activation in the water systems that may be detectable within the fiducial volume, similar methods were used to monitor the flow of activity from the piping into the AV. The final estimate [2] of the ^{232}Th levels within the AV is $1.60 \pm 0.40(\text{stat.})^{+0.64}_{-0.83}(\text{sys.}) \times 10^{-15}$ g/g ^{232}Th, which includes both the uncertainty in the distribution of the activity within

[2] a slightly different version was used for [39]

the piping, and that associated with the assay technique.

6.6 Čerenkov Tail

The *in-situ* analysis has demonstrated that the finite detector resolution results in Čerenkov events occurring in an energy window just above the Q value. It is also statistically possible therefore, that there may be a very small number of such events, a so-called Čerenkov tail, from radioactive decays with energies significantly greater than the Q value, and above the analysis kinetic energy threshold of 5.5 MeV. The majority of these events will have occurred in the external regions (H_2O, PMT and PSUP), where radioactivity levels are not as tightly controlled as in the D_2O. Separate analysis of the internal and external events is required, since there is poorer understanding of the H_2O region due to lack of calibration with sources, and thus larger uncertainties associated with any simulations of events external to the D_2O.

6.6.1 Internal Backgrounds

Internal backgrounds far above the Q value are expected to be low for two main reasons: firstly because the probability of obtaining such a statistical fluctuation is very low, and secondly because the radioactive background levels inside the D_2O are so minimal. It is possible to distinguish internal from external events by imposing a radial cut of 550 cm^3, which removes misreconstructions generally occurring at the edge of the D_2O, and any unscattered γ rays from Čerenkov events near the AV/H_2O boundary which may travel into the D_2O.

The ^{222}Rn spike mentioned in section 6.3.2, of 81 ± 4 Bq, was used to determine a ratio between a detected number of photodisintegration neutrons above a kinetic energy threshold of 5.5 MeV, and the number of visible Čerenkov events. This ratio is converted to a number of actual neutrons produced within the standard analysis window by normalising to the number of neutrons known to have been produced by the source, and factoring in the neutron detection efficiency. The ^{222}Rn spike only provides information on the Čerenkov tail from the ^{238}U chain, and so Monte Carlo simulations were used to extract similar ratios for the ^{232}Th and ^{24}Na background. The ratios of Čerenkov events to photodisintegration neutrons for the three radioactive backgrounds are shown in Table 6.18. Conversion from

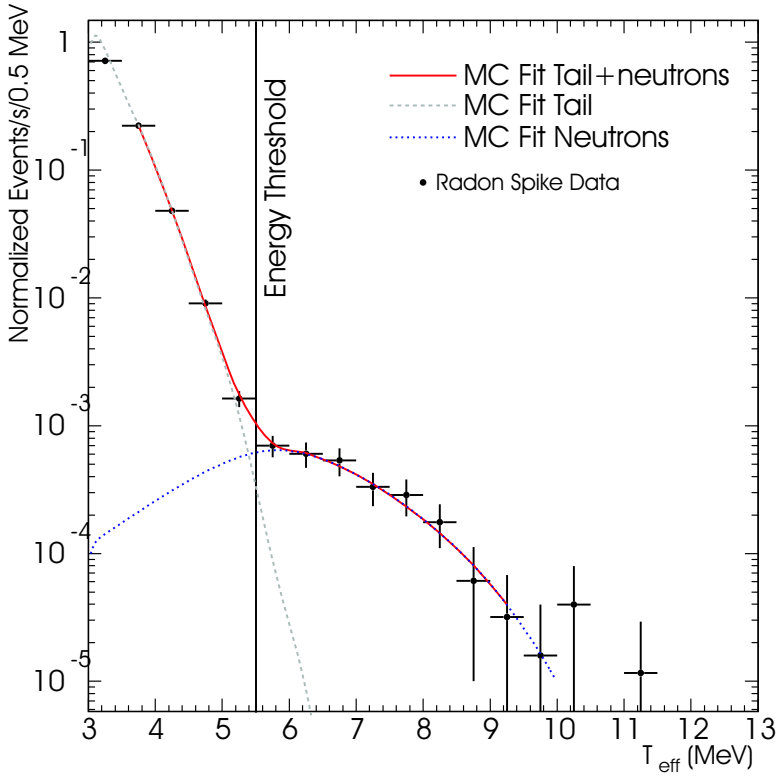

Figure 6.11: The Rn spike data was compared to simulations of Čerenkov $\beta\ \gamma$ events and associated photodisintegration neutrons, to allow an estimate of the number of Čerenkov tail events generated from within the D_2O.

Source	Ratio
^{208}Tl	$0.011^{+0.005}_{-0.002}$
^{214}Bi	$0.053^{+0.011}_{-0.013}$
^{24}Na	$0.090^{+0.024}_{-0.018}$

Table 6.18: The ratio of the number of Čerenkov events to the number of detected photodisintegration neutrons above a kinetic energy threshold of 5.5 MeV, for each of the three background sources. The errors are a combination of statistical and systematic. Figure kindly provided by J. Klein.

the number of photodisintegration neutrons from each chain to the number of Čerenkov tail events requires the number of background neutrons as determined by *in-situ* analysis. Thus a total of $3.6^{+1.0}_{-0.9}$ internal Čerenkov tail events exist in the salt phase [74].

6.6.2 External Backgrounds

External Čerenkov events in the D_2O, such as those that originate from radioactivity in the H_2O or in the PMTs, AV or PSUP, are mostly misreconstructions just inside the D_2O that can largely be eliminated through a radial cut of 550 cm. Monte Carlo simulations in the external regions are not reliable enough to gain an estimate in the number of events that may leak into the fiducial volume, due to of lack of source deployment and poor optical calibration because of increased scattering possibilities over larger distances. The study

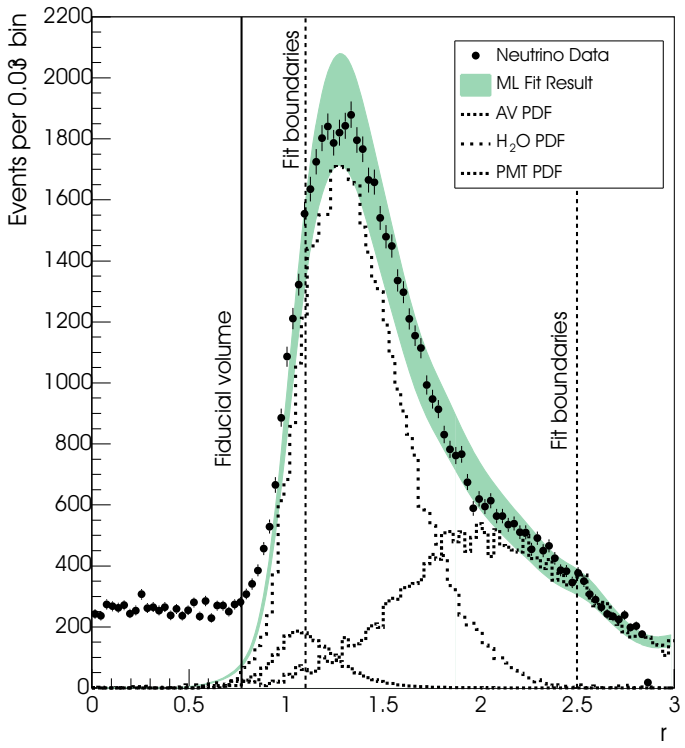

Figure 6.12: A maximum likelihood fit of neutrino data to radial PDFs, constructed from Čerenkov events from background sources in the external regions of the detector. Figure kindly provided by M. Dunford.

therefore relies on a series of sources deployed in various locations in the H_2O. A ^{232}Th source encapsulated in acrylic was used to model events from the AV and from the PSUP, and a ^{222}Rn spike deployed in the H_2O region allowed study of the ^{238}U backgrounds, in much the same way as was done in the D_2O when investigating the internal Čerenkov

events. Figure 6.12 shows how radial PDFs constructed from these sources were fit to the data in a region $1.1 < R^3/{R_{AV}}^3 < 2.5$. A single radial profile was used as it shows very little dependence on the type of low energy background. Results from this fit were then extrapolated into the fiducial volume, since the statistics are so much lower in the actual region of interest. Note that to enhance statistics a slightly lower kinetic energy threshold of 4.5 MeV was used in the analysis, which required additional correction when extrapolating the actual number of external events within the salt data set. The results from the maximum likelihood fit procedure in the neutrino analysis region was consistent with zero events. The 68% upper limit values provided 7, 3 and 11 external Čerenkov events from the AV, H_2O and PMT respectively, with a combined upper limit of 18.5 [39].

6.7 Summary of Photodisintegration Backgrounds

The measured levels of ^{232}Th in the *ex-situ* and *in-situ* analyses are in good agreement with each other. They are combined as a weighted mean to provide the best estimate of the ^{232}Th concentration as $1.22^{+0.72}_{-0.76} \times 10^{-15}$ g/g ^{232}Th, where the errors have been combined in quadrature. The ^{238}U chain is dominated by the temporally dependent ingression of ^{222}Rn. Since the *in-situ* performs a measurement of the ^{238}U levels over the entire neutrino livetime no weighted average between the *ex-situ* and *in-situ* measurements was taken and so the estimated amount of ^{238}U is simply that from the *in-situ* analysis: $8.25^{+1.24}_{-2.18} \times 10^{-15}$ g/g ^{238}U, where the errors have again been added in quadrature.

The photodisintegration rates from these chains can be deduced from Monte Carlo simulations. These show that 3.79μg ^{232}Th and 29.85μg of ^{238}U each produce one neutron per day. The rate of neutron production from photodisintegration from γ rays within these chains is determined as $0.60^{+0.19}_{-0.21}$ neutrons per day within the full fiducial volume *i.e.* within a radius of 600.5 cm.

What has been presented so far is the photodisintegration rate; to convert to the number *detected* requires the neutron detection efficiency and of course, the livetime. This has been calculated [75] as $39.8 \pm 0.5\%$ [3] and translates a number of neutrons produced in a fiducial volume of 600.5 cm to a number detected over a fiducial volume of 550 cm and a kinetic energy threshold of 5.5 MeV, as used in the standard neutrino analysis. If the

[3] this has been slightly updated to 40.7% in [39]

number of neutrons from salt activation (given in section 5.5.3) is assumed to be uniform for the purpose of applying the neutron detection efficiency to allow fiducial scaling to 600.5 cm, then the total photodisintegration production rate from all three radioactive chains within the AV is $0.656^{+0.19}_{-0.21}$ per day. The neutron detection efficiency may then be applied so that over a livetime of 391.432 days there are a total of $102.2^{+29.6}_{-33.1}$ photodisintegration neutrons within the standard monitoring window for a solar neutrino analysis in the salt phase.

Chapter 7

Low Energy Signal Extraction

7.1 Motivation

The energy thresholds for standard analysis of the first two phases (D_2O [76, 71] and salt [47, 39]) were chosen so that any background events present in the data set would have minimal impact on the errors of the extracted neutrino fluxes. Thus, the analysis was limited to a region where the background events were a small fraction of the neutrino events. This limited the ability to test theoretical models related to the shape of the neutrino energy spectrum at lower energies. For example, this region is of particular interest for resolving the question of sterile neutrinos, whose presence would slightly suppress the energy spectrum in the region of 0.5 to 5 MeV [77].

Analysis in this region required a careful separation of backgrounds from the neutrino signals. The CC signal looks very similar to backgrounds produced by ^{214}Bi. Therefore, it is difficult to extend the fitted region to lower energies without constraining the assumed shape of the electron-neutrino energy spectrum. If this were constrained, the analysis region could be extended down to lower energies to enable fitting the neutrino fluxes and testing a particular model of the electron-neutrino energy spectrum, with the advantage of simultaneously fitting the backgrounds.

Previous analyses independently determined the background levels as explained in Chapter 6. The number of photodisintegration neutrons from the radioactive chains, which also provided the number of Čerenkov events in the tail of the internal backgrounds, was calculated over a narrow kinetic energy range of $\sim$ 4.0 MeV to 4.5 MeV. These background events, as well as those from the external Čerenkov backgrounds, were then deducted from the relevant fitted signal to obtain the neutrino fluxes. However,

since the background distributions across certain parameters were distinct enough they could be fitted in parallel with the neutrino signals. This avoided the complication, and associated errors, of having to convert the determined levels of radioactive background which emit γ rays of greater than 2.2 MeV to a number of photodisintegration neutrons, which, in turn, were subtracted from the NC signal. This assumed that the probability of photodisintegration within the simulations was accurately modelled, as described in Chapter 4. Simultaneous fitting of background and signal also meant that the analysis of the Čerenkov tail from internal backgrounds within the signal region was no longer necessary, as the background events across the entire energy spectrum had been taken into account in the fit. Another advantage of simultaneous fitting was that the correlations between all the signals and backgrounds were necessarily incorporated into the fitting procedure.

The *in-situ* analysis demonstrated that the backgrounds in the low energy region were confined to signals from ^{238}U, ^{232}Th and, within the salt phase, ^{24}Na. ^{232}Th and ^{238}U are distinct from each other in isotropy. However, given that isotropy is known to be dependent on the energy [31], its power to separate may vary across the full energy spectrum. This technique did not allow for the fitting of ^{24}Na as it is almost identical to ^{208}Tl across all parameters; fixing its contribution in the fit according to the amounts deduced in Chapter 5 can not be avoided.

The parameters used to separate out the neutrino signals are: kinetic energy[1], isotropy, radial position and the direction to the Sun ($\cos\theta_{\odot}$). The isotropy is parameterised by β_{14} and the radial position by ρ, where $\rho = (R/R_{\rm AV})^3$. The distributions for both signal and background are shown in Figure 7.1. Note that the photodisintegration neutrons from ^{208}Tl and ^{214}Bi are clearly visible on top of the underlying Čerenkov light spectra above ~ 5 MeV.

- The CC energy spectrum reflects that of the underlying ^{8}B neutrino spectrum. The NC energy spectrum depends on the Čerenkov energy spectrum of the γ rays emitted after neutron capture on ^{35}Cl. The ES energy spectrum decreases with energy.

- The NC signal has no dependence on the direction to the Sun, unlike the ES signal (and, to a lesser extent the CC signal).

[1] this is the *effective* kinetic energy of the electron

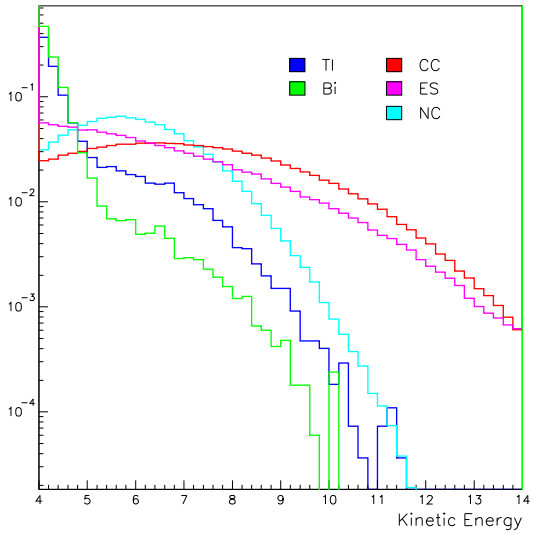

(a) Kinetic energy distribution

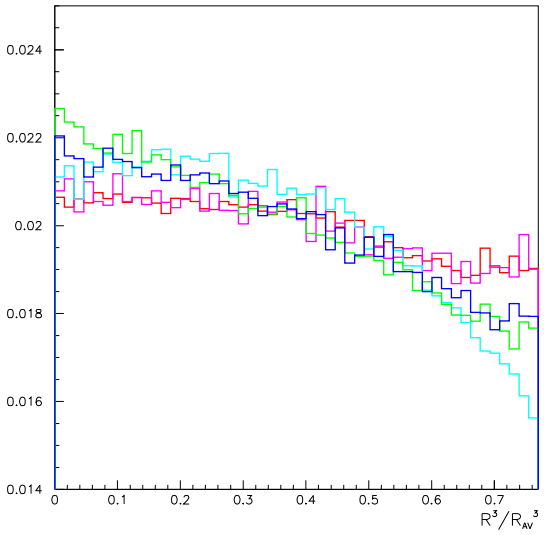

(b) Radial distribution

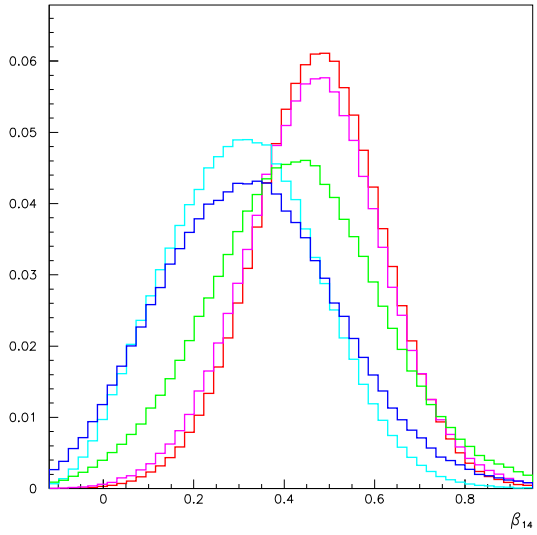

(c) Isotropy distribution

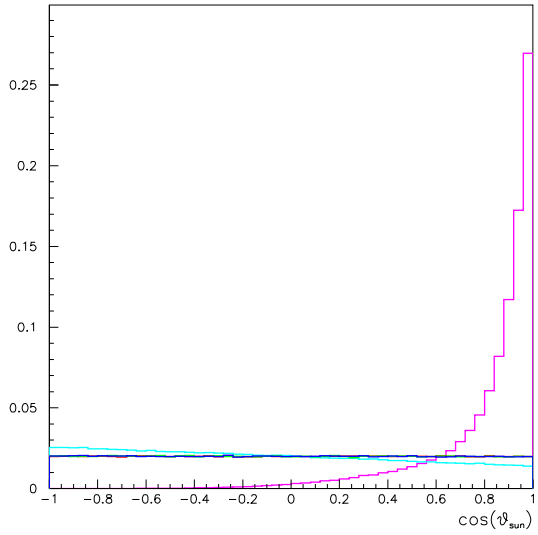

(d) Direction to the Sun distribution

Figure 7.1: Low energy background and signal distributions across the four fitting parameters. Note that the energy distribution is logarithmically scaled and there is an offset applied to the radial distribution for ease of PDF comparison. Each distribution has been normalised to unity across an arbitrary number of bins.

- The isotropy of CC and ES events is quite different from that of NC events, since electron-like signals produce only one Čerenkov ring, but neutron-like events may produce several overlapping rings, giving rise to a broader overall distribution.
- The radial profile is uniform for ES and CC. It decreases slightly for NC at the edges of the vessel, as some neutrons are lost through capture on the AV.

^{208}Tl and ^{214}Bi are not expected to have any $\cos\theta_\odot$ dependence, and to have isotropy and radial dependencies similar to that of NC and CC signals, respectively. However, the marked difference in energy spectrum between signal and background should be enough to separate the NC from the ^{208}Tl and the CC from the ^{214}Bi. This chapter describes the feasibility study that was performed to investigate whether signal extraction with the backgrounds incorporated into the data set was possible.

7.2 Fitting with Maximum Likelihood

A **Ma**ximum likelihood **Fit** (MXF) algorithm was been developed by J. Wilson [41] to allow signal extraction and simultaneous determination of systematic errors. A simulated event with a particular set of parameters has an associated probability of representing a particular event class. The likelihood works to maximise this probability for the sum of events across all the possible PDFs.

Parameter	Minimum	Maximum	Bins
E (MeV)	5.5	20.0	20
ρ	0.0	0.770	10
$\cos\theta_\odot$	-1.0	1.0	100
β_{14}	-0.12	0.95	50

Table 7.1: Standard analysis bounds used to extract neutrino signals in the salt phase.

This code was used on the entire salt data set with thresholds and binning shown in Table 7.1 to perform an energy unconstrained [2] fit [39], using the fitting parameters of kinetic energy correlated with ρ and β_{14}, and $\cos\theta_\odot$ conditional on the energy and ρ. This particular factorisation is shown in Equation 7.1:

$$P(i|E,\rho,\beta_{14},\cos\theta_\odot) = P(i|E,\rho,\beta_{14}) \times P(i|\cos\theta_\odot|E,\rho)\ . \tag{7.1}$$

[2] the shape of the CC energy spectrum is allowed to float

This allows for the fact that $\cos\theta_\odot$ is correlated with two out of the three parameters that are themselves correlated. Assuming that β_{14} and $\cos\theta_\odot$ are independent, *i.e.* they are *only* correlated through their dependencies on their energy and radial position, this probability factorisation takes into account all possible parameter dependencies. The reason for such correlations, and the importance of their correct assessment, will be explored in more detail in the following sections.

As well as lowering the kinetic energy threshold, it was necessary to change the allowed range of some of the other parameters for this analysis, for example ρ, so that external event PDFs do not need to be included in the fit. It was not expected that the ranges of β_{14} or $\cos\theta_\odot$ needed to be altered to perform a low energy analysis.

7.3 Radial Considerations

The standard analysis in salt sets an upper radial threshold of 550 cm and a lower kinetic energy threshold of 5.5 MeV so that the backgrounds have a negligible effect on the data set. Lowering the energy threshold whilst maintaining the same fiducial volume would require fitting for these backgrounds, or at least a more accurate assessment of their contribution, as they may misreconstruct just inside of this fiducial volume (see Figure 7.2. There are difficulties associated with either of these options. Firstly, the optical constants in the light water are not as well understood as in the heavy water because geometrical constraints limit the number and positioning of calibration scans. Secondly, the optical paths are more complicated to model. For example, any Čerenkov photons which travel through the D_2O will have longer path lengths and scatter more. They will also have to pass through the AV twice, undergoing reflection. In summary, the PDFs of events in the light water are a much less accurate representation than PDFs of events in the heavy water, and so it would preferable to not use them.

Another problem with using low energy data at high radii, uniquely associated with the salt phase, is that the distribution of the events from salt activation is not uniform. The calibration sources are approximately [3] homogeneously spread throughout the detector. However, there are slightly more ^{24}Na in the upper half of the detector as that from the water systems descend from the base of the neck into the D_2O. Consider the

[3] geometrical constraints limited deployment at the edges of the vessel and just below the neck

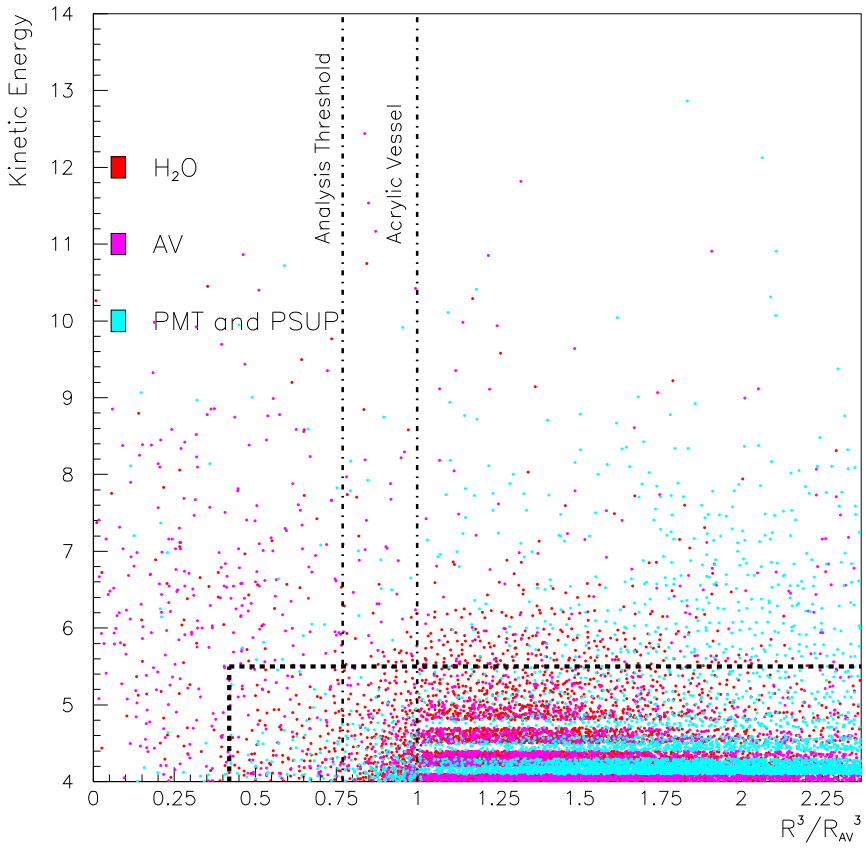

Figure 7.2: PDFs of the dominant low energy backgrounds from the external regions that are present across both the light and heavy water regions.

fiducial volujme used in the *in-situ* analysis defined by a radius less than 450 cm. Because the majority of ^{24}Na events from the neck and water systems will have decayed before entering this small fiducial volume, the variation across the vertical axis of the detector is subtle enough that no adjustment of the radial profile was considered necessary.

This would not be the case for a larger fiducial volume defined by a radius of 55o cm, since the contribution of neutrons from the water systems entering the analysis region from the neck would be considerably larger. Since the radial profile is one of the fitted parameters, it is vital that it is well understood, and the difficulty in obtaining an accurate model of the water flow pattern (see Chapter 5) indicates how substantial the resulting errors could be. Incorrectly determining the amount of ^{24}Na, which can produce neutrons through photodisintegration, would affect the accuracy of the estimate of the number of

NC events. Three possible solutions to this problem are described below.

7.3.1 Reducing the Fiducial Volume

One alternative is to tighten the radial cut such that the tail of H_2O misreconstructed events has negligible impact on the signal extraction. However tightening the radius from 550 cm to 450 cm reduces the volume by 34%. Although the ^{24}Na would still have to be included in the fit, it could be assumed to be distributed uniformly throughout this fiducial volume.

7.3.2 Maximising the Fiducial Volume

It might also be possible to select a radius between that used for standard signal extraction and *in-situ* analysis. This would increase the size of the data set, but without including the external PDFs it would be very hard to determine at what point the levels of external contamination would affect the signal extraction and need to be included within the fit, or at what point the radial profile of ^{24}Na would need to be adjusted.

7.3.3 Imposing a Radially-Dependent Energy Threshold

The final alternative is a radially-dependent energy threshold. Figure 7.2 indicates that the majority of the misreconstructed H_2O Čerenkov events occur in the D_2O at large radii. Therefore, a low energy event may be included in the data set if its radial position reduces the possibility of it being a misreconstructed H_2O background. If it is of higher energy, it is more unlikely to be a background event (see Figure 7.2) and may still be included in the data set, even if its radial position is much closer to the AV.

This radially-dependent energy cut allows confidence that most of the backgrounds which can not be well parameterised have been eliminated from the data set, without unnecessarily impacting the statistics. It was therefore investigated as the best possible method of the three presented here in order to lower the energy threshold.

7.4 Monte Carlo Samples for a Feasibility Study

Sample sets of simulated data created from independent Monte Carlo simulations allowed testing of the hypothesis that the signal and background could be accurately separated.

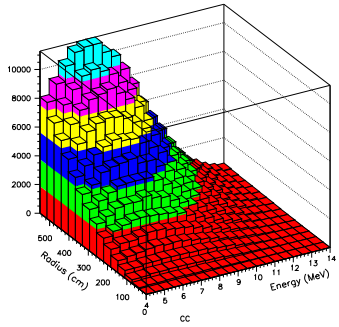

(a) CC distribution

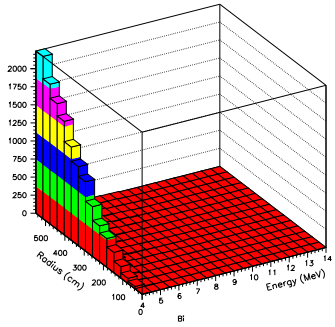

(b) ^{214}Bi distribution

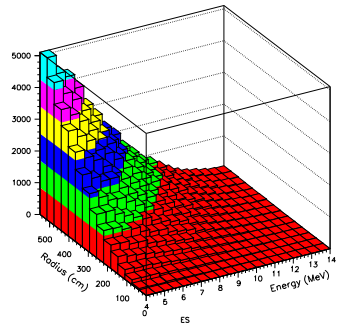

(c) ES distribution

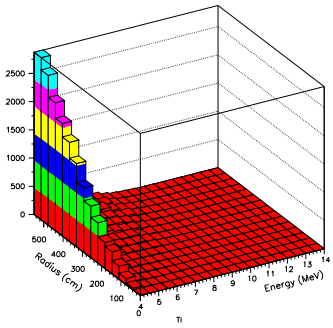

(d) ^{208}Tl distribution

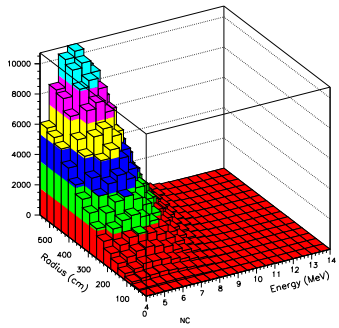

(e) NC distribution

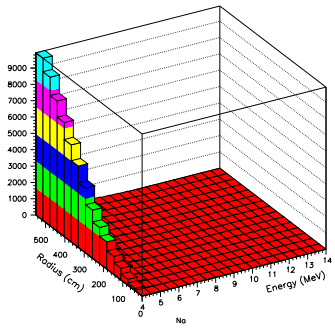

(f) ^{24}Na distribution

Figure 7.3: The energy and radial profiles of signal (left) and background (right) PDFs, shown to illustrate the distribution of information across energy and radius. After application of a radially-dependent energy cut very little information would be lost. The distributions of ^{208}Tl and ^{214}Bi, and ^{24}Na PDFs confirm that there are very few background events expected with energies exceeding 5.5 MeV.

The simulated events were divided into two groups: one half providing events from which the simulated data sets could be drawn, and the other half providing the PDFs against which these simulated data sets could be compared. The simulated data sets were made up of realistic numbers of events derived from the extracted salt phase values [41] for the neutrino signals. The expected number of background events was scaled from *in-situ* results. Generation of the Monte Carlo simulations at 200× SSM allows for 100 samples if fitting only the neutrino signals. Only 10 independent samples were created once the expected levels of background were included since simulations of the backgrounds are much more computer intensive to produce and are much larger to store. Ten samples, however, should still enable reasonable testing to see if separation is possible and not distorted by statistical anomalies. The external neutrons from the AV and the ^{24}Na from salt activation were not considered at this stage of the study.

The level of potential bias can be investigated by running the extraction on each fake data sample and comparing the number of fitted events to the number of known events that the fake data sample has been constructed from. The bias on the extraction of each signal can be defined as the difference between the fitted and expected number of events as a fraction of the error, σ on the fitted result, shown in Equation 7.2. Data which is not significantly biased should follow a Gaussian distribution of zero mean and have a variance of 1.

$$\overline{B} = \left(\sum_{n=1}^{n=N} \frac{F(n) - I(n)}{\sigma(n)} \right) / N \ . \tag{7.2}$$

This can be averaged over the number of samples being tested, N, as shown in Equation 7.2, where $\overline{B}$ is the average bias, F is the fitted value and I is the input value for each sample n. For simplicity, the error on the fitted value was symmetrised (generally the upper and lower errors were fairly similar). Since there are only 10 simulated data sets in this study, Eqn 7.3 predicts an error in the bias of upto ± 0.3, since the error on a Gaussian of width 1 is given by:

$$\mu(G)\sqrt{N} = \sigma(G) \ . \tag{7.3}$$

7.5 Binning Dependence

The number of bins used in the histograms that define the PDFs must be optimised so as to preserve the relevant information, whilst ensuring that there are enough statistics in

each bin to completely characterise the distributions without any significant bias. As the number of correlations is increased the number of bins into which the PDF must be distributed increases by a factor equivalent to the number of bins specified for that additional parameter. This makes the PDF less reliable as certain probabilities will be statistically limited. This effect can be offset by reducing the number of bins per parameter, but this may affect the sensitivity of the fit. A study was performed to analyse how changing the binning for certain parameters altered the mean bias for the simulated data sets.

	Bins	CC	ES	NC	Tl	Bi
A	20* 100 10 50	0.016	0.170	−0.286	1.414	1.574
B	10 10 10 10	−0.524	0.423	−0.004	0.357	−0.071
C	10 10 10 5	−0.555	0.447	−0.010	0.361	−0.047
D	10 20 10 5	−0.541	0.409	0.003	0.408	−0.105
E	10 30 10 5	−0.583	0.444	0.060	0.335	−0.059
F	10 10 15 10	−0.495	0.378	0.024	0.300	−0.430
G	10 5 15 10	−0.396	0.169	−0.005	0.293	0.001
H	20 5 15 10	−0.341	0.015	−0.082	0.422	0.017

Table 7.2: Shown is the mean bias for each of the signals and backgrounds. There is slight bias dependence on the bin width of the various parameters. The asterisk indicates that the energy width extends to 20 MeV and the last bin is 6.5× wider than the others.

Table 7.2 summarises several of the binning combinations (strictly in the order: energy, $\cos\theta_\odot$, ρ and β_{14}) that were employed in the bias tests and shows the average bias over the 10 samples for each of the fitted PDFs.

- The binning used in the standard analysis, A, shows very large (and unacceptable) biases for both the background PDFs. Whereas there is a reasonable distribution of signal across the entire energy spectrum, there is only a slight tail of background events above 5.5 MeV to be distributed across the upper range of the bins. Since there is very little signal in the range 13.5 MeV to 20 MeV, it was decided to lower the upper threshold on energy to 14 MeV. This substantially improved the quality of the fits.

- B indicates that the biases in the backgrounds can be substantially reduced by decreasing the total number of bins, but the increase in bias for the CC and ES signals suggests that correlations have been neglected. This is highlighted by comparison with C, in which the number of isotropy bins has been halved, and the bias increases on

nearly all of the extracted numbers.

- To reduce the bias on ES, the number of $\cos\theta_\odot$ bins was doubled for D. By comparing C and D, one can see the balance that must be achieved between statistical limitations and loss of information; it would be expected that if the only change to the fit was an increase in the number of $\cos\theta_\odot$ bins that the bias on the ES signal would decrease. In fact the bias on ES is higher in D than in C, because there are not enough events in each bin for accurate fitting.

- G was considered to contain the optimal number of bins in each parameter as it yields the lowest overall bias.

7.6 Correlated Parameters

Ignoring certain correlations between the fitting parameters may lead to possible biases in the signal extraction. In the standard salt analysis, a study was performed to assess the dependency between the fitting parameters. Results from the fit factorised as in Eqn 7.1 were compared to those from a fit which only accounted for the correlation between energy and β_{14}. Both ρ and $\cos\theta_\odot$ were considered to be completely independent of the other parameters. This fit accounts for the strong correlation between the energy and the isotropy, but does not allow for any possible correlation with the radial position. There was found to be a 0.8% difference between the results [39]. Described below are some reasons for certain inter-parameter dependencies.

7.6.1 Isotropy versus Energy

Isotropy is correlated with energy primarily because lower energy electrons are more prone to scattering, which smears the edges of the Čerenkov cone and broadens the isotropy.

Neutron events provide a pronounced example, as indicated in Figure 7.4, that the higher the isotropy[4] the lower the energy. A neutron event that gives rise to a lower kinetic energy occurs when a higher than average number of γ rays is emitted. A cascade of γ rays totalling 8.6 MeV is emitted when ^{35}Cl decays to its ground state after neutron capture. Each γ ray loses energy through Compton scattering and scatters off electrons. If

[4] lower values of β_{14} indicate higher values of isotropy

the energy of each of the electrons exceeds the Čerenkov threshold of 0.262 MeV, then each gives rise to a cone of Čerenkov light. Once the electrons are below threshold, the energy can no longer be detected. The loss of energy from below-threshold electrons means that as the number of electrons producing Čerenkov cones increases the total amount of light measured in the event for a given energy will be smaller.

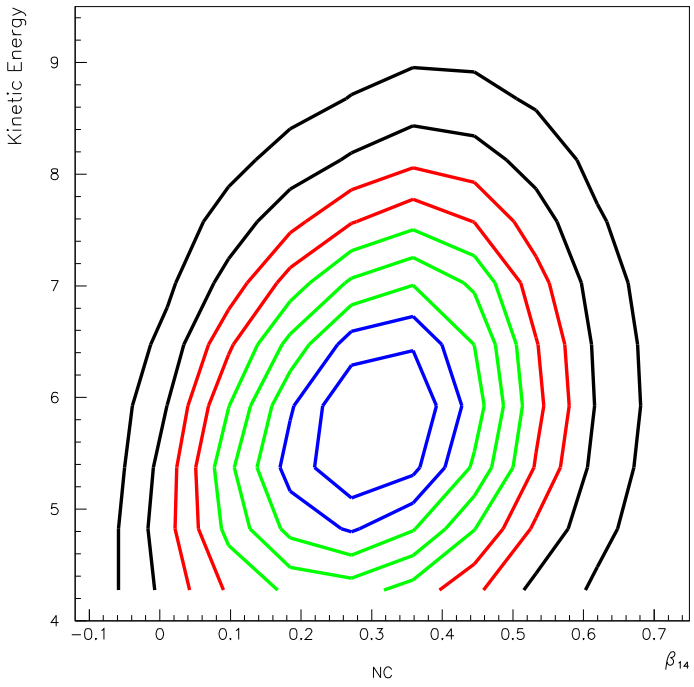

Figure 7.4: Correlation between the kinetic energy and the isotropy of an event is clearly visible in the NC Monte Carlo simulations.

7.6.2 Direction to the Sun versus Energy

The increased scattering of low energy electrons may also cause a slight correlation between energy and $\cos\theta_\odot$. The direction to the Sun can be reconstructed more accurately for higher energy electrons which have scattered less and so provide a more realistic indication of their initial direction.

7.6.3 Position versus Energy

Energy and position are not completely independent of each other. Low energy events have increased scattering and therefore a larger variation in time taken for the light to reach the PMTs. Since the timing residual is used to obtain the position, the reconstructed radius of the event will be smaller (further from the PMTs). This misreconstruction may cause such an event which is produced outside the fiducial volume to be included within the analysed region. This can be seen in Figure 7.1(b). The distributions of the low energy ^{208}Tl and ^{214}Bi fall off towards the edge of the vessel but one would expect a much flatter profile, as is seen in the distribution of CC and ES. They have the expected distribution because they are of higher energy and therefore more likely to have correct reconstructed positions. The reduced number of low energy events at high radii indicates that such events are more likely to be misreconstructed *in* towards the centre of the vessel.

A low energy event also has very few hits in the backward hemisphere. These hits are used in the reconstruction algorithm to determine the point of interaction along the position axis and so, without this information the event is much more likely to be misreconstructed.

Events occurring at the edge of the fiducial volume that are going outwards have a smaller number of PMTs in the field of view on which to project a Čerenkov cone. The same PMT may be hit by several γ rays from a single event, which will only register as a single hit, thus lowering the apparent energy of the event. This effect is expected to be relatively small, given the 3 m distance between the AV and the PSUP.

The radially-dependent energy cut forces a link between these two parameters and so any existing correlation is expected to be enhanced. The effect of such dependencies can be investigated by comparing the biases of fits performed with a variety of PDF factorisations on data sets with and without a radially-dependent energy cut. The various factoristaions used are defined, for the purpose of this thesis, as:

$$\text{2D} + \text{1D} + \text{1D}: \quad P(i|E,\rho,\beta_{14},\cos\theta_\odot) = P(i|E,\beta_{14}) \times P(i|\rho) \times P(i|\cos\theta_\odot) \tag{7.4}$$

$$\text{3D} + \text{1D}: \quad P(i|E,\rho,\beta_{14},\cos\theta_\odot) = P(i|E,\rho,\beta_{14}) \times P(i|\cos\theta_\odot|E)$$

$$\text{3D}: \quad P(i|E,\rho,\beta_{14},\cos\theta_\odot) = P(i|E,\rho,\beta_{14})\ . \tag{7.5}$$

Since $\cos\theta_\odot$ can only distinguish the ES signal (and CC to a much smaller extent), a

3D fit *without* including ES effectively gives the possible biases when using a 4D fully correlated fit, for that choice of binning. The 3D+1D does not account for a correlation between $\cos\theta_\odot$ and radial position.

Fit	CC	ES	NC	Tl	Bi
2D+1D+1D	−0.565	0.252	−0.029	0.212	0.144
3D+1D	−0.380	−0.168	−0.080	0.487	0.208
3D	−0.334	-	−0.110	0.590	−0.252

Table 7.3: The mean biases for 10 fake data sets containing signal and background can be affected by the correlations between the parameters. The events are within a fiducial volume defined by a radius of 500 cm and have kinetic energies above 4 MeV.

Table 7.3 shows the biases for fits above a kinetic energy threshold of 4 MeV and within a fiducial volume defined by a radius of 500 cm, for three different PDF factorisations. There are not significant differences in the overall biases, although the extraction of certain signals is improved by including known correlations. For example, including the correlations between $\cos\theta_\odot$, energy and radial position significantly improves the quality of the ES extraction.

Table 7.4 shows the correlations for fits to events when a radially-dependent cut is applied to exclude events with E < 5.5 MeV events at high radii; > 450 cm.

Fit	CC	ES	NC	Tl	Bi
2D+1D+1D	−0.843	−0.514	−0.672	0.333	2.701
3D+1D	−0.396	−0.169	−0.005	0.293	0.001
3D	−0.345	-	−0.048	0.400	−0.034

Table 7.4: Bias values for the extracted signal and background averaged over 10 fake data sets, after imposing a radially-dependent energy cut on the samples. They show that ignoring correlations between fitting parameters can have significant effects on the quality of the fit.

Here, the correlations can be seen to have a much more significant effect on the quality of the fit. The 3D (and so effectively 4D if ES is ignored) fit shows the smallest possible biases. By comparison to the 3D+1D fit, it can be seen that there is very little increase in the bias as the correlations between $\cos\theta_\odot$ and ρ are assumed negligible. However treating the radial position and direction to the Sun as completely independent parameters leads to significant bias, since the nature of the variable cut implicitly forces

a correlation with energy that is neglected in the fit. Thus the 3D+1D was chosen as the PDF factorisation for an energy-dependent fiducial volume analysis.

7.7 Additional Backgrounds in the Data Set

7.7.1 External Neutrons

On average, external neutrons reconstruct back to the AV, and so have a unique radial profile that should allow them to be separated from other neutron signals [39]. Fits were performed both fixing and floating the number of external neutrons, both methods having very little effect on the fitted amounts of other signals. It is preferable to float signals if possible; the external neutrons were thus included as an additional signal in this analysis.

7.7.2 γ Rays from Atmospheric Neutrinos

Atmospheric neutrinos were calculated to have contributed 8.5 ± 2.2 background internal γ rays. Several of the events overlapped with the multiple events and so above an analysis kinetic energy threshold of 5.5 MeV, $3.2^{+4.6}_{-3.2}$ events were fixed in the fit. The events were constrained to the shape of ^{16}N data, which produces γ rays of approximately the same energy as the majority of the γ rays produced through the atmospheric neutrino interactions in the detector. With a lower energy threshold of 4 MeV there is an additional source of γ rays from about 30% of such interactions. This would correspond to an additional $0.94^{+1.4}_{-0.9}$ γ rays in the data set.

7.7.3 Multiple Events

An additional cut was placed on the salt data set to remove multiple events. With the standard analysis cuts there were 28 such events stemming from 11 triggers (an event may be part of a triple or even quadruple event, as well as a simple double). This number increased to 38 events when the kinetic energy threshold was lowered to 4 MeV and the energy dependent radial cut was applied [78].

7.8 Blind Tests on the Data Set

All fitting studies conducted so far have only used simulated data sets. If the simulations are a poor replication of the data, then the results may not reflect what would be seen in actual data. This would also be true if there are additional backgrounds which have not been considered. A preliminary study on a statistically reduced data set allows the method to be tested so that changes could be made to the analysis without introducing a bias to the number of the events. The data set must be small enough so that the statistical errors are large enough that the analysis is not biased by preliminary results. An upper limit of a quarter of the final data set should be an adequate sample. In order for the extracted amounts to be compared to the number of events fitted within the standard analysis, they must be livetime-corrected and scaled according to the number of simulations passing that set of cut requirements.

The bias tests conducted on the simulated samples had indicated that separation worked well using a radially-dependent energy cut out to 500 cm, but analysis of the blind data set indicated that there was too much contamination from the external events, both from the H_2O and in the amount of ^{24}Na coming from the water systems. The external events from the H_2O can be seen in Figure 7.2, although it had been assumed that the radial constraint would not need to be quite so tight for their elimination. This effect, combined with the increased levels of ^{24}Na at large radii, overwhelmed any expected ^{208}Tl signal. It was decided to reduce the radius to 450 cm for low energy events (*i.e.* those below 5.5 MeV). This should minimise the size of the other backgrounds with respect to the ^{208}Tland possibly allow for a better fit. The same overall limits of 4.0 MeV and 550 cm remained.

Table 7.5 shows the fitted number of events for 102.6 live days, scaled for simple comparison to the standard events. In the case of the signal and fitted external neutron background this represents the number of fitted events in a constrained fit above the standard analysis threshold and, in the case of the low energy backgrounds is the number of events as obtained from the *in-situ* analysis. The number of extracted ^{208}Tl events is still very small, but the statistical error is large and falls within the expected bounds. The number of NC events fitted includes the number of internal neutron backgrounds; a more true comparison requires deducting 101.5 photodisintegration neutrons and 23.6 addi-

Signal	Fitted	Scaled	Standard
CC	690.6 ± 41.4	2284.3 ± 138	2226.4 ± 72.3
ES	92.4 ± 21.7	264.1 ± 61.9	254.2 ± 35.2
NC	719.2 ± 48.6	2061.6 ± 139.3	2098.1 ± 78.1
Tl	3.66 ± 37.0	7.88 ± 79.57	72.7 ± 36.5
Bi	140.4 ± 21.9	410.3 ± 64.0	390.0 ± 38.5
Na	14.37	38.52	61.5
AV	40.9 ± 22.9	150.48 ± 84.9	130.2 ± 43.4

Table 7.5: The number of events extracted from a data set of 102.6 days as a preliminary investigation of signal extraction using a radially-dependent energy cut. Except for the NC signal, the numbers can be directly compared to a similarly energy-constrained fit above 5.5 MeV and within a fiducial volume of defined by a radius of 550 cm across the whole data set, or in the case of the backgrounds to the numbers extracted from *in-situ* analysis.

tional internal neutrons to give 1996.6 NC events in the standard analysis. The number of NC events in the combined fit only includes the additional neutrons which, if subtracted after scaling for livetime and the analysis window, would give 2053.4 events. The errors given are the statistical ones of the fitting procedure, since the number of ^{24}Na events was assumed to be fixed with no associated errors at this stage. Note that the scaled number of ^{24}Na events does not agree with the standard number of ^{24}Na events. The level of ^{24}Na fixed in the fit was determined for the time period specific to the blind data set, taking into account any assays and calibration deployments that took place. Because these circumstances are not necessarily uniformly distributed across the data sample, the number of ^{24}Na fixed is not simply a livetime scaling of the total number fixed in the data set. Note also that the number of ^{208}Tl and ^{214}Bi events differs from Table 6.4. This study made direct comparisons with [39] for which a slightly different flow rate out of the reserve tank was estimated. This slightly affected the fitted number of ^{208}Tl and ^{214}Bi events.

7.9 Results from the Salt Data Set

With events of kinetic energy greater than 4.0 MeV limited to being within a radius of 450 cm, and those above 5.5 MeV allowed a radius of up to 550 cm there were 6472 events in the data set after the exclusion of the multiple events. This compares with 4722 events

if the standard analysis cuts [39] are applied (and the multiple events are also removed), where both span the usual data taking period in the salt phase of 391.432 live days. However, the majority of these additional data are expected to be attributable to background rather than signal. A model was assumed which constrains the CC energy spectrum to that of the standard ^{8}B neutrino spectrum, a so-called energy constrained fit.

A total of 85.14 ^{24}Na events were fixed in the fit. This number was derived from the number of neutrons calculated to be present in the full data set from calibration sources and the water systems. A Čerenkov-to-neutron event ratio of 8.39:1 was determined by summing the number of Čerenkov events within the analysis window that were produced by a ^{24}Na source (the ^{23}Na was activated by a "superhot" ^{232}Th source of known strength described in Section 6.3.2). This section aims to draw comparisons with the constrained fit performed in [39] in which a different estimate for the flow rate out of the reserve tank was used. The number of background events in Table 7.6 is therefore slightly different to the number in Table 6.4. No investigation of the reduced data set described in Chapter 5, in which the ^{24}Na levels were minimised, was conducted. The other background which was fixed in the fit was the 3.2 γ rays from atmospheric neutrino interactions. The data

Signal	Fitted	Scaled	Standard
CC	2580.0 ± 81.3	2236.9 ± 70.5	2226.4 ± 72.3
ES	356.1 ± 42.3	266.8 ± 31.7	254.2 ± 35.2
NC	2672.9 ± 106.9	2008.3 ± 80.3	2098.1 ± 78.1
Tl	104.8 ± 78.6	59.1 ± 44.3	72.7 ± 36.5
Bi	536.8 ± 54.9	411.2 ± 42.1	390.0 ± 38.5
Na	81.5	61.5	61.5
AV	132.8 ± 44.2	128.1 ± 42.6	130.2 ± 43.4

Table 7.6: The number of events extracted from the full salt data set after applying a radially-dependent energy cut. The 101.25 photodisintegration neutrons must be subtracted from the standard number of NC events before allowing a direct comparison.

was then fitted to PDFs generated at 200 $\times$ SSM and covering the entire data set. The results can be seen in Figure 7.5, where the PDFs have each been scaled to indicate the extracted number of results. The NC PDF fits for all neutron-like events and so will include neutron background which must be subtracted off according to separate estimates of these contributions. However, this no longer includes neutrons from photodisintegra-

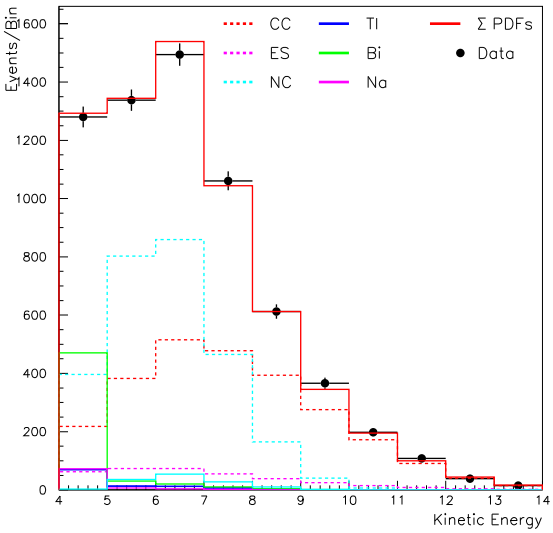

(a) Kinetic energy distribution

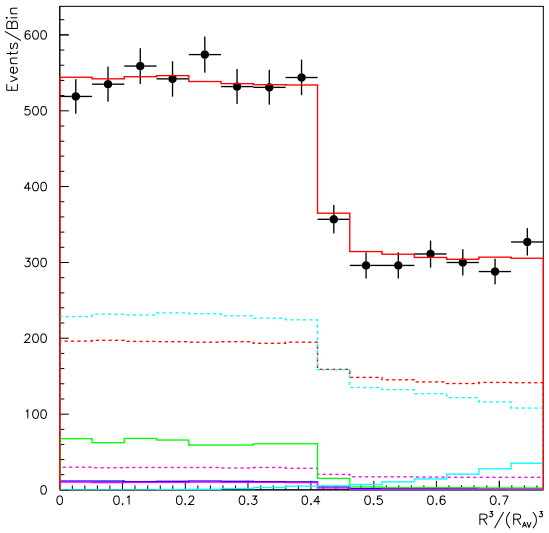

(b) Radial distribution

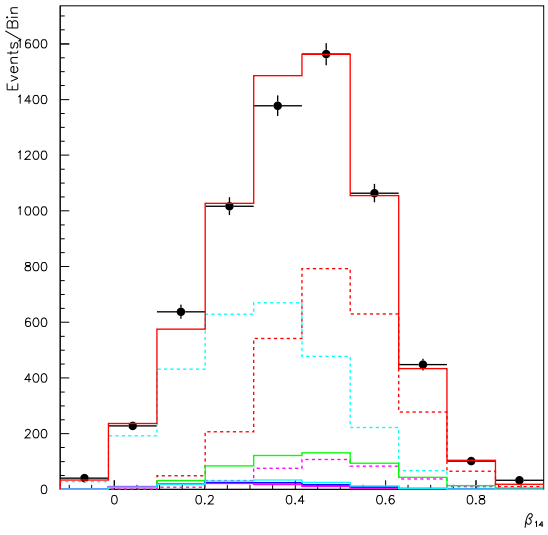

(c) Isotropy distribution

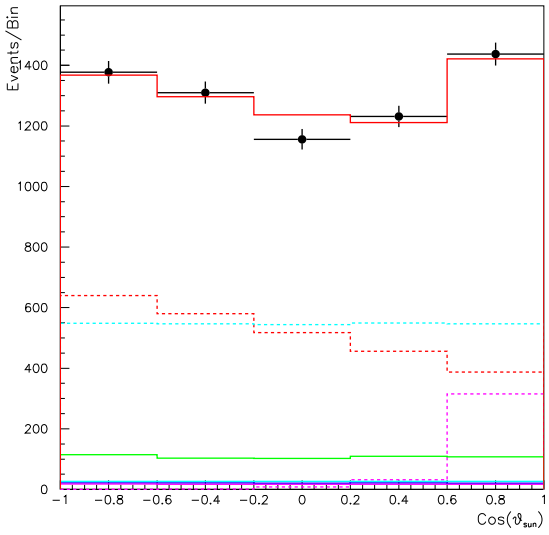

(d) Direction to the Sun distribution

Figure 7.5: Fitting background and neutrino signals in the salt data set across kinetic energy, fiducial volume, isotropy and direction to the Sun. The errors shown are statistical errors on the data only. Note that the multiple events have been subtracted from the data set, and the additional neutron backgrounds have been incorporated in the NC PDF, as there is no way of separating them. Before any flux deductions can be made these events must be subtracted from the total number of fitted neutrons.

tion, as these are explicitly included in the ^{208}Tl and ^{214}Bi events. Thus, the predominant source of internal neutron backgrounds included in the NC signal is $15.8^{+21.3}_{-4.6}$ neutrons from atmospheric neutrinos and the overall total, which also includes (α, n) reactions described in section 3.3.2.2, is $23.6^{+21.3}_{-4.8}$ events. Table 7.7 indicates that there are visible

	CC	ES	NC	^{208}Tl	^{214}Bi
CC	1	-0.226	-0.371	0.137	-0.137
ES	-0.226	1	-0.110	0.051	-0.131
NC	-0.371	-0.110	1	-0.534	-0.236
^{208}Tl	0.137	0.051	-0.534	1	-0.679
^{214}Bi	-0.137	-0.131	0.236	-0.679	1

Table 7.7: Correlation matrix for the fitted background and signal.

correlations between the extracted events.

CC : is mostly correlated with NC because of the similarity in energy. There is a smaller correlation with ES through isotropy. The difference in energy between the signal and background minimises any correlations between them.

ES : is the least dependent on the other signals or backgrounds because it is largely determined through $\cos\theta_{\odot}$. There is slight correlation with CC because they are similar in both energy and isotropy.

NC : is quite correlated with ^{208}Tl because of their similar isotropy distributions. It is also reasonably correlated to CC because of their energy spectra. The signal differs in both of these parameters from ^{214}Bi and so there is very little correlation demonstrated between those two PDFs.

^{208}Tl : is highly correlated with ^{214}Bi because of their overlapping energy spectra. There is also a strong correlation with NC through isotropy.

^{214}Bi : is hardly correlated at all with ES and CC despite their similar isotropy because the energy spectra are so different. Again, it is highly correlated with ^{208}Tl since they have similar energy spectra.

7.10 Systematics

The systematics associated with the fitting parameters were assessed the same way as in [39], except for the resolutions which were assumed here to be one sided only. A summary of all the systematics is given in Table 7.8.

Uncertainty	CC (%)	ES (%)	NC (%)
Energy Scale	$^{+2.7}_{-3.8}$	$^{+0.7}_{-0.0}$	$^{+0.0}_{-1.4}$
Energy Resolution	$^{+0.0}_{-1.3}$	$^{+0.0}_{-0.0}$	$^{+0.0}_{-0.0}$
Energy Non-Linearity	$^{+0.9}_{-0.9}$	$^{+0.0}_{-0.3}$	$^{+0.7}_{-0.7}$
Radial Energy Bias	$^{+1.9}_{-2.5}$	$^{+0.4}_{-0.2}$	$^{+1.0}_{-1.5}$
β_{14} Mean	$^{+2.2}_{-2.6}$	$^{+2.2}_{-1.6}$	$^{+2.8}_{-2.3}$
β_{14} Width	$^{+0.0}_{-0.1}$	$^{+0.4}_{-0.0}$	$^{+0.1}_{-0.0}$
Radial Accuracy	$^{+0.4}_{-0.1}$	$^{+1.2}_{-0.3}$	$^{+1.9}_{-0.0}$
x Vertex	$^{+0.0}_{-0.0}$	$^{+0.2}_{-0.2}$	$^{+0.0}_{-0.2}$
y Vertex	$^{+0.2}_{-0.0}$	$^{+0.0}_{-0.1}$	$^{+0.0}_{-0.3}$
z Vertex	$^{+0.1}_{-0.1}$	$^{+1.1}_{-0.0}$	$^{+0.5}_{-0.2}$
Vertex Spread	$^{+0.1}_{-0.0}$	$^{+1.1}_{-0.0}$	$^{+0.0}_{-0.0}$
Angular Resolution	$^{+0.1}_{-0.0}$	$^{+0.0}_{-0.1}$	$^{+0.1}_{-0.0}$
^{24}Na Models	$^{+0.0}_{-0.0}$	$^{+0.0}_{-0.1}$	$^{+0.4}_{-0.6}$
Neutron Capture Efficiency	-	-	$^{+3.3}_{-2.9}$
Internal γ Rays	$^{+0.0}_{-0.0}$	$^{+0.0}_{-0.1}$	$^{+0.1}_{-0.1}$
Internal Neutrons	-	-	$^{+0.2}_{-0.8}$
Total	$^{+4.1}_{-5.5}$	$^{+3.1}_{-1.6}$	$^{+4.9}_{-4.5}$

Table 7.8: Percentage error systematics on the extracted number of events for the combined signal and background fit, applying a radially-dependent energy cut. The total combines all the systematics, in quadrature, to a greater accuracy than is shown here.

7.10.1 Parameter Systematics

This section summarises the systematic errors on the parameters that were determined in independent analyses. The uncertainty is normally derived by comparing calibration source data and Monte Carlo simulations. More details can be found in [42, 31, 79] which explain their derivation, and in [41] which clearly explains their application. Generally, to investigate how an uncertainty affects the fit, the relevant parameter of each simulated event within all the PDFs is altered by a random number drawn from a Gaussian distribution centred on the value of the uncertainty. The shifted values form new PDFs against which the data is fit.

Energy

The energy scale, resolution, non-linearity and radial energy bias are each considered separately, but each was assessed by comparing ^{16}N source data to simulations [42]. Central position source data was used except for the investigation of a possible radial energy bias, which required a full scan of the detector space.

The energy scale uncertainty was determined to be $\pm 1.13\%$. The uncertainty on the energy resolution is considered as a one-sided error since the width of the distribution can only increase. The resolution function for electrons was determined as the Gaussian shown in Eqn 7.6 based on studies of ^{16}N scans:

$$\sigma_{\mathrm{E}} = -0.131 + 0.383\sqrt{E} + 0.03731\mathrm{E} \; . \tag{7.6}$$

The main uncertainties are those associated with the source strength and position (including detector asymmetry which monitors how the distribution of working PMTs affects the response). Since the ^{16}N source runs at a much higher rate than the expected data rate, there is an uncertainty associated with the corresponding change in gain. The uncertainty on the resolution was determined as:

$$\begin{aligned} \mathrm{E} \; < 5\,\mathrm{MeV}: \quad & \Delta\sigma_{\mathrm{E}} = 3.4\% \\ \mathrm{E} \; > 5\,\mathrm{MeV}: \quad & \Delta\sigma_{\mathrm{E}} = (3.4 + 0.478(\mathrm{E} - 5))\% \; . \end{aligned} \tag{7.7}$$

Radial

The entire structure was lower than in the D_2O phase as indicated by the vertex reconstruction studies, presumably due to the weight of the salt within the vessel [41]. Before fitting, the radius of each simulated event was corrected by a factor of 0.995 and the z position of each data event was increased by 5.5 cm to account for a difference in the actual and fitted position of the AV. The z position represents the position of an event along the vertical axis of the detector. After application of such corrections, any discrepancy in the reconstructed vertex position between calibration source and Monte Carlo is a measure of the error in the radial scale and resolution. Using ^{16}N data the scale uncertainty was estimated as $\pm 1.0\%$, with a resolution that is broader by up to 0.015×16 cm.

There are also uncertainties on the reconstructed position with respect to each of the vertices ($\delta x, \delta y = \pm 2$ cm in the horizontal plane, and $\delta z = \pm 6$ cm) which are expected to have very little impact on the fitting parameter ρ.

Isotropy

The isotropy has an error associated with the mean and width of its distribution, both of which were parameterised by studies that compared these values for simulations and data. Since the isotropy distributions are so different for electron-like and neutron-like events, the distributions of each was individually studied. The standard calibration source used to parameterise any uncertainties implicit to electrons was the ^{16}N source. The ^{252}Cf source was used for comparisons to neutron-like events, and the derived scale and resolution uncertainties are given in Table 7.9. They were

Source	Scale	Resolution
^{16}N	0.85%	0.94%
^{252}Cf	0.48%	0.67%

Table 7.9: The isotropy uncertainty is energy dependent and was separately investigated for neutron-like and electron-like events using ^{16}N and ^{252}Cf calibration sources.

propagated into the extraction by shifting the PDF mean values of β_{14} according to the scale, and smearing the distribution according to the resolution. [5]

Angular Resolution

Above 5 MeV the Čerenkov light from a ^{16}N source is dominated by the forward peaked Compton scattered electrons. Determining the vector between the reconstructed position of the event and the source position approximately gives the direction of travel of the Čerenkov-light emitting electron. A comparison of ^{16}N source runs and simulations allowed derivation of an angular response function:

$$W(\cos\theta_{\mathrm{Res}}) = e^{-2.935-0.345\times \mathrm{E}} \ , \tag{7.8}$$

which, for the purpose of this thesis, was assumed to be valid for energies down to 4 MeV. The shifted value of $\cos\theta_{\odot}$ is then obtained by smearing this distribution around the cosine of the original angle.

7.10.2 Neutron Background Systematics

Salt Activation Neutrons

Approximately 55% of the calibration source time was deployment within a radius

[5] a slightly more conservative estimate was taken for [39]

of 450 cm. It was generally assumed that there would be an equal flux of neutrons drifting into, and out of, the analysed fiducial volume before being captured. An additional ±20% was fixed in the fit to allow for uncertainty in the source position, diffusion length of neutrons before capturing and the length of deployment. The uncertainty on the ^{24}Na in the water system model was estimated as ±50% on each of the following components: the flow rate in the tank, on the production rate in the pipes and neck, and on the drift down from the neck. This gave an upper estimate of 111.9 ^{24}Na events and a lower limit of 45.4 ^{24}Na events in the data set that had to be fixed in the fit.

Neutron Capture Efficiency

The neutron capture efficiency is $(39.8 \pm 0.5^{+1.2}_{-1.0})\%$, which affects the NC flux by $^{+3.3}_{-2.9}\%$.

Neutron Background

The largest contribution to the neutron background in previous signal extraction analyses [76, 71, 47] was the number of photodisintegration neutrons as described in section 3.3.2.2. These are implicitly fitted out by determining the background contribution within the fit. The number of neutrons is therefore reduced from $125.1^{+37.3}_{-32.0}$ to $23.6^{+21.3}_{-4.8}$, which has substantially smaller errors. By considering the correlations between the NC signal and any background capable of producing neutrons whilst fitting, the error on the photodisintegration neutrons is already taken into account. There is no need for any additional error in the neutron background estimate. Since this error must be propagated into the NC flux when the number of neutron backgrounds is subtracted from the fitted number of NC events, there is a slight gain on the systematic error associated with background neutrons.

7.11 Flux Determination

The energy constrained values of the CC, ES and NC flux from the ^{8}B solar neutrino spectrum extracted down to 4 MeV are:

$$\begin{aligned}
\phi_{\mathrm{CC}} &= \mathbf{1.73}\ {}^{+0.05}_{-0.05}\ (\mathrm{stat})\ {}^{+0.07}_{-0.09}\ (\mathrm{syst})\ \times 10^{-6}\mathrm{cm}^{-2}\mathrm{s}^{-1} \\
\phi_{\mathrm{ES}} &= \mathbf{2.25}\ {}^{+0.27}_{-0.27}\ (\mathrm{stat})\ {}^{+0.09}_{-0.05}\ (\mathrm{syst})\ \times 10^{-6}\mathrm{cm}^{-2}\mathrm{s}^{-1} \\
\phi_{\mathrm{NC}} &= \mathbf{4.85}\ {}^{+0.19}_{-0.19}\ (\mathrm{stat})\ {}^{+0.24}_{-0.22}\ (\mathrm{syst})\ \times 10^{-6}\mathrm{cm}^{-2}\mathrm{s}^{-1}\ .
\end{aligned}$$

The NC flux is in good agreement with the latest Standard Solar Models. The BP04[6] model [23] predicts a standard flux of ^{8}B solar neutrinos equal to $5.79\pm1.33\times10^{-6}\mathrm{cm}^{-2}\mathrm{s}^{-1}$. The error on this is mainly theoretical, and is larger than the error on the NC flux provided in this extraction.

They are also in excellent agreement with the constrained results obtained from the standard analysis conducted over the salt data set, which has a higher kinetic energy threshold of 5.5 MeV. For comparison, the values are given below:

$$\begin{aligned}
\phi_{\mathrm{CC}} &= \mathbf{1.72}\ {}^{+0.05}_{-0.05}\ (\mathrm{stat})\ {}^{+0.11}_{-0.11}\ (\mathrm{syst})\ \times 10^{-6}\mathrm{cm}^{-2}\mathrm{s}^{-1} \\
\phi_{\mathrm{ES}} &= \mathbf{2.34}\ {}^{+0.23}_{-0.23}\ (\mathrm{stat})\ {}^{+0.14}_{-0.15}\ (\mathrm{syst})\ \times 10^{-6}\mathrm{cm}^{-2}\mathrm{s}^{-1} \\
\phi_{\mathrm{NC}} &= \mathbf{4.81}\ {}^{+0.19}_{-0.19}\ (\mathrm{stat})\ {}^{+0.27}_{-0.28}\ (\mathrm{syst})\ \times 10^{-6}\mathrm{cm}^{-2}\mathrm{s}^{-1}\ .
\end{aligned}$$

The obvious discrepancy between the CC (electron-type neutrino) and NC (all types of neutrino) flux is strong evidence for flavour change, neatly illustrated in Figure 7.6. It shows each flux as a combination of electron and non-electron type neutrinos. The solid bands indicate the combined statistical and systematic uncertainties on each flux when a fit is performed down to 4 MeV. The blue dotted line compares the BP04 model with its statistical and theoretical uncertainty to the measured NC flux.

7.12 Discussion

It is possible to extract neutrino signals down to kinetic energy of 4 MeV if the external backgrounds which had previously limited the energy threshold to 5.5 MeV are removed. This seems to be possible by applying a radially-dependent energy cut which excludes low energy events at high radii. It also allows the ^{24}Na to be modelled in the fit without

[6] a model calculated by Bahcall and Pinnsoneault in 2004

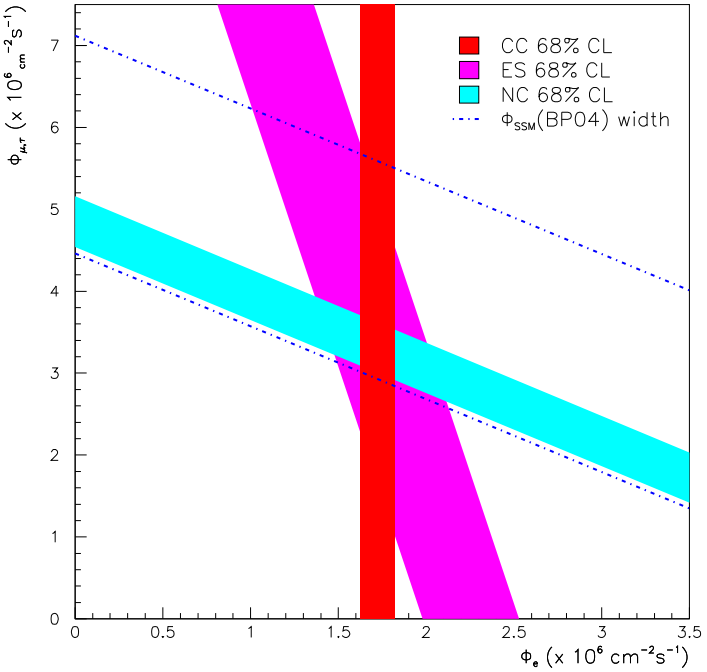

Figure 7.6: The bands indicate the extracted flux for the neutrino signals, where the width of the band is the spread of the statistical and systematic uncertainties. The total ^{8}B solar neutrino flux predicted by one of the latest SSM models is shown by the blue dotted lines parallel to the extracted NC flux.

having to assess any change in the radial profile of these events from the water systems entering via the neck. The extracted neutrino signals are in excellent agreement with those obtained in the higher energy threshold analysis, and the fitted out levels of background are in agreement with those obtained in the *in-situ* analysis. Because the error associated with the estimate of the number of photodisintegration neutrons has been implicitly incorporated into the fit the systematic errors for the neutron backgrounds are smaller for the NC flux.

The next logical step in the analysis would be to perform a fit in which the CC energy spectrum is not constrained, to see if there is any suppression of the flux at lower energies, or to see if the experiment has any sensitivity to detect this. The difficulty would be separating the CC and ^{214}Bi flux, which are similar in all parameters except energy. One possibility that requires further investigation might be to constrain the amount of ^{214}Bi according to estimates from the independent *ex-situ* measurements of the

radioactivity levels. Another possibility is to lower the energy threshold to incorporate a region where the ^{214}Bi completely overwhelms the CC signal, and using the results from this bin to constrain the amount of ^{214}Bi. However, this is slightly model dependent and limited by the low energy threshold of the detector.

Chapter 8

Conclusion

The Sudbury Neutrino Observatory (SNO) experiment is a heavy water imaging Čerenkov detector that has the unique ability of measuring both the total active flux of solar neutrinos, and the flux of electron-type only neutrinos, from the ^{8}B spectrum.[1] Any measured deficit in the electron-type neutrino flux with respect to the total flux strongly supports the theory of flavour oscillations in the neutrino sector, as seen in the quark sector.

A maximum likelihood fit statistically separates the measured events using PDFs for each signal in a number of characteristic variables. Background events which are well understood and statistically separable from other PDFs may also be determined in the fit. Backgrounds which can not be separated must be constrained within the fit, or subtracted from the relevant signal measurement. The standard analysis of the salt data set used a lower kinetic energy threshold of 5.5 MeV. Lowering the kinetic energy threshold to 4 MeV using a radially dependent energy cut was possible because of previous studies to understand the prominent backgrounds within the region $\sim 4 - 5$ MeV. The ability to define an energy dependent fiducial volume for analysis was added into the signal extraction code.

The total active flux is measured by detecting neutrons that result from the interaction of a neutrino with a deuteron that splits it into its constituents of a neutron and a proton. The threshold for this interaction is 2.2 MeV. All sources producing γ rays equal or greater in energy must be identified and monitored for their contribution to the neutron background through photodisintegration of the deuteron. Such γ rays are present in the naturally occurring radioactive chains of ^{232}Th and ^{238}U, which are visible in the detector

[1] and also minimal contribution from neutrinos from the hep reaction

through the production of Čerenkov light by their daughters; ^{208}Tl and ^{214}Bi. The presence of salt (NaCl) in the detector allows activation of ^{23}Na through neutron capture. The ^{24}Na was produced by neutrons ingressing from the rock surrounding the experiment into the water systems and were swept into the detector during D_2O circulation. They were also present in the D_2O after deployment of certain calibration sources. The subsequent excited state, ^{24}Na, releases two γ rays and a β particle on its decay to the ground state; these are also capable of photodisintegrating the deuteron.

Each radioactive element has a different cross section for deuteron photodisintegration and so the levels must be determined separately. The use of Monte Carlo simulations to investigate the feasibility of separation relied on the accurate modelling of the physical processes that particles can undergo within the detector. A review of current theories predicting the cross sections for deuteron photodisintegration was presented in Chapter 4. The models compared well to those currently used within the Monte Carlo simulations.

A method was developed from that used in the first phase (pure D_2O) to separate ^{208}Tl and ^{214}Bi distributions according to their isotropy, a parameter that uses the distribution of the Čerenkov cone of light projected on to the PMTs. A different measure of isotropy was used. In the first phase events were parameterised by the mean of the angle between all hit PMTs (θ_{ij}). In the second phase the Legendre polynomials (βparameters) of the cosine of this angle were expanded and combined in the form β_{14} which gave good separation between the CC and NC events. ^{208}Tl decays release a single β and several γ particles. The γ rays each Compton scatter off electrons within the D_2O; each one of these will produce a ring of Čerenkov light. The light from ^{214}Bi decay in the analysis window is dominated by a single β decay and so gives rise to just a single Compton scattered electron producing a ring of light. Ring fitting algorithms can not be used because of the scattering that smears the edges of the projected ring, but the average width of the cone is used to indicate whether the distribution of light has come from several particles or just a single one. Maximum likelihood is used within a low energy window to determine the amounts of ^{208}Tl and ^{214}Bi according to the isotropic distributions of the events.

A period of data with particularly high rate at low energies was identified through preliminary use of this technique. The source of background was identified as Radon which had leaked in through an open valve in the water systems. The time period coincided with a large seismic event which shifted the energy scale and so the Radon could not be

used as a calibration source. The investigation prompted the application of Chauvenet's criterion to the salt data set, to remove periods of unexpectedly high background rate.

Since the β decay of ^{24}Na produces two γ particles its isotropy closely resembles that of ^{208}Tl. It can therefore not be separated in the same way. Chapter 5 explained how ^{24}Na levels were determined by modelling the ingression from the water systems and estimating the production from calibration sources after their removal. This amount of ^{24}Na could then be used as a constraint within the likelihood fit to separate the other backgrounds. A separate method removed time periods when the ^{24}Na was most likely to be present within the data set, thus minimising the amount of ^{24}Na to be constrained within the fit. Chapter 6 showed how these two methods yielded very similar amounts of ^{208}Tl and ^{214}Bi which indicates reasonable modelling of the ^{24}Na.

Measurements of each of the radioactive backgrounds capable of photodisintegrating the deuteron gave an estimate of the number of such neutrons within the data set. The total detected number within a radius of 550 cm and above a kinetic energy threshold of 5.5 MeV was $102.2^{+31.6}_{-29.6}$ neutrons. This estimate, along with other neutron backgrounds, would have to be deducted from any NC measurement before yielding the total active flux.

Chapter 7 showed good agreement between the current analysis technique, which deducted the backgrounds from the NC measurement, and an analysis method which fitted the signal and backgrounds in parallel. Because the photodisintegration is implicitly modelled in the background PDFs used in the fitting, and the cross sections for photodisintegration within these simulations has been shown to be accurate, there was no need to subtract off the photodisintegration backgrounds within the combined fit.

This thesis has presented the first measurements of these spectra down to a kinetic energy of 4 MeV using an energy dependent fiducial volume, and showed a clear deficit in the electron-type neutrino flux with respect to the total active flux. The total active neutrino flux is in very good agreement with SSM predictions. All three determined fluxes (NC, CC, ES) are also in excellent agreement with the latest results from a constrained fit in the salt phase performed with a higher kinetic energy threshold of 5.5 MeV. This provides no evidence for any significant spectral distortion in the low energy region, and does not indicate the presence of sterile neutrinos whose existence could suppress the total active flux below 5 MeV.

Glossary

AV **A**crylic **V**essel

CC **C**harged-**C**urrent (ν interaction)

ECA **E**lectronics **Ca**libration

EFT **E**ffective **F**ield **T**heory

ERT **E**ffective **R**ange **T**heory

ES **E**lastic **S**cattering (ν interaction)

ITR **I**n **T**ime **R**atio

NC **N**eutral-**C**urrent (ν interaction)

MC **M**onte **C**arlo

MSW **M**ikheyev **S**mirnov **W**olfenstein Effect (the matter effect)

MXF **Max**imum likelihood signal extraction package

NCD **N**eutral **C**urrent **D**etector.

NN **N**ucleon **N**ucleon interaction.

OWL **O**ut**w**ard **L**ooking PMT.

PDF **P**robability **D**ensity **F**unction.

PMT **P**hoto-**M**ultiplier **T**ube.

PSUP **P**MT **SUP**port structure.

SNO **S**udbury **N**eutrino **O**bservatory

SNOMAN **SNO** **M**onte Carlo and **AN**alysis software.

SNU **S**olar **N**eutrino **U**nit (1 capture per 10^{36} atoms per second).

SM **S**tandard **M**odel of particle physics.

SSM **S**tandard **S**olar **M**odel.

TAC **T**ime to **A**mplitude **C**onverter.

Bibliography

[1] W. Pauli. *Physics Today*.

[2] C. S. Wu et al. *Physical Review*, **105** (1957) 1413.

[3] R. Feynman and M. Gell-Mann. *Physical Review*, **109** (1958) 193.

[4] M. Goldhaber, L. Grodzin and A. Sunyar. *Physical Review*, **109** (1958) 1015.

[5] C. Cowan and F. Reines. *Physical Review*, **90** (1953) 492.

[6] C. Cowan and F. Reines. *Physical Review*, **113** (1959) 273.

[7] K. Zuber. "Neutrino Physics". IoP Publishing, first edition (2004).

[8] R. Davis. *Physical Review Letters 12*, **11** (1964) 303.

[9] The Royal Swedish Academy of Sciences. Press Release: The 2002 Nobel Prize in Physics.

[10] B. T. Cleveland et al. *Astrophysics J*, **496** (1998) 505.

[11] B. Pontecorvo (1972). Personal communication to John Bahcall.

[12] J. Bahcall. *Physical Review B*, **433** (1998) 1.

[13] B. R. Martin and G. Shaw. "Particle Physics". Wiley, fourth edition (1999).

[14] B. Pontecorvo. *Soviet Physics JETP*, **26**, 5 (1968) 984–988.

[15] M. Apollonio et al. *Physical Letters*, **B466** (1999) 415.

[16] A. Y. Smirnov. *11th Workshop on Neutrino Telescopes, Venice*. ArXiv:hep-ph/0305106 v1.

[17] L. Wolfenstein. *Physical Review D*, **17** (1978) 2369.

[18] S. Mikheyev and A. Y. Smirnov. *Nuovo Cimento*, **C9**, 17.

[19] F. Boehm and P. Vogel. "Physics of Massive Neutrinos". Cambridge University Press, second edition (1992).

[20] H. A. Bethe. *Physical Review Letters*, **56**, 12.

[21] O. Cremonesi. *Nuclear Physics B Proceedings Supplement*, **91** (2003) 287–296.

[22] The Kamland Collaboration. *submitted to Physical Review Letters*. ArXiv:hep-ph/0406035.

[23] J. N. Bahcall and C. Peña-Garay. *Physical Review Letters*, **92**, 12.

[24] The Super-Kamiokande Collaboration. *Physical Review Letters*, **81** (1998) 1562.

[25] H. Chen. *Physical Review Letters*, **55** (1985) 1534.

[26] The SNO Collaboration. *Nuclear Instruments and Methods in Physics Research*, **A449** (2000) 172.

[27] International Commission on Radiation Units & Measurements. "Stopping Powers for Electrons and Positrons" (1984).

[28] F. J. Kelly and H. Überall. *Physical Review Letters*, **16** (1966) 145.

[29] G. 't Hooft. *Physical Letters B*, **37**.

[30] B. Krusche et al. *Nuclear Physics*, **A386** (1982) 245.

[31] J. A. Dunmore. "The Separation of CC and NC Events in the Sudbury Neutrino Observatory". Ph.D. thesis, University of Oxford (2004).

[32] A. Noble (editor). "Scientific Review of SNO Water Systems" (1996). SNO Technical Report.

[33] H. Heron. "Techniques to Measure the NC Background in the SNO Experiment". Ph.D. thesis, University of Oxford (1998).

[34] The SNO Collaboration. *Nuclear Instruments and Methods*, **A501** (2003) 399.

[35] J. R. N. Cameron. "The Photomultiplier Tube Calibration of the Sudbury Neutrino Observatory". Ph.D. thesis, University of Oxford (2001).

[36] The SNO Collaboration. "The Sudbury Neutrino Observatory Proposal" (1987). SNO internal report SNO-87-12.

[37] J. Klein. "The SNO Trigger". SNO Technical Report.

[38] M. G. Boulay. "Direct Evidence for Weak Flavour Mixing with the Sudbury Neutrino Observatory". Ph.D. thesis, Queen's University (2001).

[39] The SNO Collaboration. "Measurement of Electron Energy Spectra, Flux, and Day-Night Asymmetries of ^{8}B Solar Neutrinos from the 391-Day Salt Phase SNO Data Set". Awaiting publication.

[40] M. J. Lyon. "Neutron Transport in the Sudbury Neutrino Observatory". Ph.D. thesis, University of Oxford (1996).

[41] J. R. Wilson. "A Measurement of the ^{8}B Solar Neutrino Energy Spectrum at the Sudbury Neutrino Observatory". Ph.D. thesis, University of Oxford (2004).

[42] K. Graham. "Energy Systematics for the Next Salt Paper" (2004). SNO internal analysis note.

[43] N. K. M^{c}Cauley. "Producing a Background Free Data Set for Measurement of the Charged Current Flux and Day-Night Asymmetry at the Sudbury Neutrino Observatory". Ph.D. thesis, University of Oxford (2001).

[44] V. L. Rusu. "Measurement of the total ^{8}B Solar Neutrino Flux at the Sudbury Neutrino Observatory". Ph.D. thesis, University of Pennsylvania (2003).

[45] M. Boulay et al. "Other Background Sources in the Salt Phase of SNO" (2003). SNO internal analysis note.

[46] Livetime Working Group. "Livetime for the Full Dataset" (2003). SNO internal analysis note.

[47] The SNO Collaboration. *Physical Review Letters*, **92** (2004) 181301.

[48] N. K. M^{c}Cauley (2005). Private communication.

[49] F. Duncan (2004). Private communication.

[50] C. Kyba (2002). Private communication.

[51] A. Hallin. "24Na Activation in the Neck". `http://www.sno.phy.queensu.ca/~hallin/private/24Na_Activation_in_Salt.html`.

[52] J. Farine et al. "Run Selection - Water Systems and Low Energy Background Considerations" (2004). SNO Internal Document.

[53] J. W. Chen and M. J. Savage. *Physical Review C*, **60** (1999) 065205. ArXiv:nucl-th/9907042.

[54] G. Rupak. *Nuclear Physics A*, **678** (2000) 405. ArXiv:nucl-th/9911018 v2.

[55] H. Bethe and R. Peierls. *Proceedings of the Royal Society*, **A148** (1935) 146.

[56] H. Arenhovel and M. Sanzone. "Photodisintegration of the Deuteron: A Review of Theory and Experiment". Springer Verlag (1991).

[57] E. Fermi. *Physical Review*, **48** (1935) 570.

[58] H. Bethe and C. Longmire. *Physical Review*, **76** (1949) 38–50.

[59] S. Weinberg. *Physical Letters B*, **251** (1990) 288.

[60] M. J. Savage. *Nuclear Physics A*, **721** (2003) 94–103. ArXiv:nucl-th/0301058 v1.

[61] J. W. Chen (2004). Private communication.

[62] X. Chen. "Monte Carlo Simulations and Analysis of Backgrounds in the Sudbury Neutrino Observatory". Ph.D. thesis, University of Oxford (1997).

[63] G. M^{c}Gregor. "The Measurement of the Neutral Current Interaction at the Sudbury Neutrino Observatory". Ph.D. thesis, University of Oxford (2002).

[64] R. B. Firestone et al. "Table of Isotopes". Wiley Interscience, eighth edition (1999).

[65] A. Hallin and C. Howard (2004). Private communication.

[66] C. Sims and N. Jelley. "Determining the Neutron Background from Sodium Activation for Day Night Studies and *In Situ* Analysis" (2004). SNO internal analysis note.

[67] P. Skensved and B. Robertson. "Summary of Backgrounds in SNO". SNO Technical Report SNO-1994-13.

[68] P. Skensved. "Neutron Estimates." `http://www.sno.phy.queensu.ca/~peter/private/neutron_estimates.html`.

[69] T. Noble (2004). Private communication.

[70] A. Hallin. `http://www.sno.phy.queensu.ca/~hallin/private/24Na_in_the_Neck.html`.

[71] The SNO Collaboration. *Physical Review Letters*, **89** (2002) 011301.

[72] R. Lange (2004). Private communication.

[73] L. Lyons. "Statistics for Nuclear and Particle Physicists". Cambridge University Press, first edition (1992).

[74] J. Klein. "A Short Sharp Shock: Modeling the Čerenkov Tail with the ^{222}Rn Spike" (2004). SNO internal analysis note.

[75] Neutron Working Group. "Neutron Detection Efficiency During the Salt Phase of SNO" (2003). SNO internal analysis note.

[76] The SNO Collaboration. *Physical Review Letters*, **87** (2001) 071301.

[77] P. de Holanda and A. Smirnov. *Physical Review D*, **69** (2004) 113002.

[78] H. O'Keeffe (2005). Private communication.

[79] K. Graham. "Angular for the Next Salt Paper" (2004). NSP Angular Response Update.